Radiated Noise Assessment of Shipboard Systems Using Vibration Analysis

by

David Elatov

Submitted to the Department of Mechanical Engineering
in partial fulfillment of the requirements for the degrees of

Master of Science in Naval Architecture and Marine Engineering

and

Master of Science in Ocean Engineering

at the

MASSACHUSETTS INSTITUTE OF TECHNOLOGY

February 2022

Author .....
Department of Mechanical Engineering
February 15, 2022

Certified by .....
Professor Steven B. Leeb
Professor of Electrical Engineering and Computer Science
Thesis Supervisor

Accepted by .....
Professor Nicolas Hadjiconstantinou
Chairman, Department Committee on Graduate Students

Radiated Noise Assessment of Shipboard Systems Using Vibration Analysis

by

David Elatov

Submitted to the Department of Mechanical Engineering
on February 15, 2022, in partial fulfillment of the
requirements for the degrees of
Master of Science in Naval Architecture and Marine Engineering
and
Master of Science in Ocean Engineering

Abstract

Since the emergence of acoustic warfare, especially in modern times, noise regulation of ships has become a concern, leading to ships being built and tested with rigorous and periodical measures to ensure their noise signatures are minimal. Simultaneously, other predictive maintenance and load monitoring systems are installed on ships for better resource management. This work came from an idea to merge both worlds and used the predictive maintenance system to predict the radiated noise due to vibrations from the ship's systems.

First, a scientific survey to study the field yielded two plausible theoretical models that could help predict vibro-acoustic transmissions in complex systems - Finite Element Analysis and Statistical Energy Analysis. Those methods were implemented on a simple metal cabinet with limited success—however, a frequency-gain model constructed using a set of planned experiments, performed with reasonable accuracy.

Later on, the experimental-based model construction method was implemented on a test ship to predict its frequency-gain model for different shipboard systems. This method did not yield good accuracy; however, using different data analysis tools such as Recurrent Neural Networks helped improve prediction accuracy. Eventually, this work suggests future directions to follow, based on the experience gathered from the research.

Thesis Supervisor: Professor Steven B. Leeb
Title: Professor of Electrical Engineering and Computer Science

Acknowledgments

The tradition attributes three books of the bible to wise king Solomon: Song of Songs, Proverbs, and Ecclesiastes. When he was young, youthful, and lustful, he wrote the "Song of Songs," containing love poems of faith. As he matured, "Proverbs" was written at his peak, incorporating the wisdom of life. Eventually, during his late days, "Ecclesiastes" came to life, concluding the insignificance of the material world. Nevertheless, my acknowledgments are presented to give special gratitude to the organizations and personnel involved in this research.

I would like to thank Professor Steven Leeb for his excellent advice, guidance, and patronage that brought this work to take shape. I would also like to thank the team under Prof. Leeb's leadership, colleagues, and friends - Lt. Andrew Moeller, Lt. Devin Quinn, Tommy Krause, and Daisy Green. The crew on of the test ship are to be thanked as well.

Additionally, I would like to extend my gratitude to the 2N staff, Captain Leghorn, Captain Bebermeyer, and Commander Jonart, who acted both as my teachers and mentors. Also, the contribution and support of MIT staff at the Department of Mechanical Engineering are acknowledged. I would also like to thank the Israeli MOD and Navy for the financial support and allotted time to study and develop myself here at MIT.

Special thanks are also given to Saana McDaniel for her caring and supportive help (Kiitos Paljon!).

These hard times far from home and family could not have passed quickly without my friends in the 2N program and my supportive friends in Israel. Thank you from the bottom of my heart. Mainly, I would love to thank my parents, Aviva and Semion, that I have reached this point in life with their support and guidance.

Thank you all for your time, help, and support.

לַכֹּל זְמָן וְעֵת לְכָל חֵפֶץ תַּחַת הַשָּׁמָיִם׃ עֵת לָלֶדֶת וְעֵת לָמוּת, עֵת לָטַעַת וְעֵת לַעֲקוֹר נָטוּעַ,
עֵת לַהֲרוֹג וְעֵת לִרְפּוֹא, עֵת לִפְרוֹץ וְעֵת לִבְנוֹת, עֵת לִבְכּוֹת וְעֵת לִשְׂחוֹק, עֵת סְפוֹד וְעֵת רְקוֹד,
עֵת לְהַשְׁלִיךְ אֲבָנִים וְעֵת כְּנוֹס אֲבָנִים, עֵת לַחֲבוֹק וְעֵת לִרְחֹק מֵחַבֵּק, עֵת לְבַקֵּשׁ וְעֵת לְאַבֵּד,
עֵת לִשְׁמוֹר וְעֵת לְהַשְׁלִיךְ, עֵת לִקְרוֹעַ וְעֵת לִתְפּוֹר, עֵת לַחֲשׁוֹת וְעֵת לְדַבֵּר, עֵת לֶאֱהֹב וְעֵת לִשְׂנֹא,
עֵת מִלְחָמָה וְעֵת שָׁלוֹם.

(קהלת ג', א'-ח')

To everything there is a season, and a time to every purpose under the heaven:
a time to be born, and a time to die; a time to plant, and a time to pluck up that which is planted;
a time to kill, and a time to heal; a time to break down, and a time to build up;
a time to weep, and a time to laugh; a time to mourn, and a time to dance;
a time to cast away stones, and a time to gather stones together;
a time to embrace, and a time to refrain from embracing; a time to get, and a time to lose;
a time to keep, and a time to cast away; a time to rend, and a time to sew;
a time to keep silence, and a time to speak; a time to love, and a time to hate;
a time of war, and a time of peace.

(*Ecclesiastes 3, 1-8*)

Contents

List of Figures

List of Tables

Chapter 1

Introduction

Since the emergence of submarine warfare at the intro of the 1900s', anti-submarine warfare (ASW) technologies were in a constant race to obliterate the built-in advantage using acoustic measures to detect submarines. As the technologies for submarine detection advanced, so did the submarine design techniques adapted to build quieter and stealthier submarines. Consequently, other marine vessels (especially military surface ships) became aware of the potential in lowering their acoustic signature, making them less detectable to enemy submarines [3].

Today, submarines and surface vessels are built to near perfection regarding noise control, either by passive or active means. Passive means include installing shock mounts, using sound-isolating materials, and designing propellers for low cavitation. On the other hand, active means to reduce acoustic signature include sound mufflers and different tactical maneuvers. It passes through rigorous radiated noise tests in dedicated ranges to ensure the ship withstands the acoustic requirements.

One may claim that its acoustic signature slightly changes as soon as the ship leaves the acoustic range. However, a ship is a living system that constantly changes; it faces ware, aging, corrosion, and pipe clogging. Thus, it is necessary to assess its acoustic signature at any given time, comparing it to the previously measured acoustic signature as a reference.

To do so, one must understand the mechanisms related to noise. Namely, how noise generates and how it propagates. Measuring the noise at its source and knowing

its propagation path will hopefully give a fair assessment of the radiated noise. This chapter will focus on the theoretical background for the following work.

1.1 Marine Radiated Noise

Sound is a mechanical disturbance that propagates through a medium, where its speed of sound fundamentally relies on the properties of that medium. For most fluids, the speed of sound is relatively constant and isotropic; in standard conditions (1 atm, $20°C$), its value in the air is $343\frac{m}{s}$, and for freshwater is $1481.8\frac{m}{s}$.

In seawater, the speed of sound differs according to temperature and salinity. Consequently, thermal layers in the ocean create acoustic ducts and waveguides that allow different frequencies into the guide and transfer them more efficiently. For instance, the SOFAR (Sound Fixing And Ranging) Channel is a deep channel that allows low-frequency sound to propagate effectively along distances and was used during the cold war to detect and follow Soviet Ships. [16]

Additionally, other physical effects such as compressibility or friction attenuate the noise, causing its decay. Figure 1-1, taken from source [6] shows the absorption in dB/km for different sound frequencies. Specifically to saltwater, higher frequencies tend to decay faster than lower ones. Marine mammals well use this property: while seals and dolphins hunt in close packs and make no wish to alert the prey of their approach, they use high-frequency sounds that dissipate faster. On the other hand, whales that do not live in small packs and travel long distances use low-frequency noises to communicate through long distances.

While designing a marine vessel, one must account for the allowable radiated noise levels that must not prevail over the relative noise levels. The Wenz Curve (Figure 1-2), taken from [2], shows the surrounding noise levels for different sea-states and marine environments. For example, a submarine that does not wish to be detected in usual maritime traffic must not exceed a level of 60dB in most of its frequency range. It must not exceed 40dB in higher frequencies: tenfold quieter.

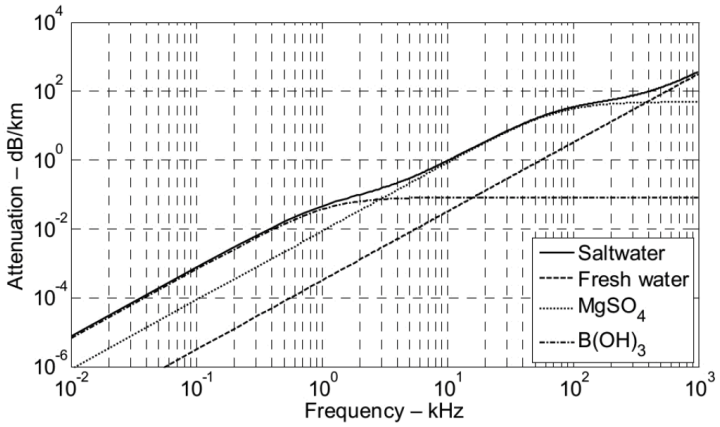

Figure 1-1: Sound Absorption in Water

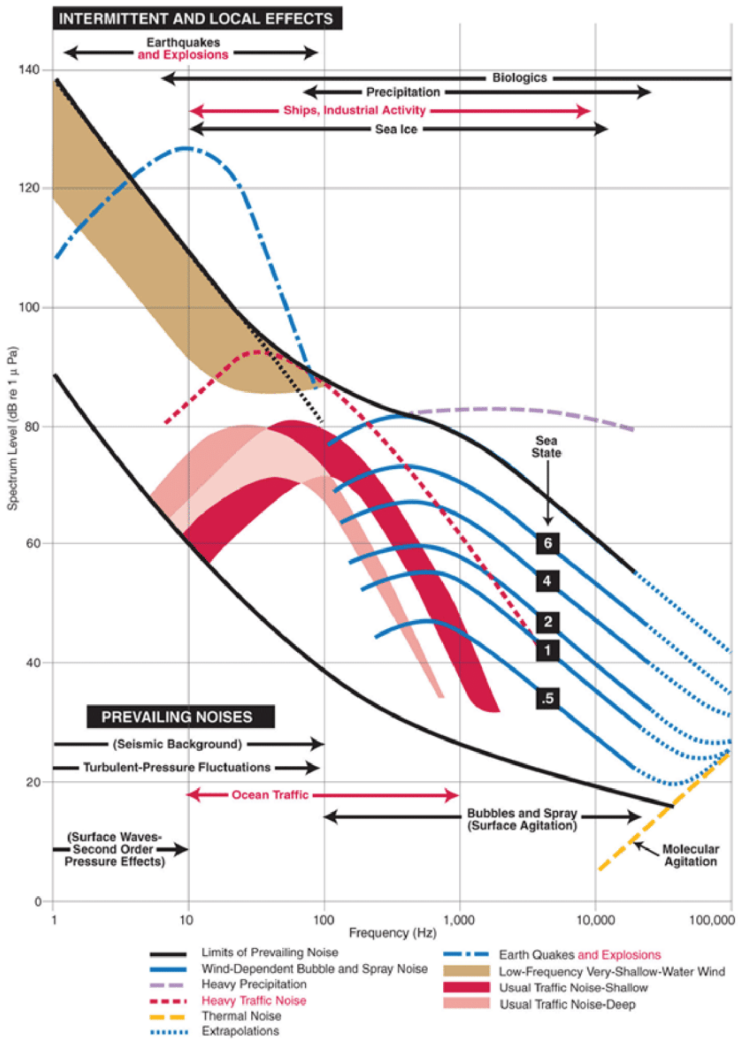

Figure 1-2: The Wenz Curve

1.2 Ship Acoustics

Shipboard systems, designed to maintain the ship operating, create noise constantly. This noise is generated through various mechanisms: Mechanical vibrations, structural noise, flow turbulence, cavitation, shocks, electromagnetic effects, and more, where its mechanism has its characteristics. Flow turbulence noise, for example, is connected to the pressure fluctuations in the flow and is distributed along a wide range of frequencies (usually low). On the other hand, cavitation created by the explosion of tiny vapor bubbles upon a surface is a wide-band, high-frequency noise modulated with the number of propeller blades.

Regarding conduction and transmission, the mechanisms are classified according to the medium on which they are transmitted: Structure Borne Noise (SBN) is used for solids, Air Borne Noise (ABN) is used for air, and similarly for water, WBN. Additionally, the Noise spectrum radiated from a ship is divided into three categories: low, mid, and high-frequency ranges [16]. Each category deals with the different deformation types associated with these frequencies.

This division was used when the computational resources were limited, allowing different simplifications for calculations. Still, simplistic models of wave transmission through solids and fluids are well known and studied [13]. In addition, convoluted models were built in order to methodically assess and predict radiated noise due to mechanical vibrations, using some correlations [4]. Moreover, models that include a fluid-structure interface in noise transmission [19] were constructed in order to assess and lower the associated interaction models.

Even today, where modern computational tools allow us to model the ship in great detail, the computational power needed to assess the radiated noise is quite resource-consuming and, in most cases, is not justified by the accuracy it provides. Consequently, most of the works mentioned above were conducted to assess noise levels easily and avoid direct computation of the entire structure. The following sub-sections will provide a survey regarding methods to assess shipboard noise.

1.2.1 Structural Simplifications

Structural simplifications claim that the structural modes are the most prominent and efficient noise transfer mechanisms from a structural point of view. As mentioned above, this method divides the spectrum into three ranges: low, mid, and high-frequency ranges.

The Low Frequency (LF) range is mainly associated with the hull structure and vibration, which means that it correlates with the deformation of the hull as a nonuniform beam. Half the ship's length defines the top limit of the low-frequency range. For example, a ship 300 meters long will allow a wavelength of 150 meters, giving a frequency of around 10Hz, as shown below:

$$f = \frac{c}{\lambda} \approx \frac{1500m/s}{150m} \approx 10[\frac{1}{s}] \tag{1.1}$$

Shorter ships allow a wider low-frequency range. This frequency range also includes longitudinal deformations, although considered negligible in magnitude. In order to assess the modes and activation energies related to them, one must model the ship as a beam with a changing longitudinal stiffness to analyze its behavior in both the vertical and lateral deformations.

On the other hand, the Mid Frequency (MF) noise range deals with vibrations of specific sections, neglecting any further extent. Specifically, the deformations of the entire section itself due to localized forces. On the other hand, the High Frequency (HF) noise range deals with the vibration of the hull plates individually as plates with stiffened edges [11], [16].

While this method supplies a fair estimation for structural modes (assuming the radiated noise is linear), many losses and amplifications are not accounted for, and this method neglects the acoustic pathways inside the structure from the source to the hull. Therefore, this method is primarily helpful when the hull-mounted vibrations are known and are in the linear range. Otherwise, for non-hull mounted systems, one must calculate the transfer function from the system to the hull, with multiple acoustic pathways.

1.2.2 Transfer Function Assessment

Works like [4] and [18] try and assess the transfer function using correlations between power and noise. These take the multi-path approach where most possible acoustic paths are accounted for, with resulting correlations for each path: Structure Borne Noise (SBN), Air Borne Noise (ABN), system-mount-base interactions, and air to structure interactions. These models use previously investigated correlations or direct calculation methods for their assessment. Later, assuming non-coherence of sound sources, the magnitudes sum up to a level estimate. For example, according to [4] the free velocity level or a standard marine diesel can be correlated using:

$$L_F^S = \Delta L_V - 20\ log_{10} m_E + 20\ log_{10} P + 30\ log_{10} \frac{s}{s_0} + 122\ (dB, re.\ 5 \cdot 10^{-8} \frac{m}{s}) \quad (1.2)$$

Where ΔL_V is a correction factor depending on the 1/3 octave bandwidth, m_e is the engine mass in kilograms, P means the engine power in kilowatts, and the operational and rated speed accordingly are marked s and s_0.

In addition, the transfer function assuming rigid hull installation of the engine is estimated by using:

$$L_X = 20\ log_{10} 2\pi f_c m_e - 10\ log_{10} \Delta f_{OB} - 146 \quad (dB, re.\ \frac{10^8}{5} \frac{N \cdot s^2}{m}) \quad (1.3)$$

Where f_c and Δf_{OB} are the 1/3 octave center frequency and bandwidth in hertz accordingly. This example and others shown in [4] are generally used to evaluate the radiated noise level out of the ship, with some pretty accurate results compared to other theoretical models.

Nevertheless, this work mainly targets large machine parts (i.e., main engine) and does not account for an ensemble of machines working together, although possible to assume linearity. Moreover, these correlations are not always correct or were empirically proven on various vessels. Therefore, although useful for preliminary design or general assessment, this method cannot supply the needed resolution for dealing with an actual "living" ship signature.

1.2.3 Finite Element Analysis

Commonly used in the engineering field, the Finite Element Analysis (FEA) method allows direct computation of structural modes and even a fair estimate of excitation responses for different structures. Using a high fidelity model allows the designer to estimate static and dynamic responses to different loads. Nevertheless, modeling large structures like ships requires a high amount of elements, pumping up computation costs by demanding more substantial computation power and longer calculation times. Moreover, this method relies on the model's accuracy and detail that is not worthwhile to the designer. For example, the work in source [17] took 8 hours to calculate a physical 1 second of a dynamic response using four cores in parallel computation using FEA.

1.2.4 Statistical Energy Analysis

Work done by R.Lyon in the late 1950's [10] showed that coupled oscillators exchange energy in a manner proportional to their energetic state, in a similar way thermal conductivity models do. Since the nature of vibrations and exciting forces is inherently random, a statistical approach was offered to help and model the mechanisms in which noise and vibrations are transferred between different media by batching the energy associated with vibration in frequency range packets. Assuming that structural modes are the most efficient way to transfer the energy, the amount of modes for each frequency range (modal density) is accounted for while batching the energy.

This method emphasizes that the "important feature of SEA is the description of the vibration system as a member of a statistical population or ensemble [10]." Nevertheless, since it mainly deals with statistics, only approximate answers can be given in some-what measurable uncertainty level. in more extensive and more complex systems, this becomes more prominent, and errors accumulate up to the high level of uncertainty. Moreover, the frequency bands chosen may not contain enough modes (low modal density) to supply a fair estimation in some cases. Also, most designers know or can assess the loads that will act on their structure, and using a statistical

method to calculate the response, may yield unfitting results for the specific load regime.

As previously described, SEA deals with the storage and transfer of energy between components in a system. Therefore, to apply this method, one must understand, categorize, and assess the amount of energy stored in each component. The interconnections play a significant role in this analysis since they determine the rate and magnitude in which the energy disperses throughout the system. The simplest subsystem, for example, is a plate. The modes of different plates can be easily calculated, and the amount of energy stored in the plate is proportional to its dimensions and the corresponding modes. Energy transfer between plates depends on the way the plates are interconnected - torsional loads in one plate can transfer to shear modes in the other and vice versa, depending on the orientation they are connected to and the method.

A simplistic MATLAB^{TM} based computational tool was developed by Johansson and Connell at Chalmers University of Technology, Sweden [8]. It uses the basic assumptions of SEA and the acoustic vibration impedance of different plates and cavities.

Concluding, statistical energy analysis is a possible method to deal with random vibrations and their effect on the system. However, this method does not show any advantage over other methods and quickly accumulates uncertainties for an extensive convoluted system with various loading conditions.

1.3 Past Work and Motivation

Today, many ships are equipped with predictive maintenance systems that monitor power consumption, vibrations, and noise. One example is the NILM [1] developed in the Electromechanical Systems Group at MIT. By monitoring vibrations and their behavior, different conclusions on the state of the system can be detucted [7].

Past research conducted in the Electromechanical Systems Group generated a model that connects between system and base vibrations using system-mounted ac-

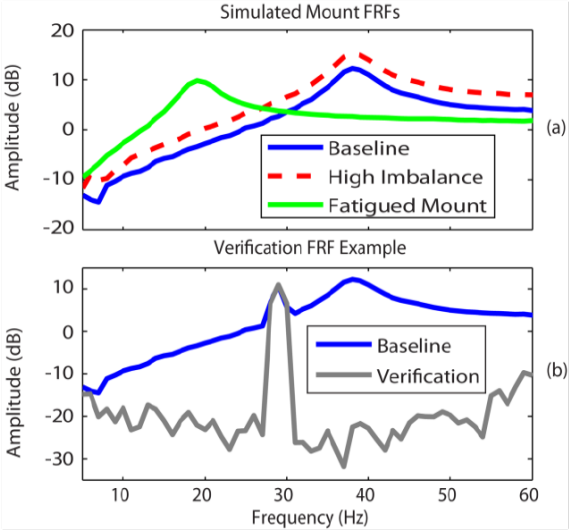

Figure 1-3: System Response Shift due to Loading Conditions, taken from [15]

celerometers [15]. Assuming a simplistic mass-spring-damper model, one can predict the vibration profile on the base of a system using accelerometers mounted on the system. Moreover, if the vibration profile changes, it can be easily deducted if the change source is in the mounting system or the mount itself. For example, Figure 1-3 shows the Frequency response spectrum due to different loading conditions created on a system: an imbalance in the system will increase the general magnitude of vibrations, yet with no change to the resonance frequency. Mount fatigue, or failure, will change the resonance frequency without necessarily changing the magnitude of vibrations. Thus, the springs' nature can be derived to estimate the vibration profile in the base - both in magnitude and frequency.

Consequently, monitoring the vibration profile on a source, such as a motor, can indicate the profile on its base. Knowing the magnitude and distribution of the vibrations on a plate, one can predict the amount of radiated noise to the environment using one of the methods as mentioned earlier. Thus, predictive maintenance systems that monitor vibrations can theoretically be also used to predict the radiating noise profile of the ship, without further resources such as Own-Noise Accelerometers (ONA) or frequent use of acoustic ranges. This work will attempt to explore this path and will provide possible solutions to the presented need.

Chapter 2

Experimental Validity of the Theoretical Models

As mentioned in the previous chapter, both Statistical Energy Analysis and Finite Element Method are computationally consuming and require high detailing. Nevertheless, the resulting data will require experimental validation due to manufacturing imperfections, variant plate properties, and other factors. Therefore, in preparation for any future modeling of a marine vessel, a simplistic model should be examined and compared to the known methods.

Consequently, a simple metal cabinet was chosen, as depicted in figures 2-1 and 2-2. As the following subsections will describe, the cabinet was modeled using the existing theoretical models, later compared to vibration measurements gathered during experiments. This section describes, presents, and compares theoretical and experimental results on the shown metal cabinet.

An experiment using two speakers attached to the right and bottom plates, operating in different frequencies and magnitudes, was executed to validate the theoretical models and their linearity. section 2.2 will, later on, describe the results and experimental methods.

Figure 2-1: Metal Cabinet used for Modeling and Experiment, Assembled View

Figure 2-2: Metal Cabinet used for Modeling and Experiments, Internal View

2.1 Cabinet Model

The cabinet was modeled as a five-walled chamber, consisting of five plate-types and three beam-types, as shown in figure and 2-3. Both beams and plates were manufactured using bent and welded steel sheets of 2.5mm thickness. The drawer rails were neglected in the modeling since they are connected to the vertical beams using screwed joints. Further drawings and illustrations of the cabinet appear in Appendix A. The plates and beams were classified as follows (ref. Figure 2-4):

1. Cover Plates - Bottom and Top, 3 bends, 4 sections.
2. Front U-Beams - Bottom and Top, 4 bends, 5 sections.
3. Front Vertical Beams - Left and Right, 4 bends, 4 sections.
4. Side Plates - Left and Right, no bends, 1 section.
5. Back Supporting Plates - Bottom and Top, 1 bend, 2 sections.
6. Back Vertical Beams - Left and Right, 4 bends, 4 sections.
7. Back Side-Plates - Left and Right, 2 bends, 3 sections.
8. Back Center-Plate - Single, 4 bends, 5 sections.

Each section of the cabinet's parts was disassembled into sub-plates, connections, and cavities to be analyzed using SEA, as detailed in Appendix A.

2.1.1 Finite Element Model

As mentioned previously, Finite Element Analysis (FEA) allows approximate computation of reactions using numerical methods. Using ANSYS Workbench^{TM} as an FE analysis tool, the actuation speakers were modeled as steel disks, with the same contact diameter and thickness corresponding to their weight, attached to the middle of the activated plates for the simulation.

Additionally, the base wheels of the cabinet were modeled as simple plates for ease of implementing the border conditions, where three arbitrary wheels acted as frictionless support, and the fourth one acted as a fixed support frame of reference.

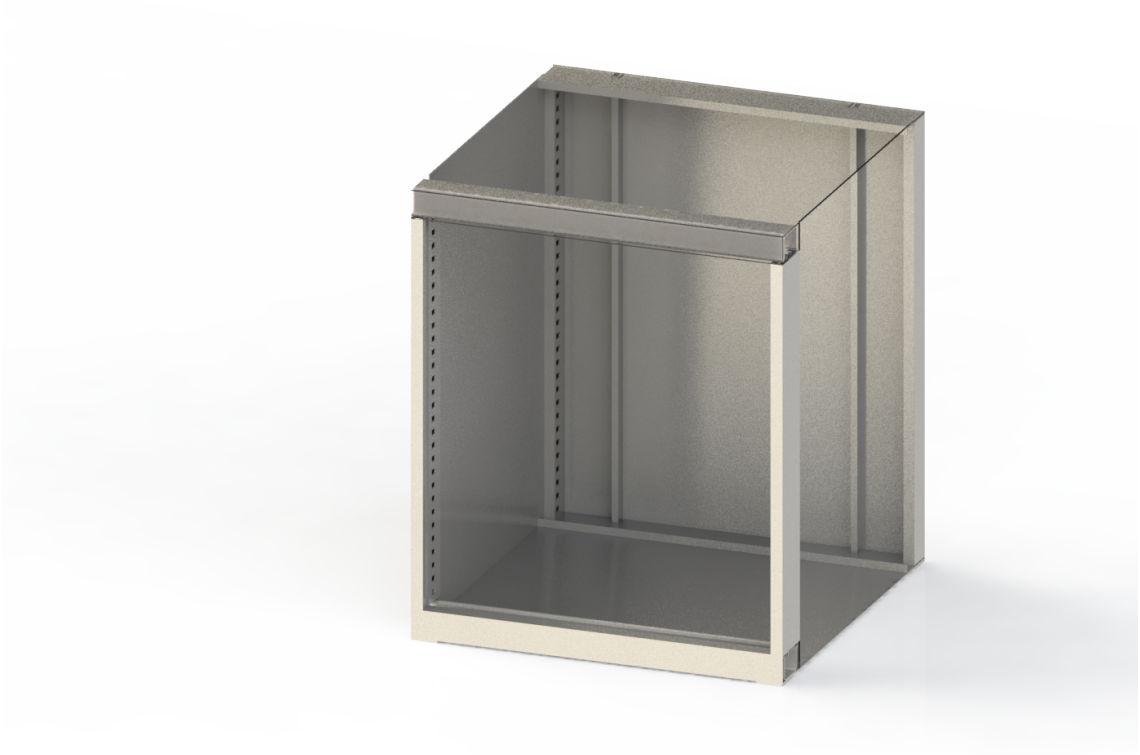

Figure 2-3: Cabinet 3D Model, Rendered (Transparent Sides)

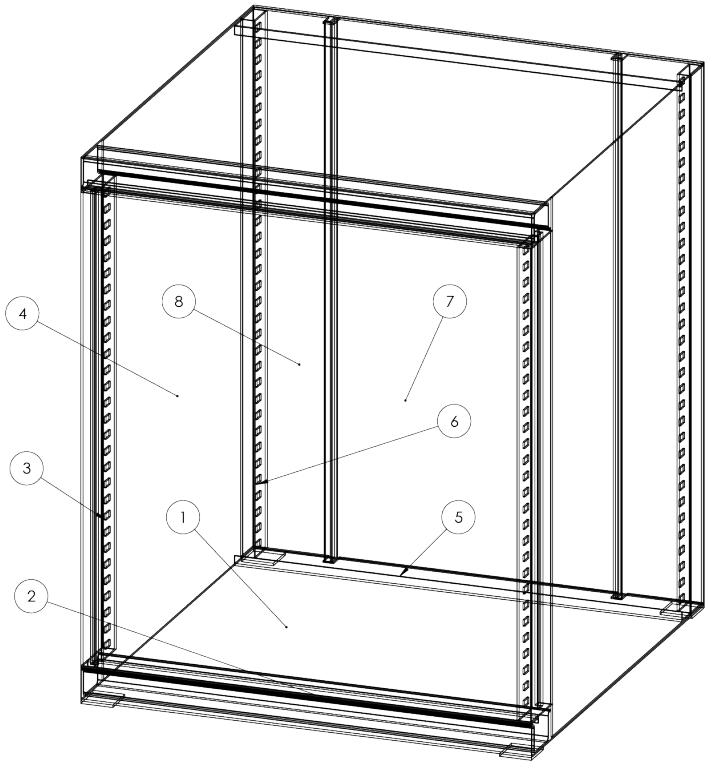

Figure 2-4: Cabinet 3D Model, Drawing

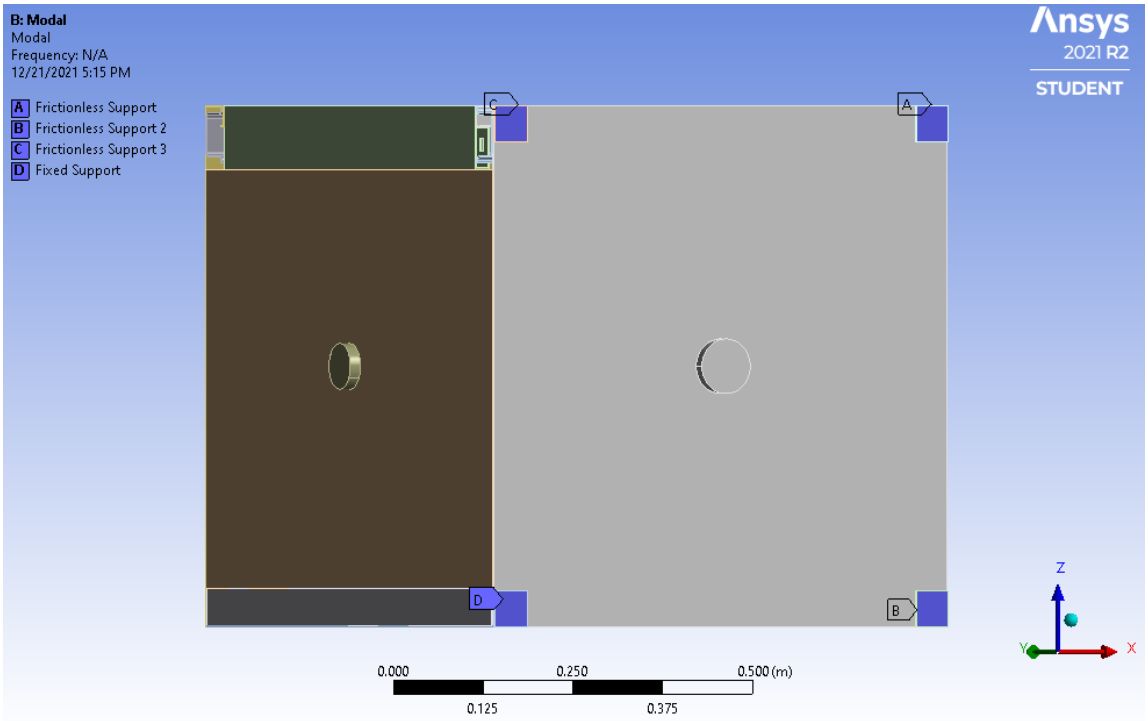

Figure 2-5: View of both Side and Bottom of the ANSYS Cabinet Model

The results did not show any sensitivity to the selection of the fixed support. Figure 2-5 shows both the side and the bottom of the cabinet model with the speakers and the labeled supports.

The meshing process of the model was done manually due to the high detailing needed around the vertical beams and the precision needed around the actuating speakers. In addition, the connections between the plates also required more delicate meshing, especially the contact areas between the back-plate sections, as shown in Figure 2-6.

First, the modes of the system were computed using the "Modal Analysis" module, resulting in a total of 840 modes between 40Hz and 4000Hz. Due to memory and computation power limitations, the calculation range was capped at 4000Hz. A 1/3 octave histogram of the vibration modes can be seen in Figure 2-7. The histogram shows that more modes appear in higher octaves, yet higher octaves span through a broader range; therefore, the modal density does not change significantly.

Later on, the results from the modal analysis were transferred to the "Harmonic

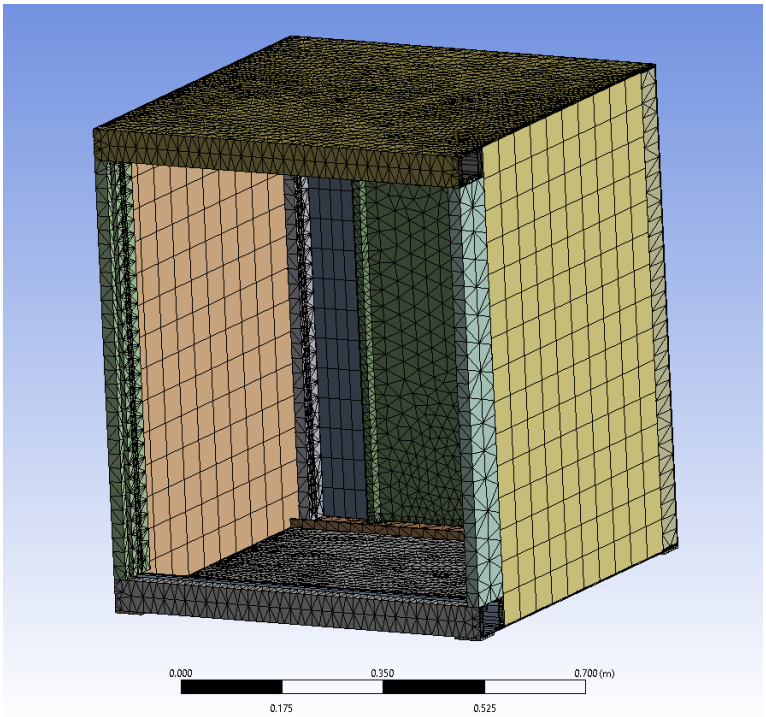

Figure 2-6: Mesh Results of the Finite Element Model

Response" module to compute the response amplitude for a range of frequencies within the spectrum, as presented in Figure 2-8. Observing the 1/3 octave power amplitudes, one can notice a similarity in amplitude in the higher frequency range. In comparison, there is less amplification for the medium back-plate in the lower frequency range than the bottom and opposite plate, probably due to the difference in size and stiffness. Moreover, there is a certain correlation in the resonance frequencies in the entire spectrum plot, which are more prominent in the lower frequency range than the high-frequency range.

Another aspect needed to verify is the linearity of the model in terms of excitation amplitude response. The calculations on the model were conducted on different magnitudes of excitation, resulting in linear, as presented in Figure 2-9.

2.1.2 Statistical Energy Analysis Model

Unlike FEA, this method does not treat the entire volume as a sum of finite and minor elements. Meaning; this method treats the system as a sum of oscillators, where

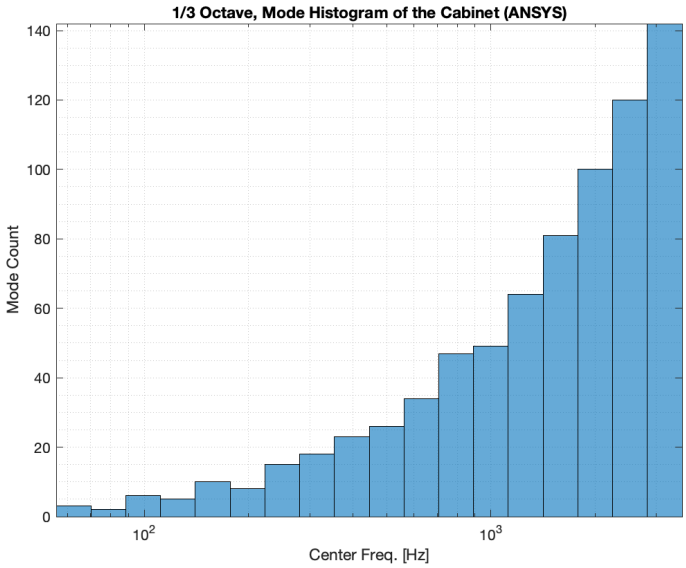

Figure 2-7: 1/3 Octave, Mode Histogram of the Cabinet

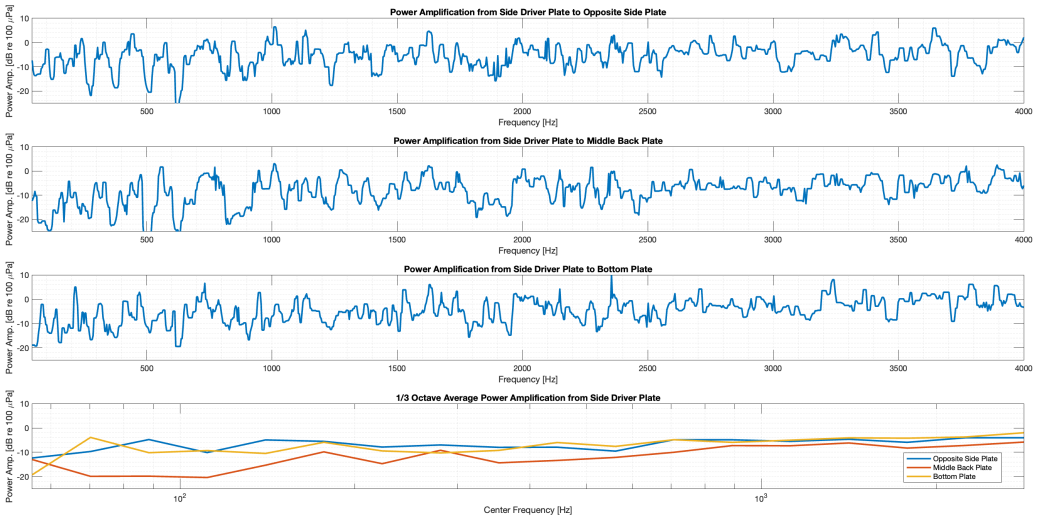

Figure 2-8: Power Amplification Values using FEA

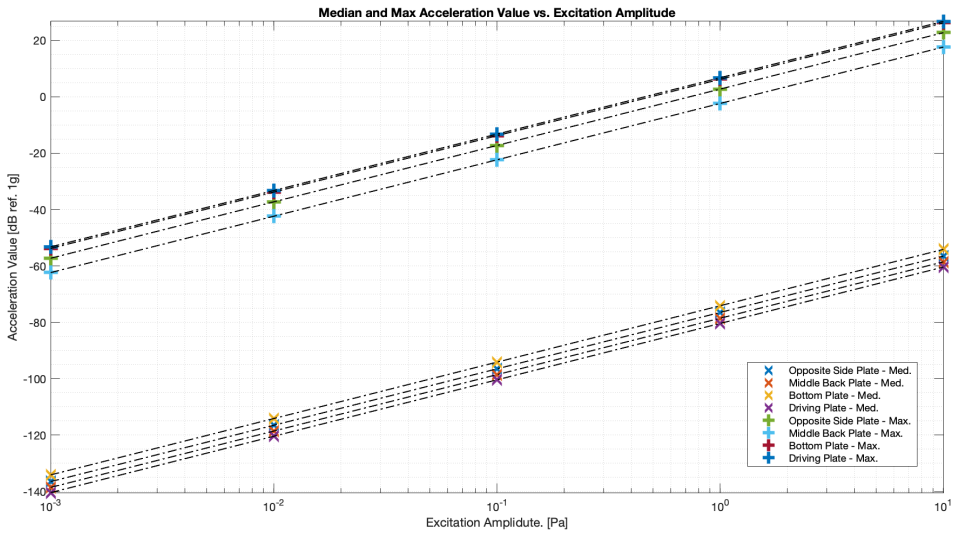

Figure 2-9: Simulated Acceleration Values for Different Actuation Amplitudes

each oscillator is defined by its energy, material, dimensions, and modal density. Additionally, the interaction between the oscillators is defined by the size of their interface and its efficiency.

For this calculation, as mentioned above, the SEA calculation tool [8] was used. Each plate was divided into smaller sections, reaching 51 plates. Moreover, the central air cavity trapped between the walls and the minor air cavities trapped inside the hollow beams adds an extra of 5 cavities, totaling 56 oscillators. Additionally, 176 plate-to-plate connections and 35 plate-to-cavity connections were modeled. Detailed modeling data can be found in Appendix A.

Since SEA treats the entire system as a statistical ensemble, no system modes were calculated as in FEA. Therefore, When comparing the whole spectrum power amplification of the system, as presented in Figure 2-10 a surprising trend appears, where the opposite side-plate has a minor gain, wherein the FEA method the most negligible average gain was presented at the middle back-plate. Moreover, comparing the results of the SEA and FEA shows no correlation in magnitude throughout the spectrum, both in the complete spectrum analysis (Fig. 2-10) and the 1/3 Octave spectrum analysis (Fig. 2-11).

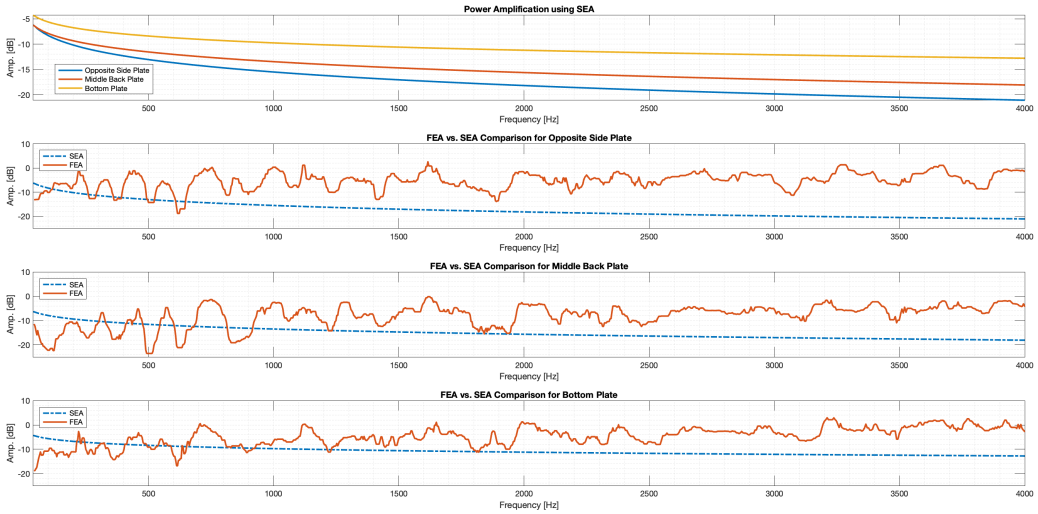

Figure 2-10: SEA Simulation Results and Comparison to FEA solution

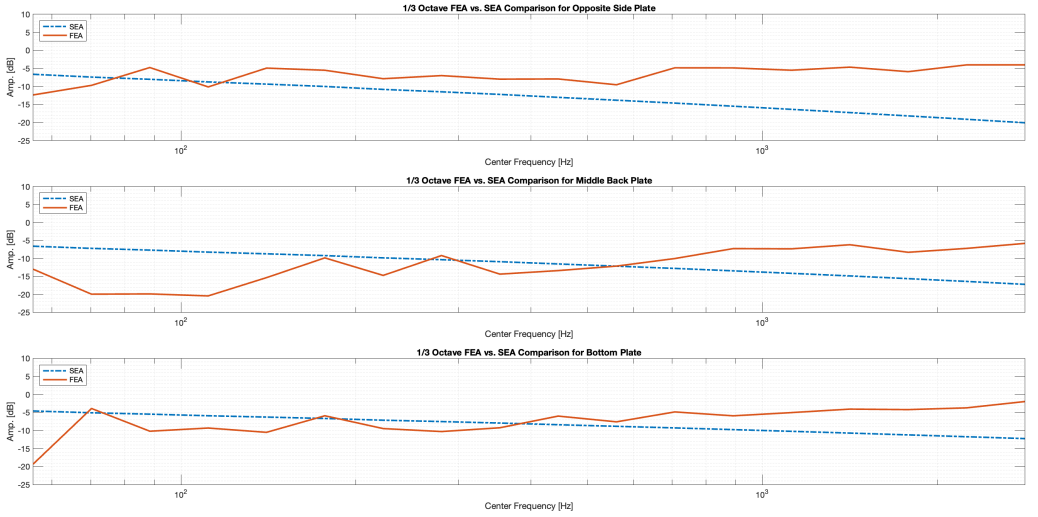

Figure 2-11: 1/3 Octave Comparison Between SEA and FEA

2.1.3 Conclusion

As shown previously, each method has its relative advantages. For example, while FEA does require high computational power and computation time, the results obtained contain high-resolution data about the system's behavior in different frequencies. Moreover, FEA can specify the modes of the system and point out the prominent ones, helping the designer to focus their effort on a specific range. On the other hand, SEA is easier to model and calculate using free and available software, without any additional tools.

However, even though both FEA and SEA simulations were conducted in parallel using the same physical properties of the system, both methods did not yield similar results. Both did not agree on the power gain between the driving and driven plates: while SEA showed a lower gain in higher frequencies, FEA demonstrated otherwise. Moreover, while FEA pointed out the most significant gains will be in either the bottom or opposite side-plate, SEA predicted that the bottom plate would be the most prominent one while the opposite side-plate would be the least prominent one.

Therefore, to decide which method is preferable is it necessary to conduct validation through experiment.

2.2 Experimental Validation

An experimental apparatus was designed involving two speakers. One speaker creates a constant ambient noise, where the frequencies constructing that noise were calculated according to:

$$S(t) \quad = \quad \sum_{i=1}^{n} \frac{1}{n} sin(100P_n \cdot 2\pi t) \tag{2.1}$$

Whereas P_n represents the n prime numbers up to 40, meaning $(2, 3, ...37)$. This way, all amplitudes will equal, and no harmonics or sub-harmonics will combine.

Additionally, a different speaker will scan the frequency range on a constant amplitude from 40Hz (the first mode according to the FEA) up to 4000Hz with increments

of 5Hz. For convenience, we shall refer to the ambient noise speaker as "Speaker A" and the frequency scanning speaker as "Speaker B." The locations of the speakers remained constant along with the experiment, and both were placed on the right-hand side plate and the bottom plate, switching roles between experiments. Meaning, in half of the experiments, speaker A was on the side plate while the speaker on the bottom plate was scanning, and vise-versa. As Table 2.1 below presents, a total of 10 experiments were conducted (in addition to a calibration experiment). Each experiment differs by the speakers' magnitude of operation (presented in full-scale percentage) or its location.

Exp.	Speaker A pos.	Speaker B pos.	A Mag.	B Mag.
1	Side-Plate	Bottom-Plate	100%	0%
2	Side-Plate	Bottom-Plate	75%	25%
3	Side-Plate	Bottom-Plate	50%	50%
4	Side-Plate	Bottom-Plate	25%	75%
5	Side-Plate	Bottom-Plate	0%	100%
6	Bottom-Plate	Side-Plate	100%	0%
7	Bottom-Plate	Side-Plate	75%	25%
8	Bottom-Plate	Side-Plate	50%	50%
9	Bottom-Plate	Side-Plate	25%	75%
10	Bottom-Plate	Side-Plate	0%	100%

Table 2.1: Cabinet Speaker Experiment Plan

This split serves three roles: foremost, experiments 5 and 10 allow constructing a full spectrum frequency-gain graph from the bottom or side-plate to the other plates. The second role is shown in experiments 1 and 6, where the frequency-gain model can be tested on another input to validate its accuracy. Finally, experiments 2-4 and 7-9 can test the system's linearity. The validation and analysis process of the experimental method is shown in Figure 2-12 where the PSD is either computed for "Full Spectrum" or for the 1/3 octave bands.

Concluding this part, accelerometers were placed behind each speaker and in the center of the back and opposite sides. All accelerometers were connected to the puck [7] and were sampled simultaneously at a rate of 20833Hz.

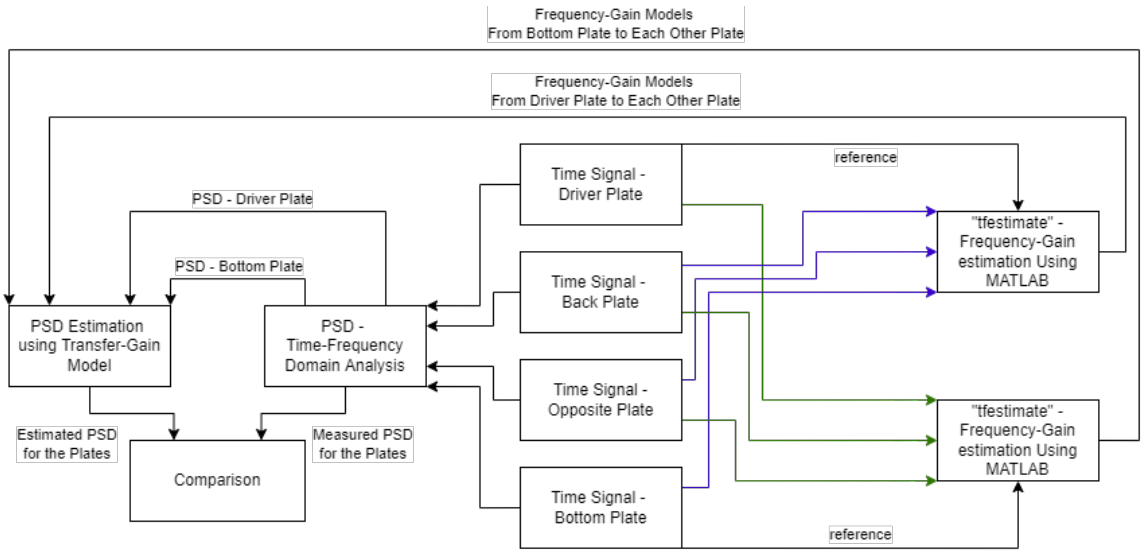

Figure 2-12: Experimental Estimation and Validation Process Diagram

2.2.1 Results

Experiment No. 10's time-series graphs and spectrograms for the driver plate and the opposite plate are shown in Figures 2-13 and 2-14. At full power, speaker B exerts an acceleration of a maximum of 2g for the driver plate, compared to a maximum acceleration of 0.4g for the opposite plate. The scanning action of speaker B is presented in the sharp and prominent diagonal line with some sub-harmonics appearing underneath it. The origin of the sub-harmonics is not clear, yet it is assumed to be sourced at the sound amplifier and not in the structure itself.

The opposite plate's time-series graph and spectrogram during experiment No. 3 are shown in Figure 2-15. Observing the time-series signal, the amplitude of the vibrations differs over time (excitation frequency), and for this experiment, the maximum response is less than 0.2g. Using the spectrogram, one can easily concur that the reaction in the opposite plate consists of time-constant lines (ambient noise) and time-variant frequency.

Examining the spectrogram for the bottom plate during experiment No. 3 shows that although the most prominent signal component is the scanning produced by speaker B, traces of signal "A" appear, showing some amount of linearity.

The gain for each frequency (TF) was estimated using the MATLAB "tfestimate"

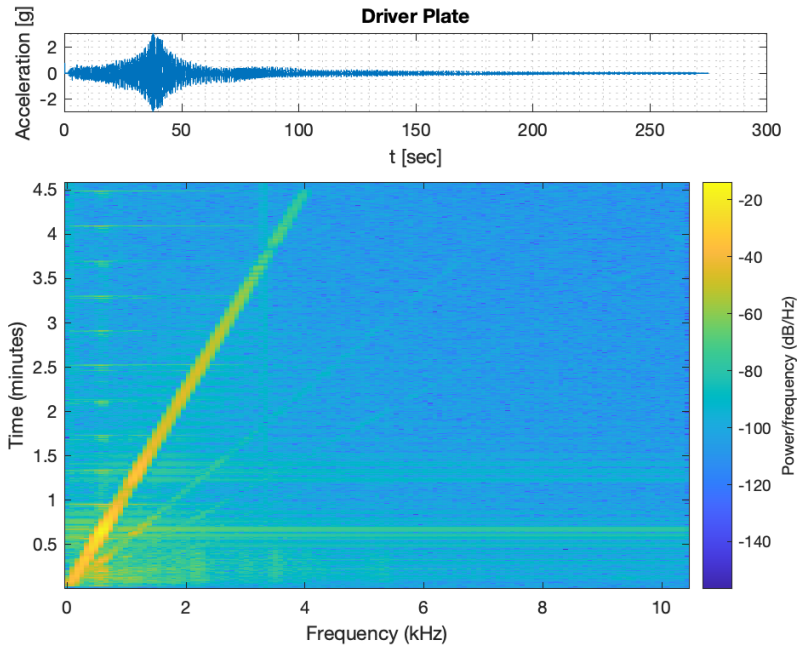

Figure 2-13: Driver Plate Acceleration Measurement and Spectrogram, Exp. 10

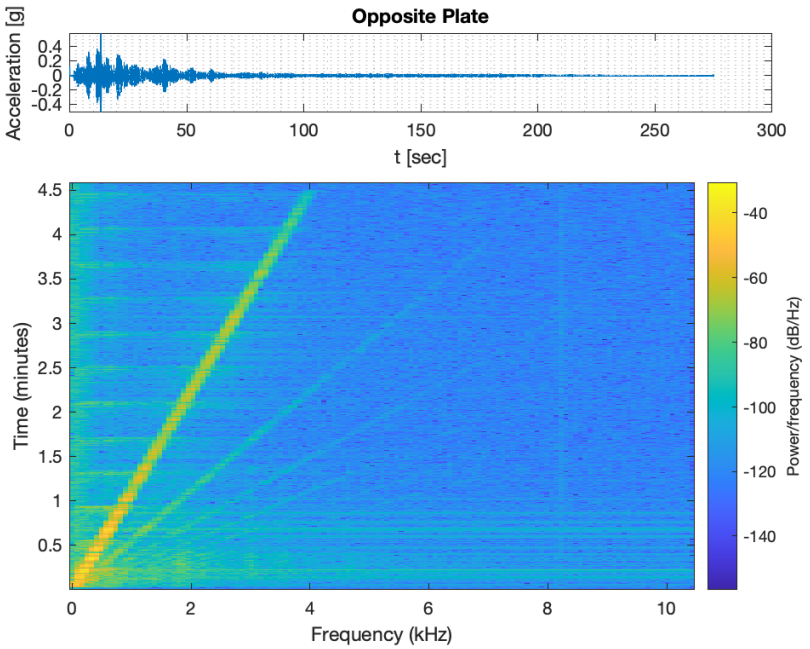

Figure 2-14: Opposite Plate Acceleration Measurement and Spectrogram, Exp. 10

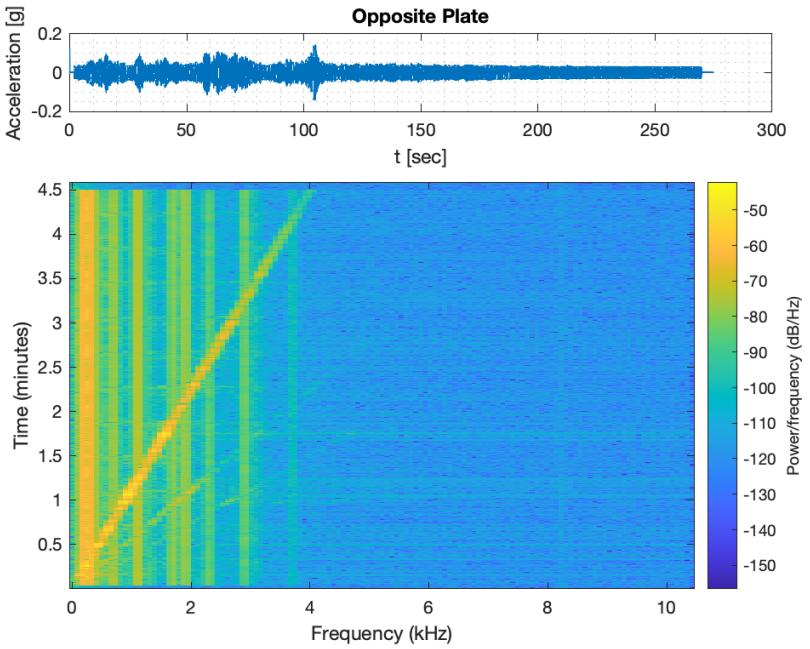

Figure 2-15: Opposite Plate Acceleration Measurement and Spectrogram, Exp. 3

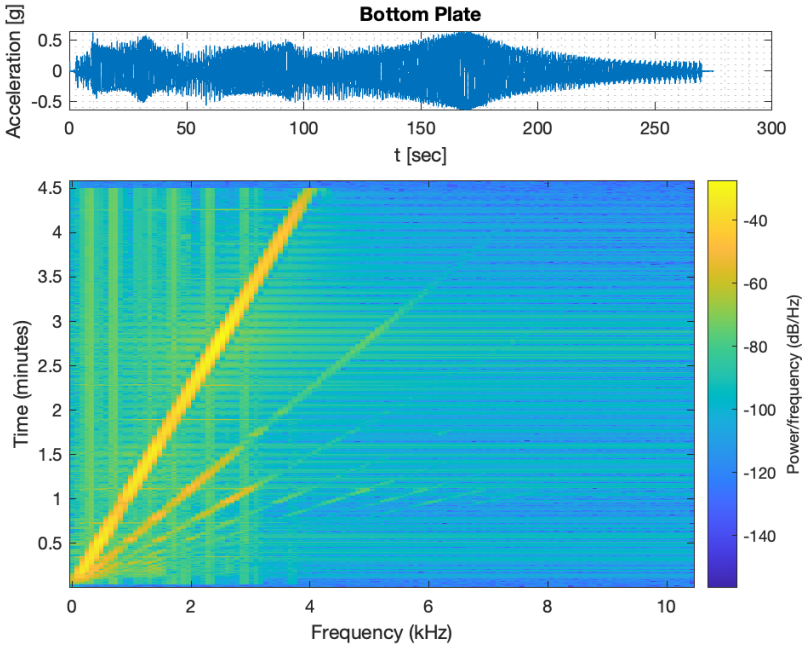

Figure 2-16: Bottom Plate Acceleration Measurement and Spectrogram, Exp. 3

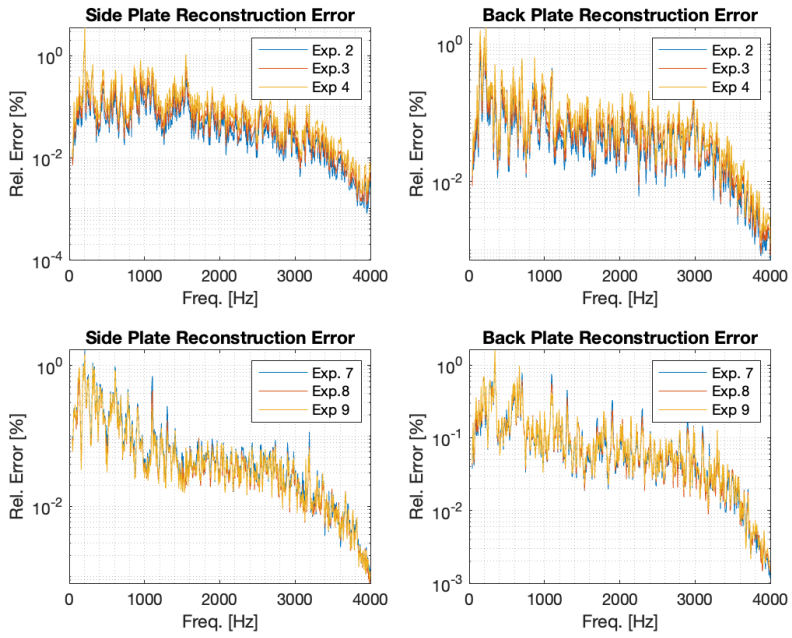

Figure 2-17: Reconstruction Error for the Cabinet Experiments

function for both the driver plate and the bottom plate. Using the estimated gain, the signals for the rest of the experiments was theoretically reconstructed and was compared to the measured values, resulting in the errors depicted in Figure 2-17.

Since the errors are lower than 1%, the y-axis in those graphs is presented in log-scale. The reconstruction errors show that using a simple experiment, one can easily estimate a frequency-gain graph of a simple system with high prediction accuracy. Moreover, the low reconstruction error allows us to assume that the estimated frequency-gain graph is indeed the valid one, for comparison with the results obtained in the SEA and FEA.

2.2.2 Comparison and Conclusion

Comparing the estimated gain with the FEA (Figure 2-18) shows a low correlation, ranging between 13% and 23%. Furthermore, although there is a general agreement in average magnitude, no correlating peaks were traced along with the range, meaning that the model prediction was inaccurate. The SEA analysis does not perform better, with a negative correlation and general disagreement on the gain levels, as presented

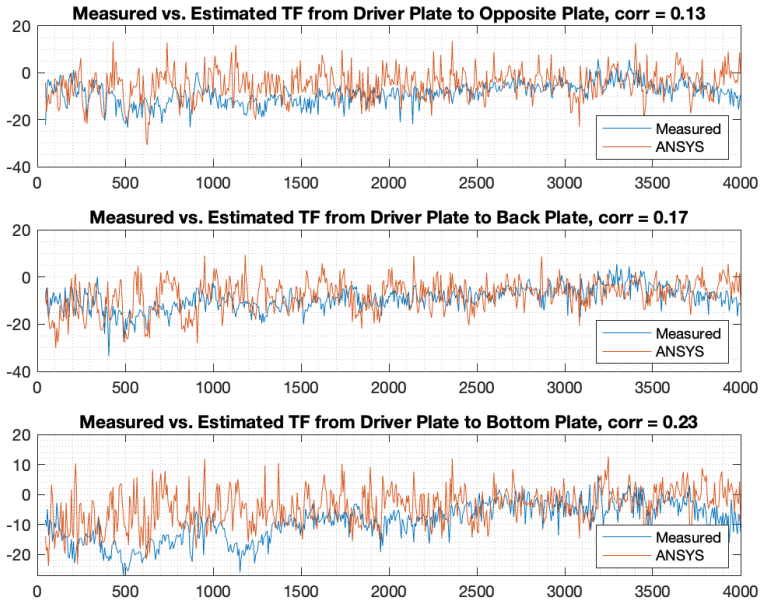

Figure 2-18: Comparison Between the Estimated Gain and FEA

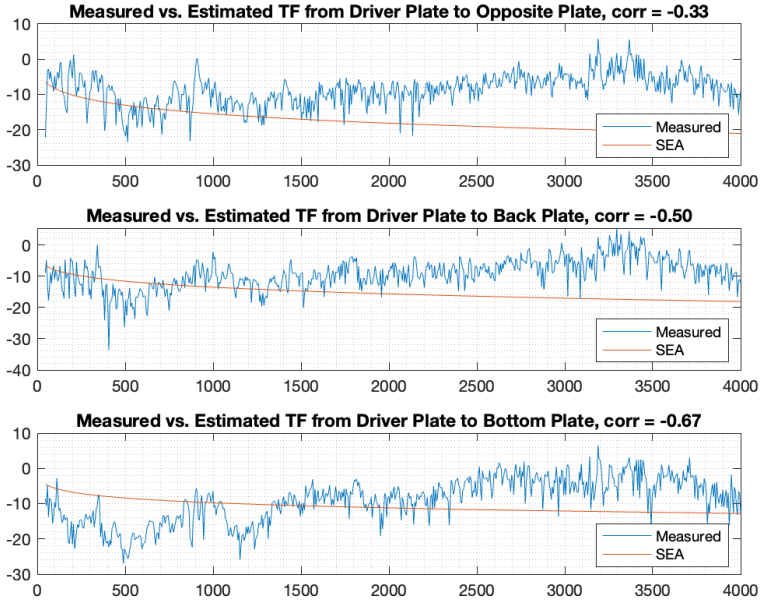

Figure 2-19: Comparison Between the Estimated Gain and SEA

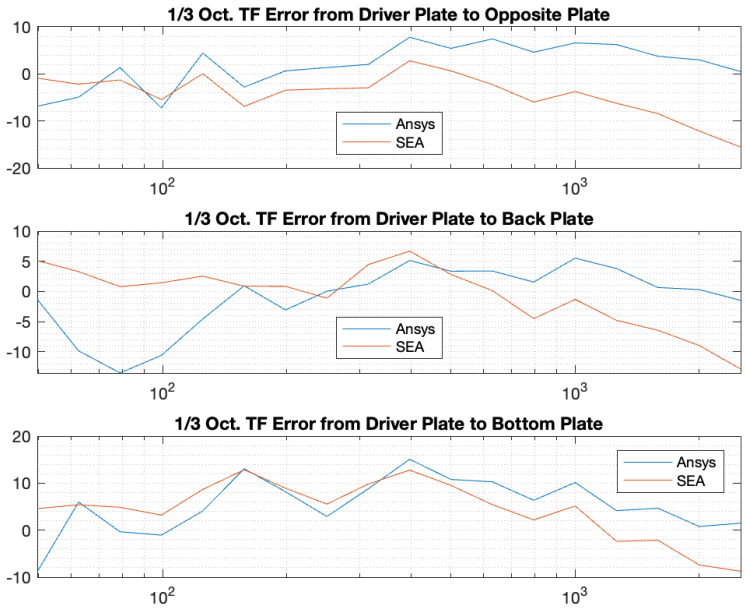

Figure 2-20: 1/3 Octave Error of FEA and SEA from the Estimated Gain

in Figure 2-19.

Comparing the gain error in the 1/3 octave range between FEA and SEA shows little-to-negligible better performance to SEA in lower frequencies and higher performance using FEA in higher frequencies. Although both generally off by about 10%.

Concluding, both types of analysis did not perform well predicting the actual gain of the system. This low performance is probably connected to modeling sensitivity and manufacturing errors such as plate thickness, uneven welding, residual stresses, and more. However, the low reconstruction errors show that a well-planned and controlled experiment can yield an accurate model. The main takeaway from this process is that even in a small and uncomplicated system, it is hard to determine the gain levels using both methods, and experimental methods are irreplaceable by them. Therefore, when willing to construct a frequency-gain model for a more complex system, the accuracy of these models is not assured.

Chapter 3

Test Ship Experiments

As a part of the constant research conducted by the Electromechanical Systems Group, different monitoring equipment was installed on a test ship anchoring in Boston. Therefore, the vibro-acoustic measurements for this research were conducted on this ship. The main targets of the experiments were as follows:

1. Build a gain model from a vibrating machine the environment.
2. Build a gain model from a vibrating machine to the hull plates.
3. Build a gain model from the hull plate to the environment.
4. Validate the models mentioned above using a set of experiments.

3.1 Experimental Plan

The leading rationale while planning the experiment was to choose machines that could be easily regulated and controlled, supplying different noise sources that can vary in magnitude or frequency. Additionally, the machines chosen had to be loud enough to prevail over the noise in Boston harbor and the ship itself.

Surveying the available machinery in the test ship led to two available systems: the fire pump and the air fan, accordingly marked in a green triangle and a blue circle in Figure 3-1. In addition, the AC unit operating near the starboard wall

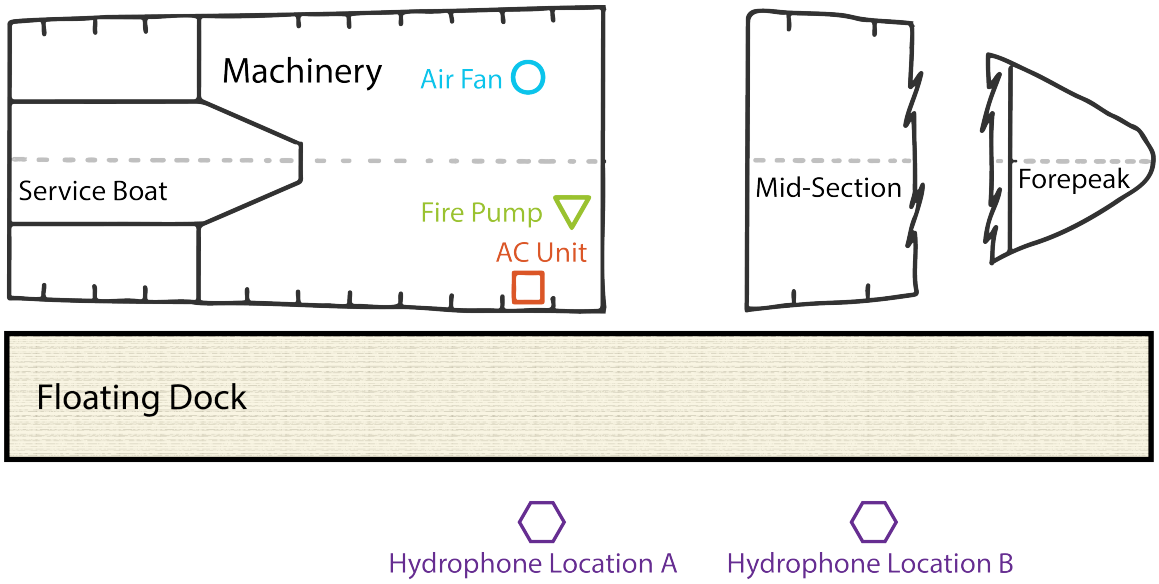

Figure 3-1: Unit and Hydrophone Location for the ship

of the machinery room (marked with a red square) was chosen to be monitored. Although the AC unit could not be manipulated for the course of the experiment, it was monitored since its monotonous vibrations may provide a control experiment for validation.

The hydrophone used in the experiment was placed in two different locations marked "A" and "B," submerged 10 feet under the surface using a buoy. Location "A" of the hydrophone was 12 feet (4 meters) off the starboard side, aligned with the AC unit, and location "B" was also 12 feet off the starboard side aligned with the forward part of the ship. Frame numbers are purposely not mentioned.

For accuracy, three identical "Wilcoxson" accelerometers were used and sampled together: the first two were installed on the central axis of vibration machinery, and one was placed on the hull itself. Additionally, a hammer tap was applied on the hull to help synchronize between the accelerometers and the hydrophone.

The hydrophone used was "Cetacean Research Tech. C-57" with a linear frequency range ($\pm 3dB$) of 15Hz - 45kHz. Using the "TASCAM DR-22WL" recorder, the system had an adequate sensitivity of $-176\ dB,\ [re.\ 1V/\mu Pa]$. Further technical data can be found in Appendix B.

A total of 21 experiments were planned as displayed in Table 3.1. Experiments

No.	Hyd. Loc.	System	Measurement	Length [s]
1	"A"	AC Unit	Ambient Noise	20
2	"A"	AC Unit	Regular Operation	40
3	"A"	Fire Pump	Ambient Noise	20
4	"A"	Fire Pump	On-Steady-Off 1	60
5	"A"	Fire Pump	On-Steady-Off 2	60
6	"A"	Fire Pump	Open & Close Discharge	60
7	"A"	Air Fan	Ambient Noise	20
8	"A"	Air Fan	On-Steady-Off 1	60
9	"A"	Air Fan	On-Steady-Off 2	60
10	"A"	Air Fan	Open & Close Intake 1	60
11	"A"	Air Fan	Open & Close Intake 2	60
12	"B"	Air Fan	Ambient Noise	20
13	"B"	Air Fan	On-Steady-Off 1	60
14	"B"	Air Fan	On-Steady-Off 2	60
15	"B"	Air Fan	Open & Close Intake 1	60
16	"B"	Air Fan	Open & Close Intake 2	60
17	"B"	Fire Pump	Ambient Noise	20
18	"B"	Fire Pump	On-Steady-Off	60
19	"B"	Fire Pump	Open & Close Discharge	60
20	"B"	AC Unit	Calibration	20
21	"B"	AC Unit	Regular Operation	40

Table 3.1: Test Ship Experiment Table

1-11 were conducted while the hydrophone was placed in location "A," and the rest for location "B." Each sub-series of the experiment was made on the three systems. At the beginning of each sub-series, a 20 second long "ambient noise" experiment was conducted for further comparison. The first sub-series in location "B" was conducted on the air fan for better measurement accuracy and time-saving since accelerometers were already mounted on it.

To validate repeatably, measurements on the AC unit were done twice: once for "ambient noise" like the rest of the experiments and once for regular operation, later to be compared. Later on, when the accelerometers were moved to the fire pump, ambient noise was measured again for 20 seconds. After that, two repetitive measurements in which the pump was turned on, remained in steady operation, and then turned off were conducted. This was made to evaluate the gain graph throughout the entire spectrum of operation, in both frequency and magnitude. Eventually,

another experiment where the discharge valve of the fire pump was opened and closed during steady operation to validate the predictability of the gain function.

A similar method of experiments was conducted on the air fan. In this sub-series, the fan was turned on, operated in a steady-state for about 30 seconds, and then turned off. The experiment was conducted twice each time. Similarly, the fan's intake was blocked and unblocked several times during its steady-state operation to validate the evaluated gain function. This method was also repeated in location "B" of the hydrophone. The measurements were halted a few times during the series of experiments due to a passing ship that generated noise.

3.2 Results and Discussion

3.2.1 Time Series Signals & Spectrograms

The following illustrations present the spectrograms for a selected number of experiments. Figure 3-2 shows the time signal with the appropriate 1/3 octave spectrogram for the first two experiments. Examining the spectrogram, it seems that the general noise levels are in the range between 1-5 kHz. Although the AC unit was working monotonously, the signal measured in the hydrophone seems to oscillate with some prominent "shocks." Comparing it to Figure 3-3, the signal appears "cleaner," monotonous, and consistent. This was probably due to the inner position of location "B," which is less exposed to the harbor's noise. This behavior can also be noticed while comparing the air fan-related noise measurements for both locations (Figures 3-4 and 3-5).

Examining the fire pump measurements for location "B" (Figure 3-6) shows that while operating, the noise from the fire pump is noticeable and prominent over the noise. Moreover, general amplitude changes can be observed in the "open-close" experiment, where the noise amplitude slowly declines and then inclines around the 30 seconds mark. The slight disturbance around the 30 seconds mark is the valve hitting its dead end, as heard in the sound files. Comparing the hydrophone signal to

the vibration measurement on accelerometer No. 1 for the "open-close" experiment does not show any signs of a change in amplitude at first sight.

Regarding the air fan measurements, the accelerometer data presented in figures 3-8 and 3-9 indeed shows a notable change of vibration for both the "on-steady-off" and the "open-close" experiments. Nevertheless, no visible change can be observed, as demonstrated in figures 3-4 and 3-5, which may suggest the noise does not prevail. However, although not visible to the human eye, further analysis might present that these vibrations are detectable.

Finally, to determine the prominence of the vibro-acoustic patterns, one must examine the time-averaged magnitude levels of the signals and compare them to the "ambient noise" levels. As demonstrated in Figure 3-10, the vibrational pattern in the fire pump is very prominent in the fire pump measurements, compared to the air fan. However, while the vibration magnitude increases equally throughout the entire frequency range for the fire pump, a prominent vibration around 1kHz is observed while the air fan-operated. Unsurprisingly, the vibration magnitudes for the AC unit do not differ. However, when comparing the time-averaged magnitudes at the hydrophone (figure 3-11), it shows almost no difference between operation modes for the air fan, especially in location "B," where it was less noisy.

3.2.2 Frequency Band Analysis

Deep-diving into the 1/3 Octave Spectrograms, each frequency range must be analyzed to determine which can demonstrate the system's behavior in the most compatible manner. For example, Figures 3-12 to 3-14 show time series magnitude analysis per 1/3 octave center frequency for experiment 18. The moment in which the pump turned on and off is visible in all frequency ranges, measured with accelerometer no.1 (Fig. 3-12). However, When observing the signal obtained from accelerometer no.3, which is mounted on the hull, no clear indication of the pump's operation is shown. Nevertheless, the hydrophone does detect the pump's operation, as seen in Figure 3-14. Listening to the sound file for this measurement demonstrates a mix of flow and machine noises that can be heard clearly.

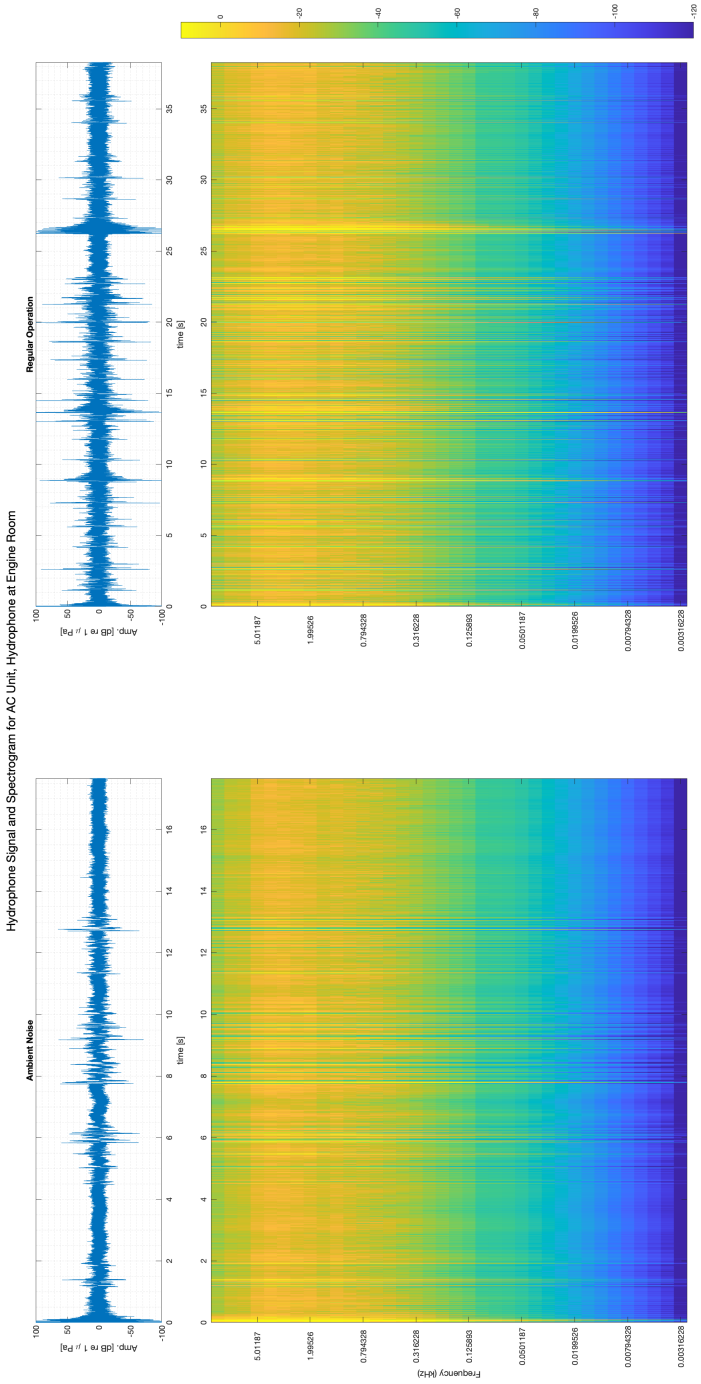

Figure 3-2: AC Unit Hydrophone Measurement Set, Hydrophone at "A"

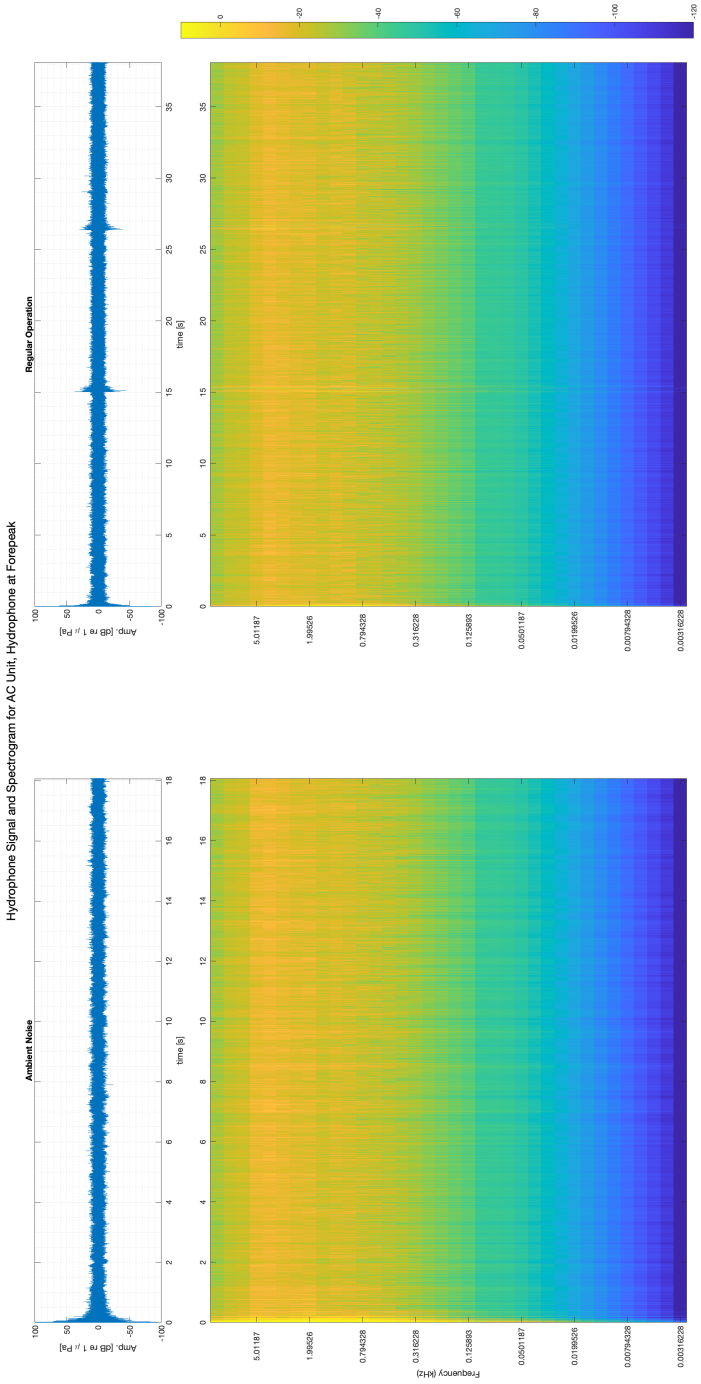

Figure 3-3: AC Unit Hydrophone Measurement Set, Hydrophone at "B"

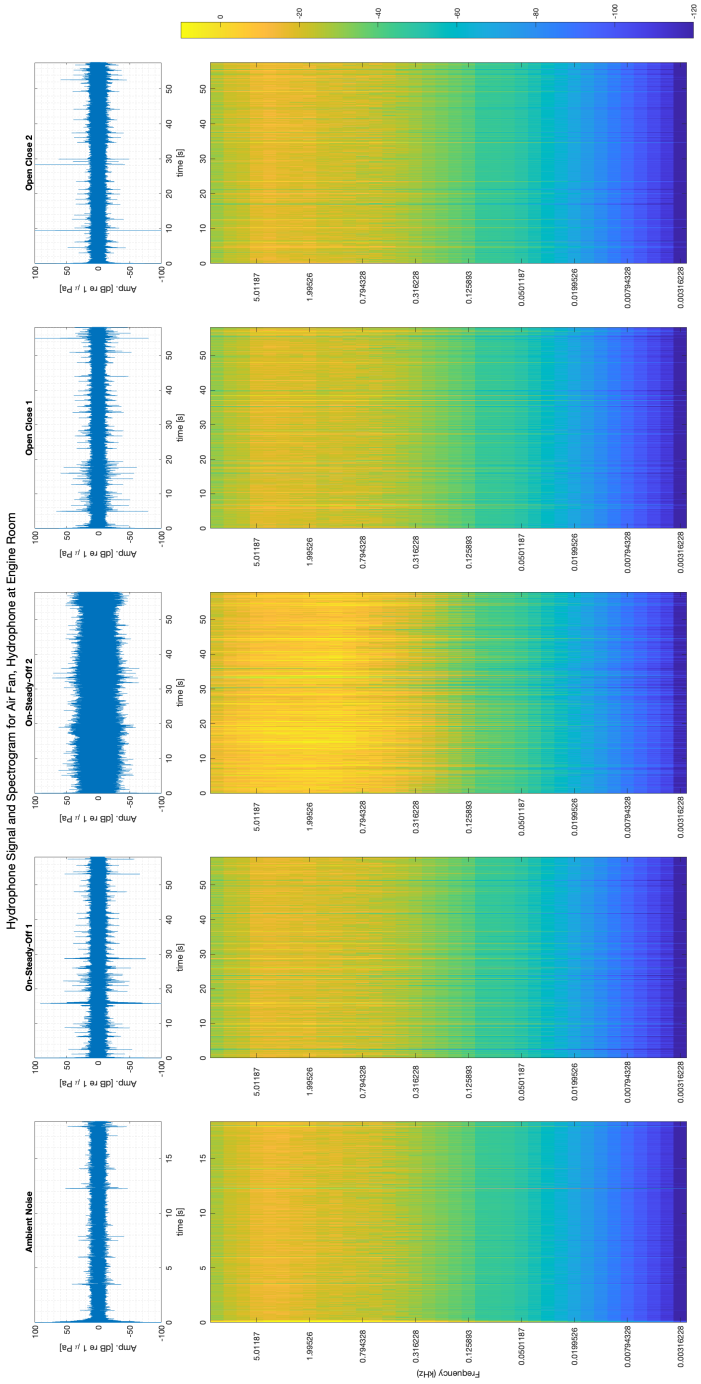

Figure 3-4: Air Fan Hydrophone Measurement Set, Hydrophone at "A"

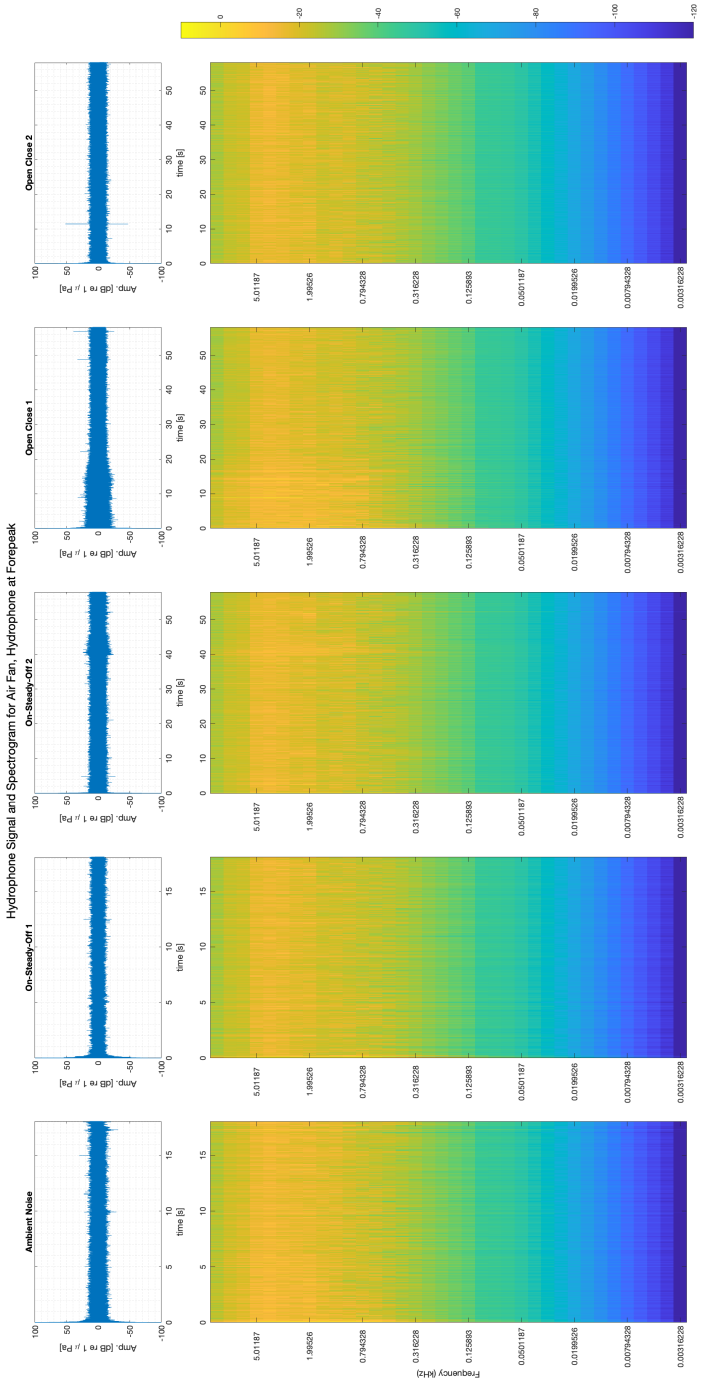

Figure 3-5: Air Fan Hydrophone Measurement Set, Hydrophone at "B"

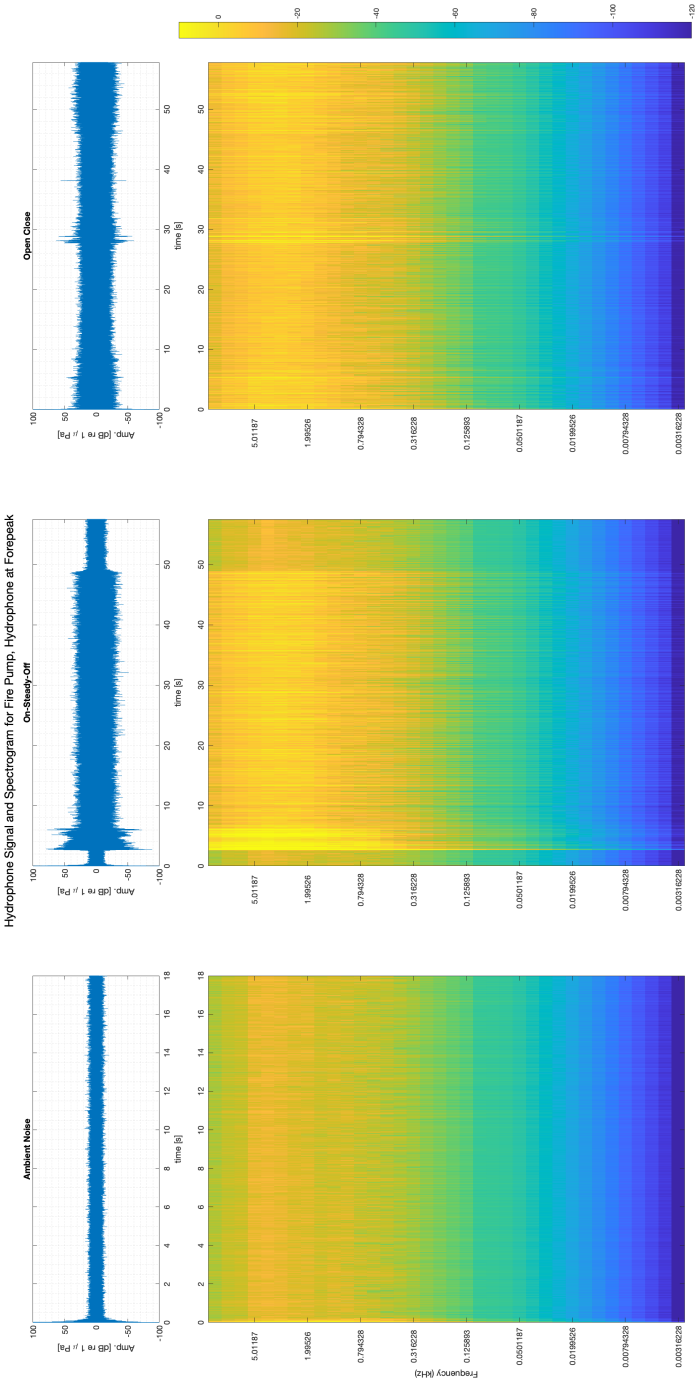

Figure 3-6: Fire Pump Hydrophone Measurement Set, Hydrophone at "B"

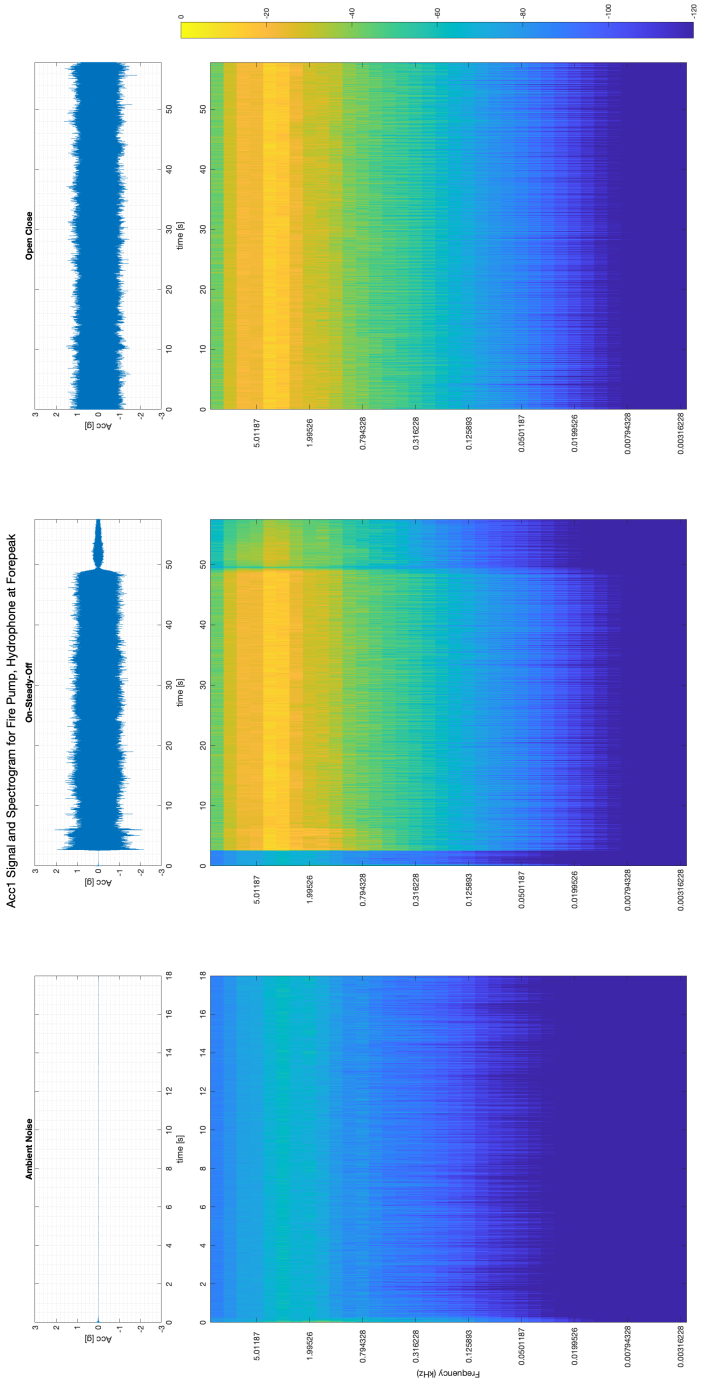

Figure 3-7: Fire Pump Accelerometer No. 1 Measurement Set, Hydrophone at "B"

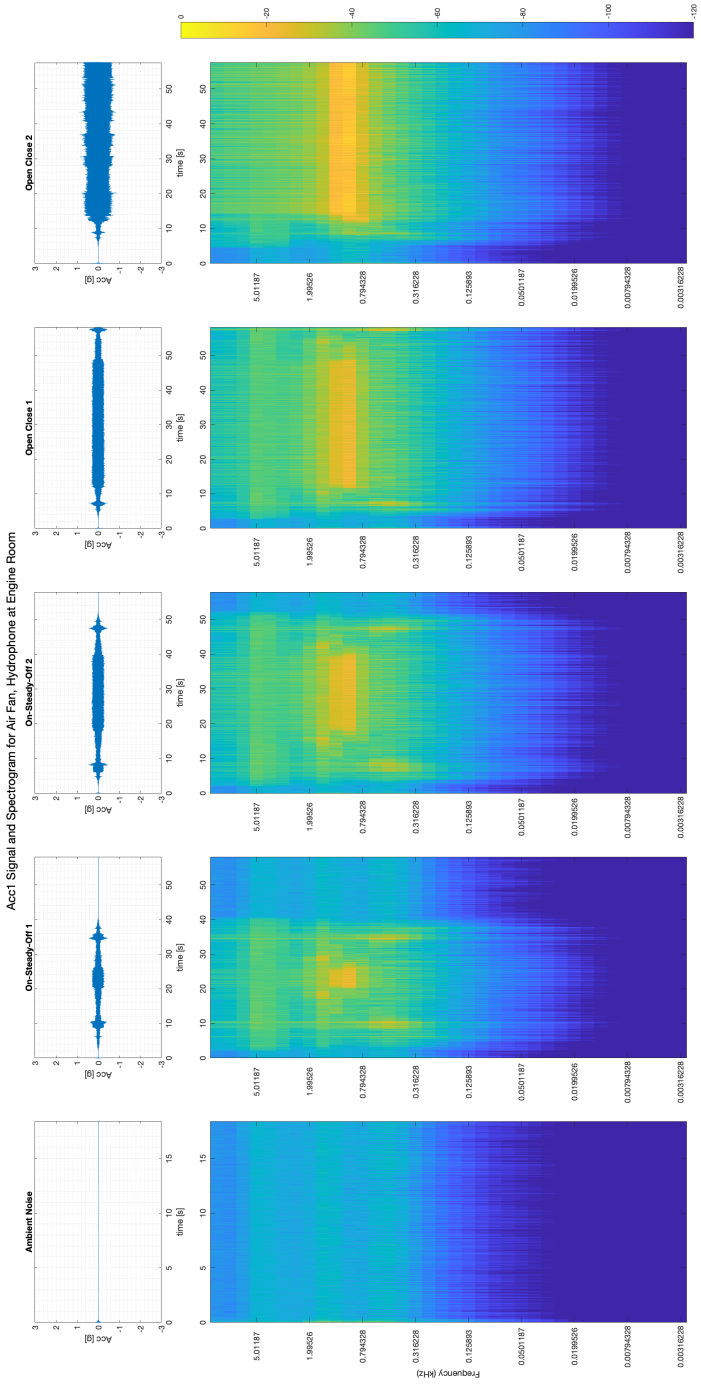

Figure 3-8: Air Fan Accelerometer No. 1 Measurement Set, Hydrophone at "A"

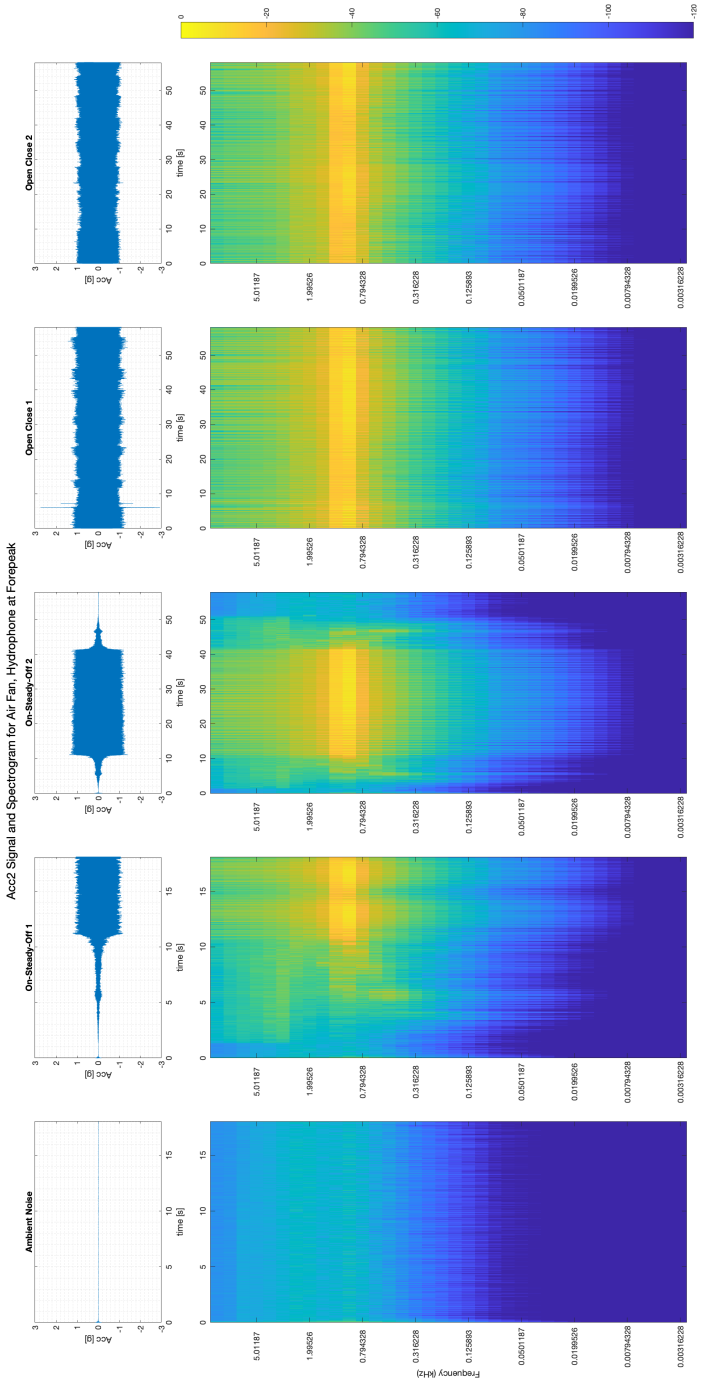

Figure 3-9: Air Fan Accelerometer No. 2 Measurement Set, Hydrophone at "B"

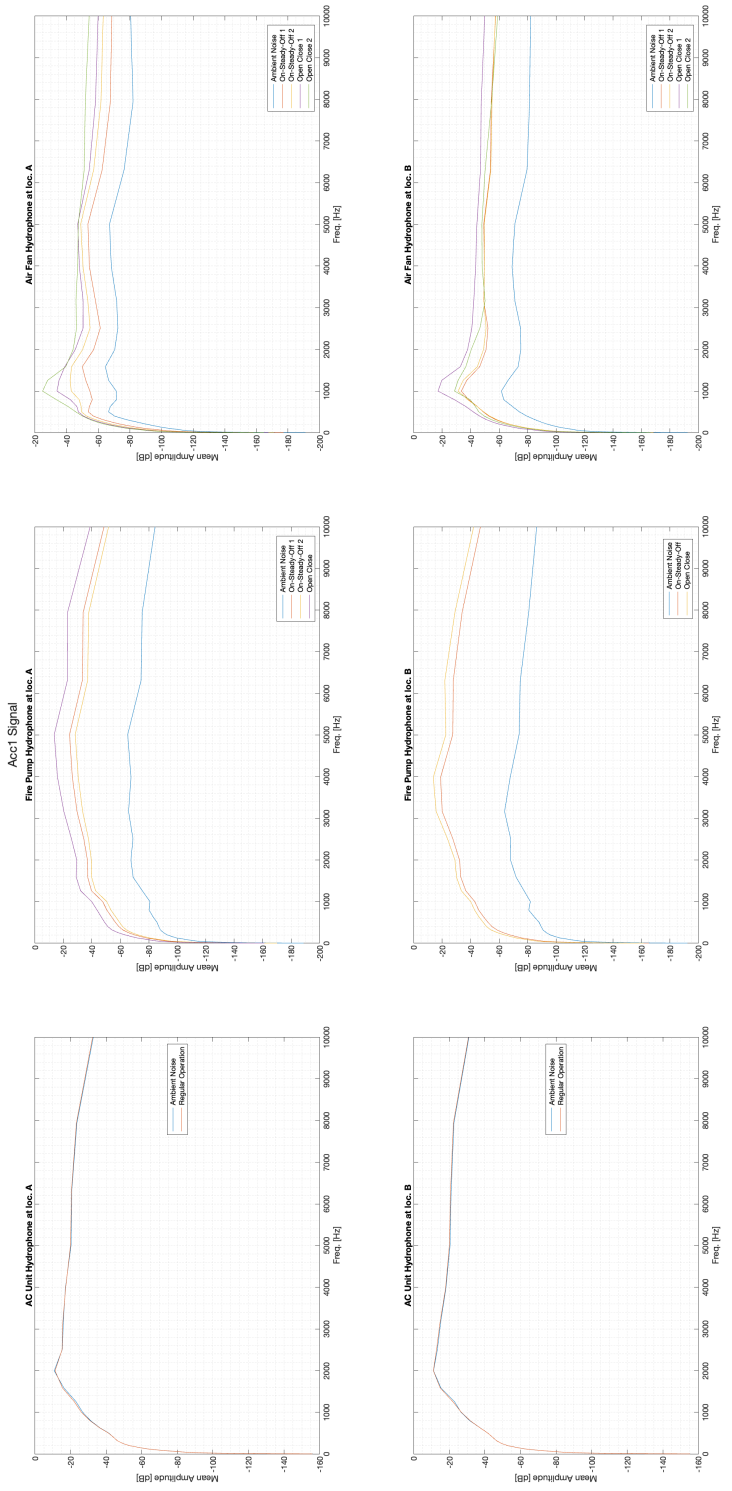

Figure 3-10: Time Averaged, Frequency Dependant Magnitude Levels, Acc. 1

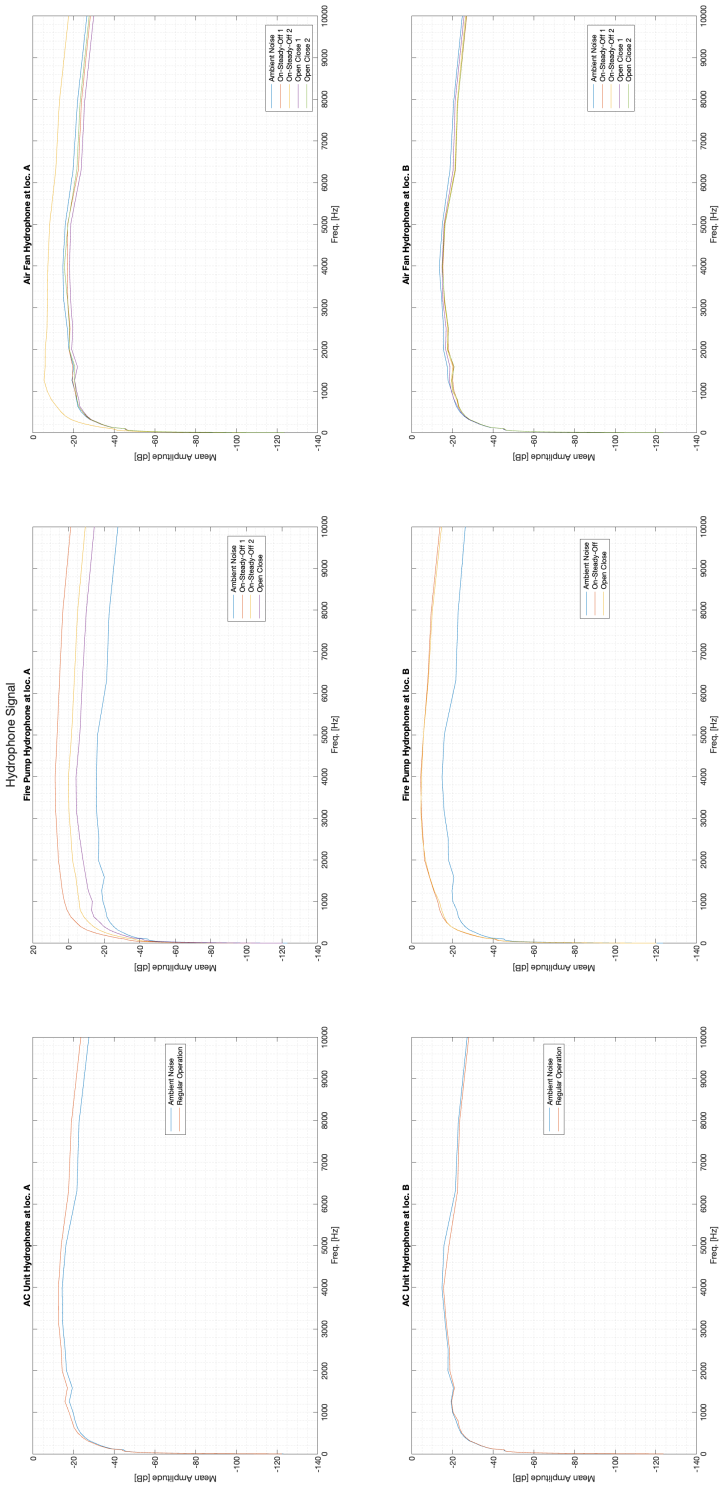

Figure 3-11: Time Averaged, Frequency Dependant Magnitude Levels, Hydrophone

The opposite trend is shown when analyzing the measurement from experiment 19. in this case, no significant magnitude changes are observed throughout the spectrum measured in accelerometer 1, maybe only around center frequencies of 631Hz, 792Hz, and 1kHz (Figure 3-15. Accelerometer 3 (Figure 3-16) shows to track the behavior observed in accelerometer 1 for a center frequency of 1kHz. However, the trend is visible throughout the range, as seen in the spectrogram of the hydrophone signal in Figure 3-17.

Moreover, another interesting phenomenon appears when analyzing experiment 16. The signal obtained from accelerometer 1 (Figure 3-18) shows apparent periodic behavior throughout the spectrum when manually blocking and unblocking the intake of the fan. This periodic behavior, in different magnitudes, is also observed in the measurements of the hull's vibration, collected by accelerometer 3 (Figure 3-19). However, analyzing the hydrophone signal (Figure 3-20) does not point out any visible trend for the human eye.

Concluding, some behaviors and trends are visible to the human eye using simple analysis and slicing of spectrograms. Nevertheless, correlations and behaviors that are not visible to the human eye might be obtained using computer analysis of the signals and their spectra, leading to the following sub-sections dealing with this issue.

Additional graphs, and results, appear in Appendix B.

3.2.3 Gain Estimation Using "tfestimate"

MATLAB's built-in function, "tfestimate," had demonstrated impressive results regarding the cabinet experiment, resulting in errors of less than 1%. The accelerometer signals from the "On-Steady-Off" experiments were used for the hydrophone's gain function evaluation, while the gain functions were tested using the "Open-Close" set of experiments. Similar to the process conducted in the cabinet experiment, the time-averaged estimation error for the entire spectrum was evaluated using the measured signal, as shown in Figure 3-21. The error levels show inferior performance, showing no suitable measurement prediction method.

The high noise levels might explain the high errors using this method that the

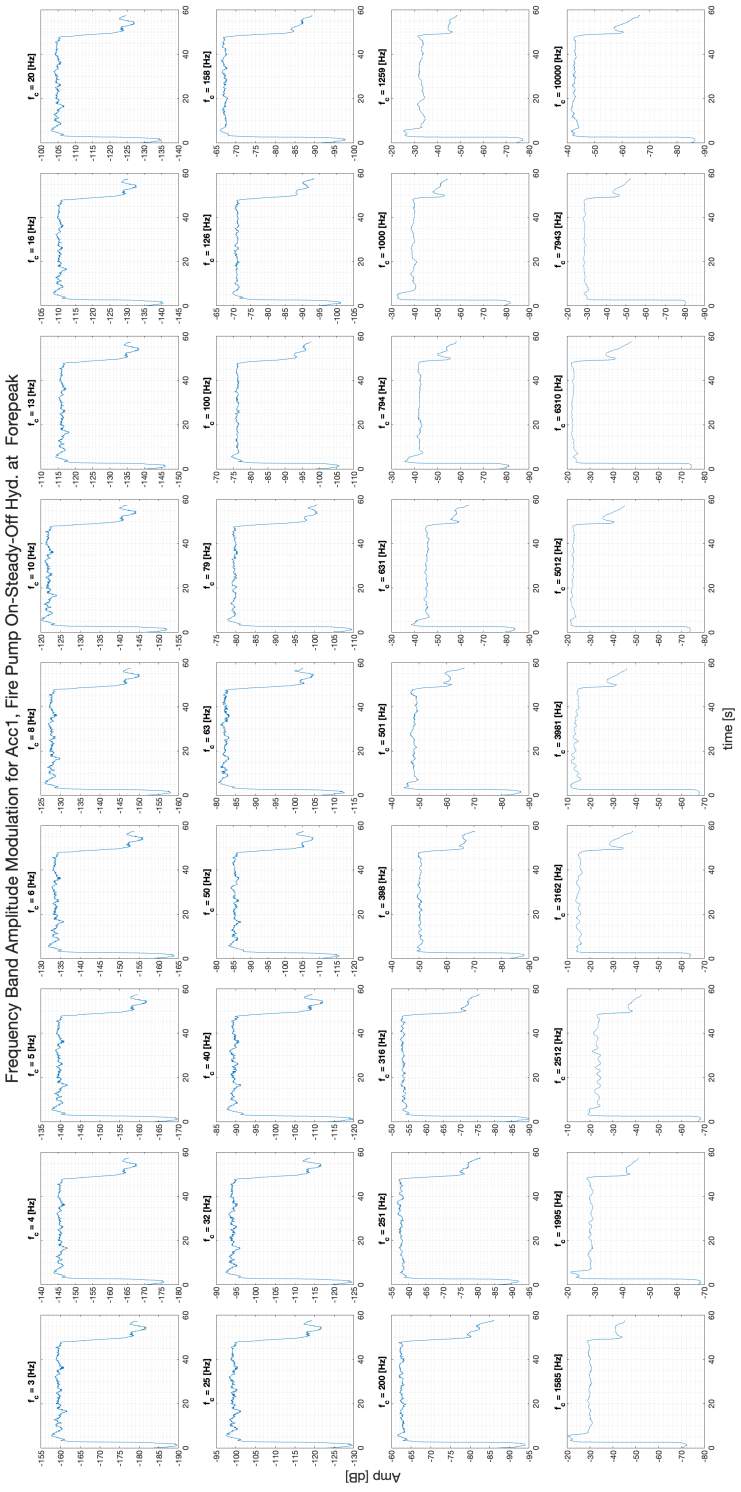

Figure 3-12: Frequency Band Analysis for Acc.1 Signal, Exp. No.18

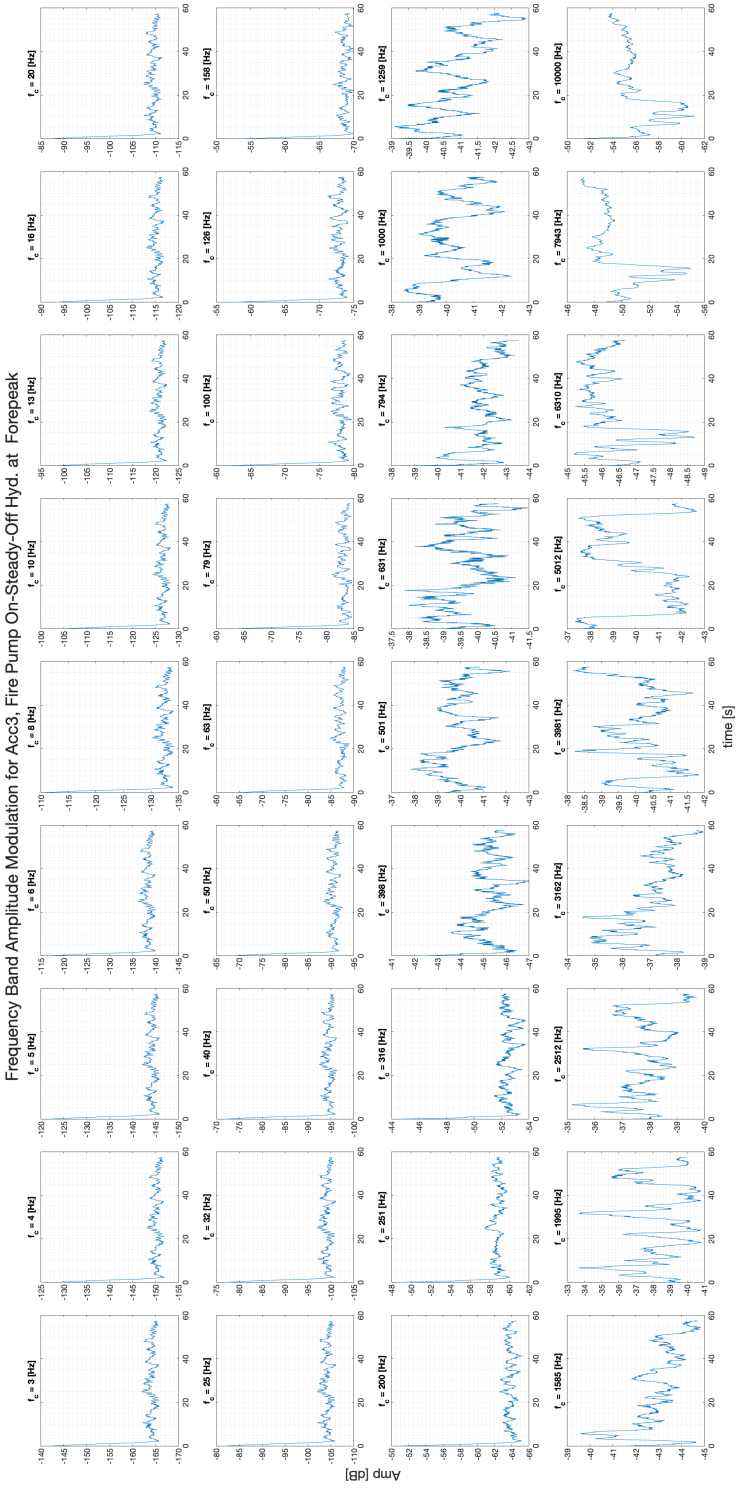

Figure 3-13: Frequency Band Analysis for Acc.3 Signal, Exp. No.18

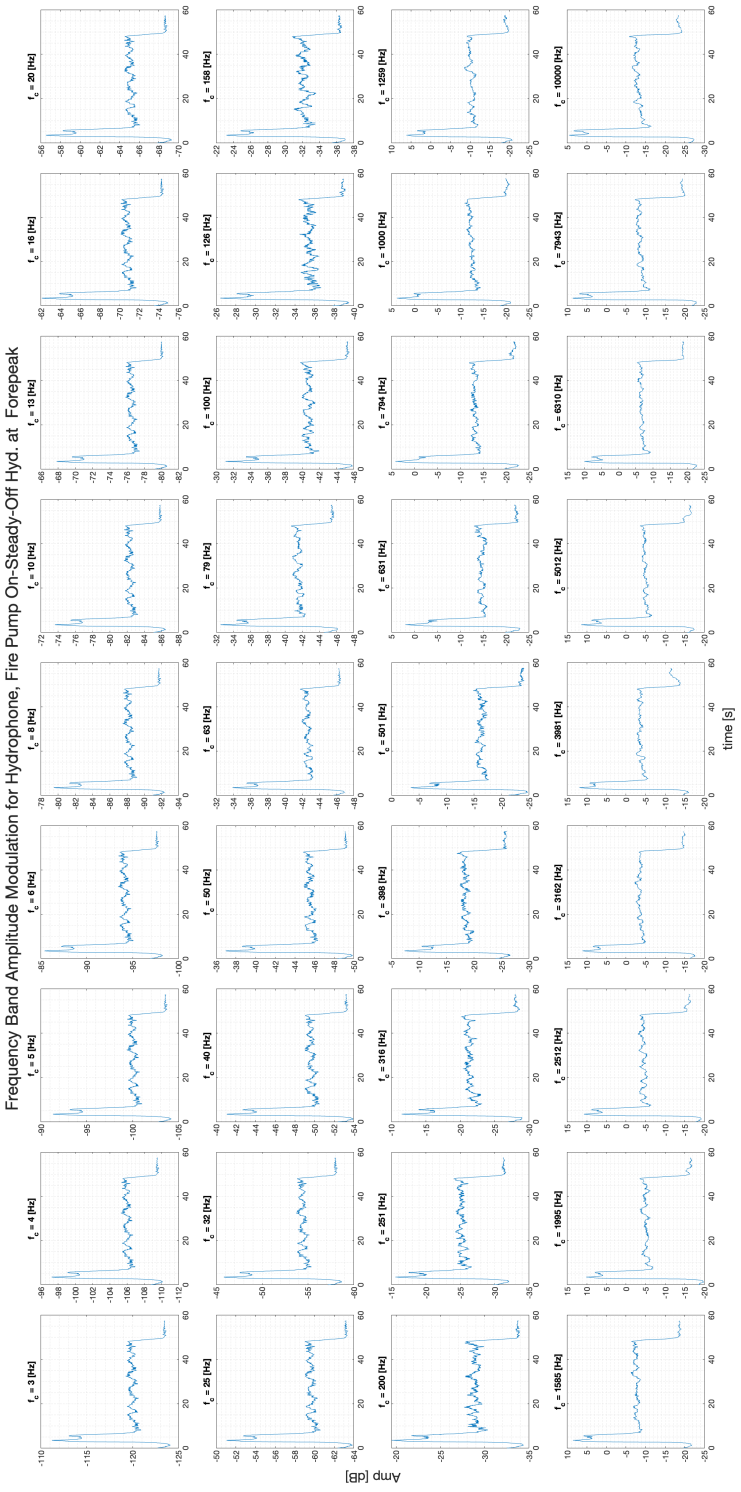

Figure 3-14: Frequency Band Analysis for Hydrophone Signal, Exp. No.18

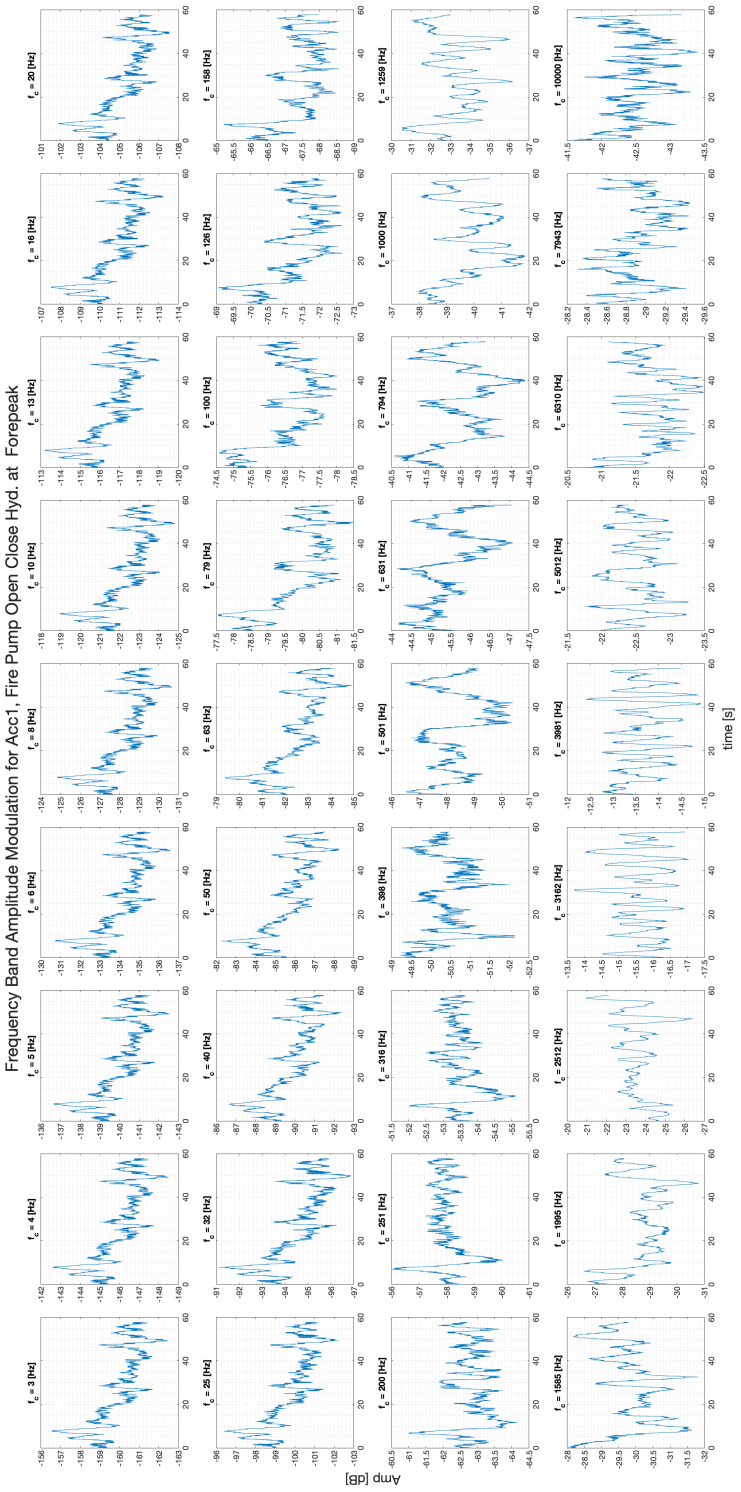

Figure 3-15: Frequency Band Analysis for Acc.1 Signal, Exp. No.19

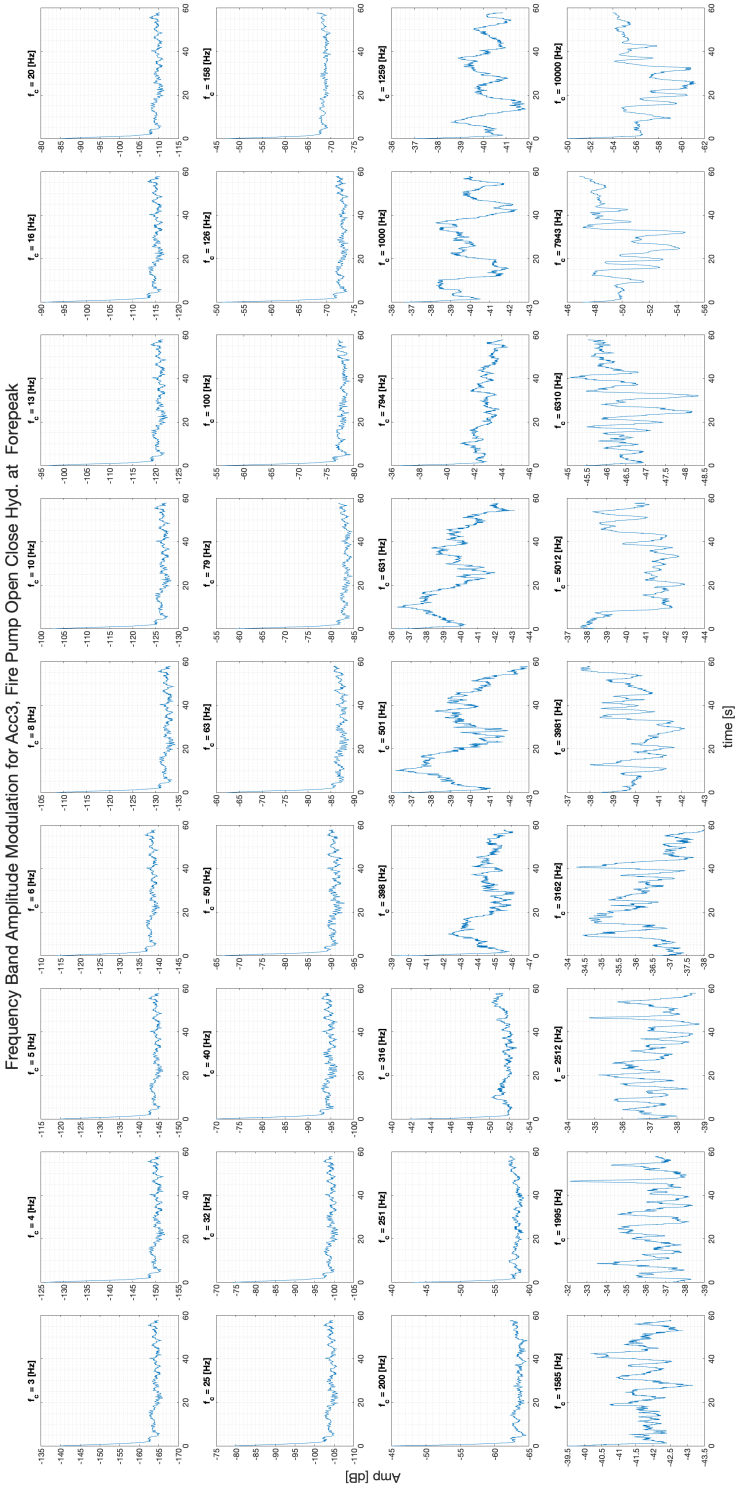

Figure 3-16: Frequency Band Analysis for Acc.3 Signal, Exp. No.19

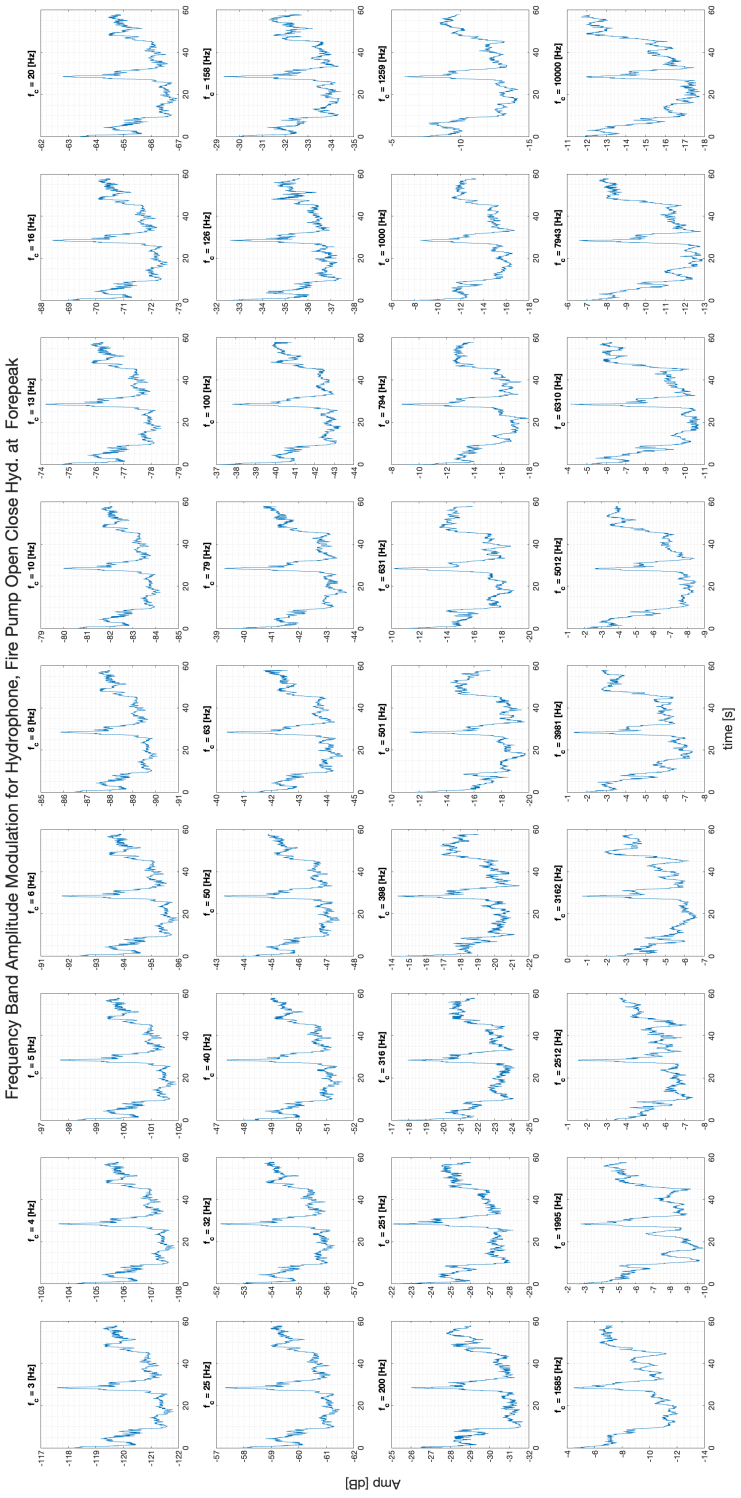

Figure 3-17: Frequency Band Analysis for Hydrophone Signal, Exp. No.19

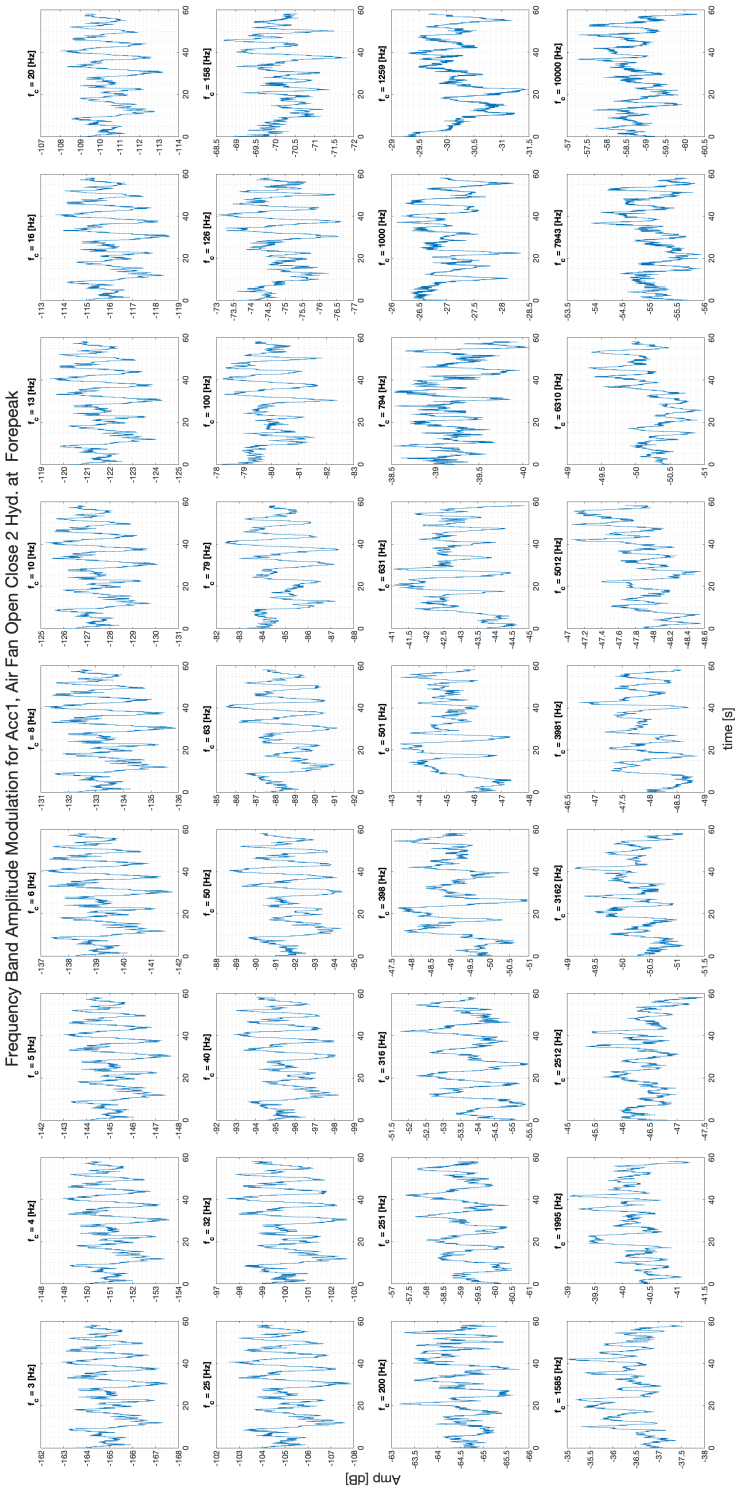

Figure 3-18: Frequency Band Analysis for Acc.1 Signal, Exp. No.16

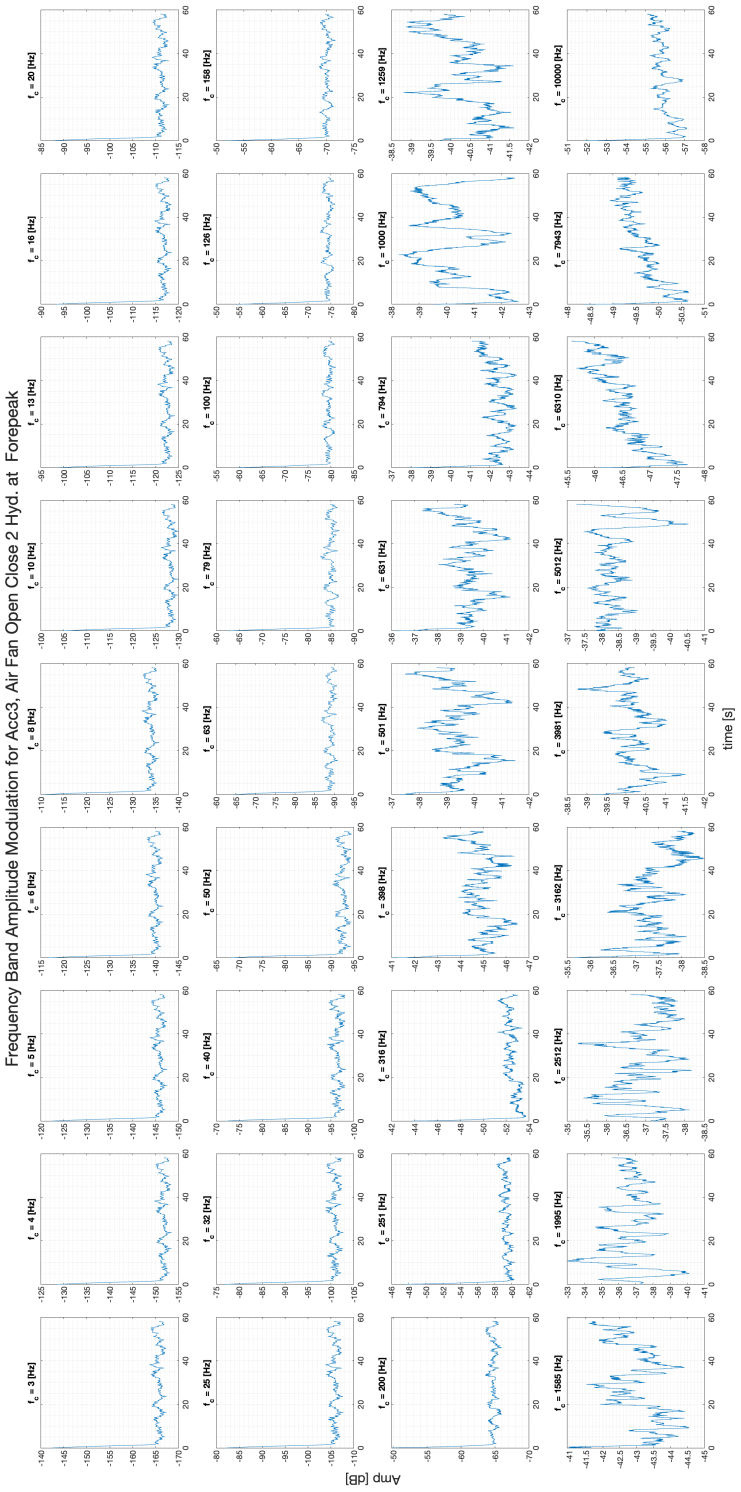

Figure 3-19: Frequency Band Analysis for Acc.3 Signal, Exp. No.16

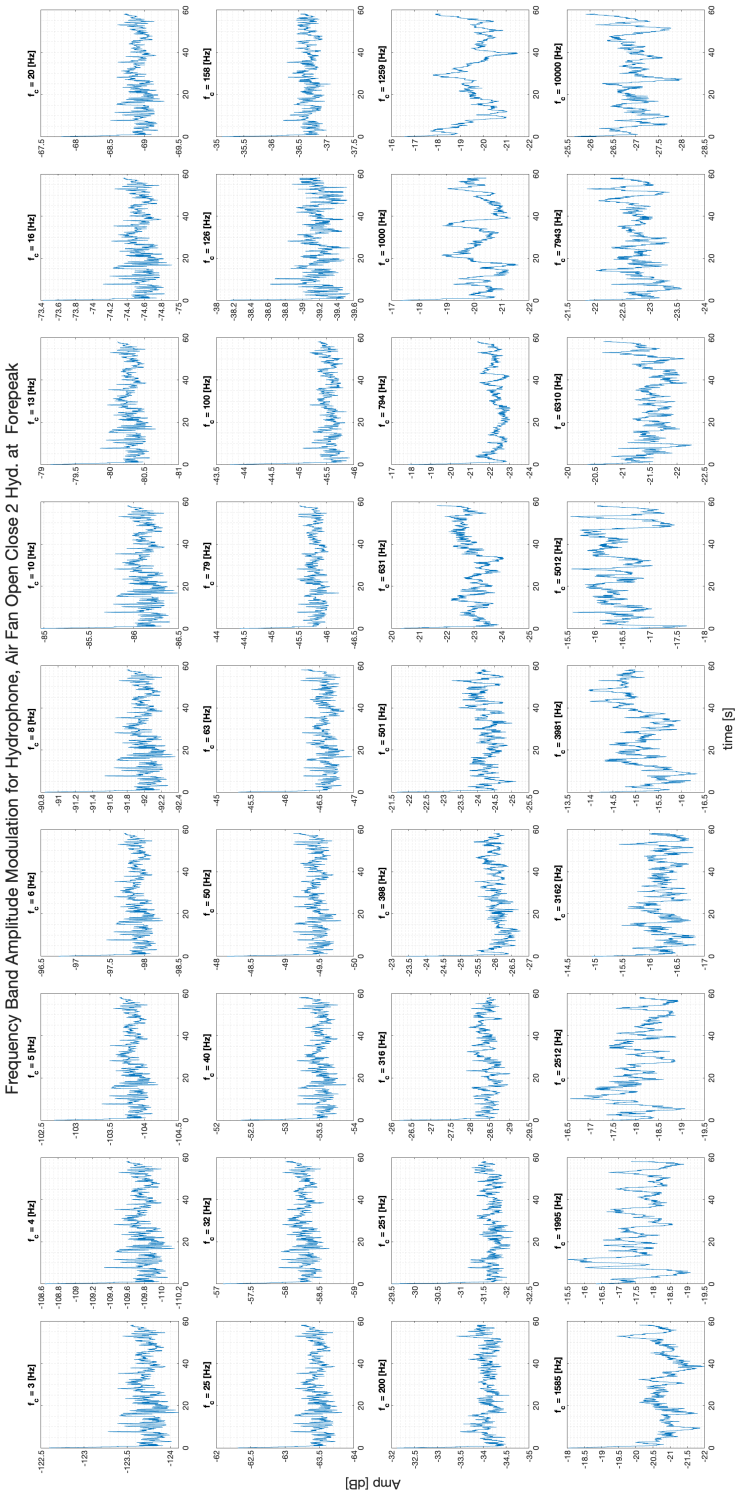

Figure 3-20: Frequency Band Analysis for Hydrophone Signal, Exp. No.16

"tfestimate" algorithm cannot account for nor filter easily. As the spectrograms showed, sometimes the patterns do not correlate, or the source of the noise does not directly connect to the vibration on the machine itself but through another mechanism like flow noise.

Averaging through the frequency ranges to the 1/3 octave domain, Figure 3-22 shows better performance in the error levels. Nevertheless, using the 1/3 Octave domain shows the general advantage of using the plate vibration measurement directly, with a general average error of around 10-15%.

3.2.4 Gain Estimation Using Recurrent Neural Network

Although an unorthodox way of estimation, Recurrent Neural Networks (RNNs) might provide a better way to estimate the gain function due to its nature. Such networks include some amount of past information for better accuracy and are used in various ways such as speech recognition [5], visual tracking of objects [12], and time series prediction [14]. Therefore, using a machine-learning process, one could theoretically build a prediction model for the radiated noise using the machine-related vibration.

Using MATLAB, a simple RNN was constructed as illustrated in Figure 3-23. The input and output layers have 36 nodes each, representing the average magnitude at each time interval. Additionally, two hidden layers with a delay of two previous time segments were added, where the first hidden layer had 24 nodes and the second had 32 nodes. Each layer was activated linearly, as shown in the illustration.

Similarly, the training and validation data were taken from the "On-Steady-Off" experiment and the "Ambient Noise" experiments. The training function used was the MATLAB generic "Levenberg-Marquardt" method [9]. Later on, the trained network was used to predict the output for the "Open-Close" experiments compared to the actual measured hydrophone signal.

An example for the prediction output using accelerometer 1 is shown in Figure 3-24. It shows some agreement in levels around the lower frequencies, while the levels' deviation grew in the higher frequencies. Moreover, there is no specific trend to

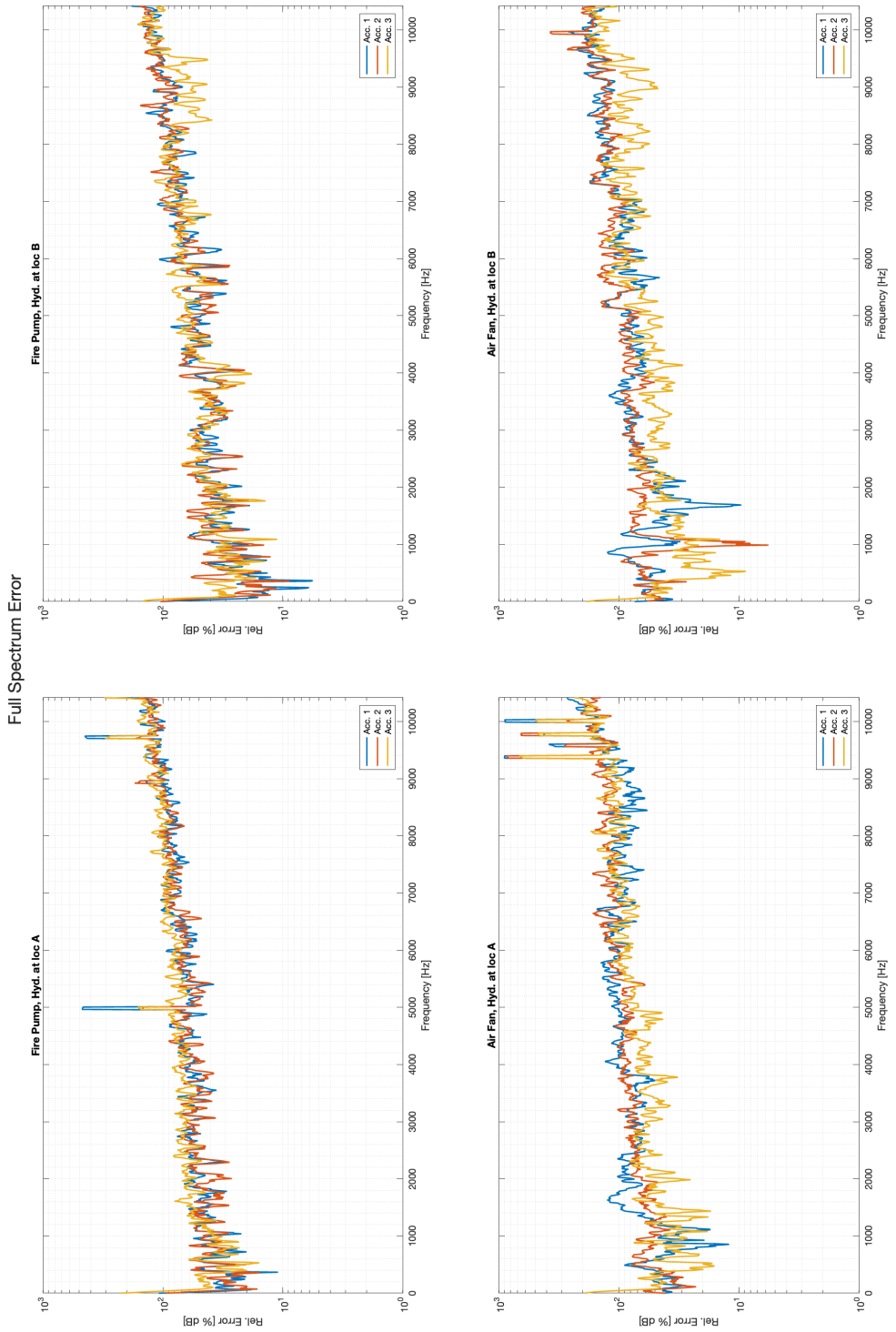

Figure 3-21: Prediction Error using "tfestimate" - Full Spectrum

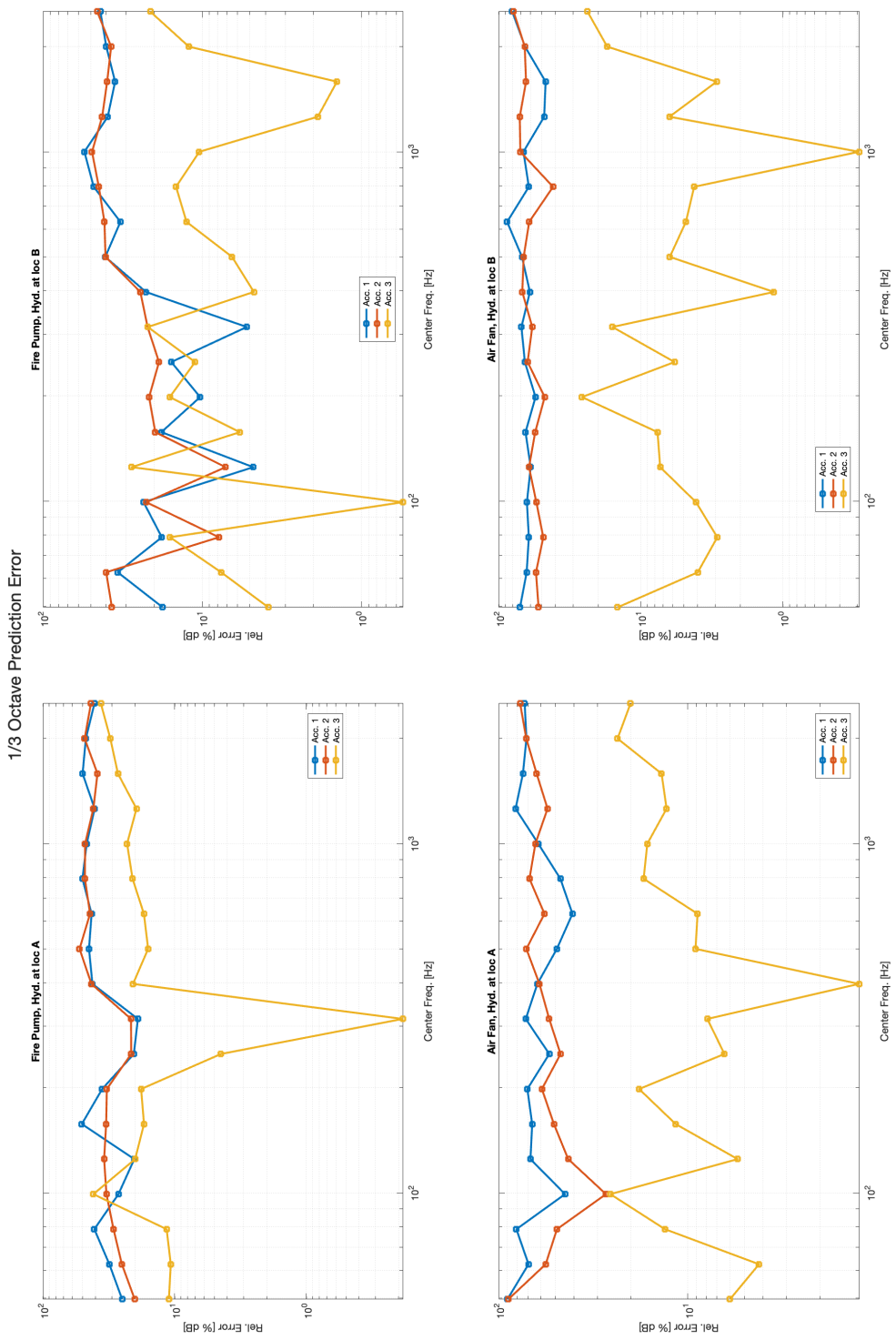

Figure 3-22: Prediction Error using "tfestimate" - 1/3 Octave

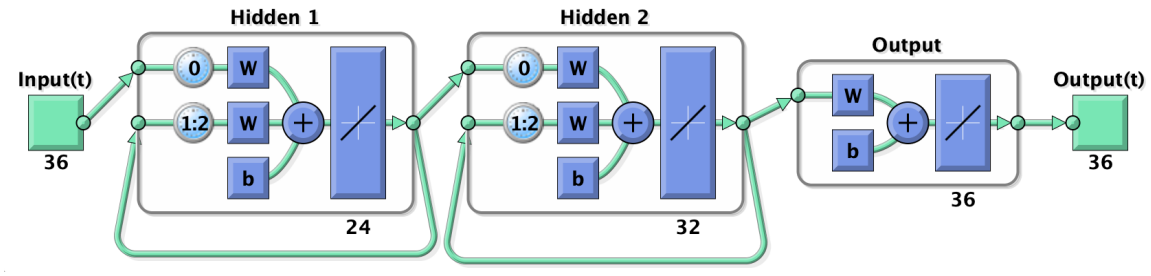

Figure 3-23: Simple RNN for Gain Prediction

whether the network underestimates or overestimates the noise level. The relative estimation error, in both dB levels (blue) and percentage (red), are shown in Figures 3-25, 3-26, 3-27, and 3-28.

Compared to the "tfestimate" method, the general performance is decent, especially in lower frequency bands. Moreover, as more data is collected, the model improves accuracy, allowing lower error levels. Other system architectures and training functions were examined, with no significant improvement in error or no learning algorithm convergence.

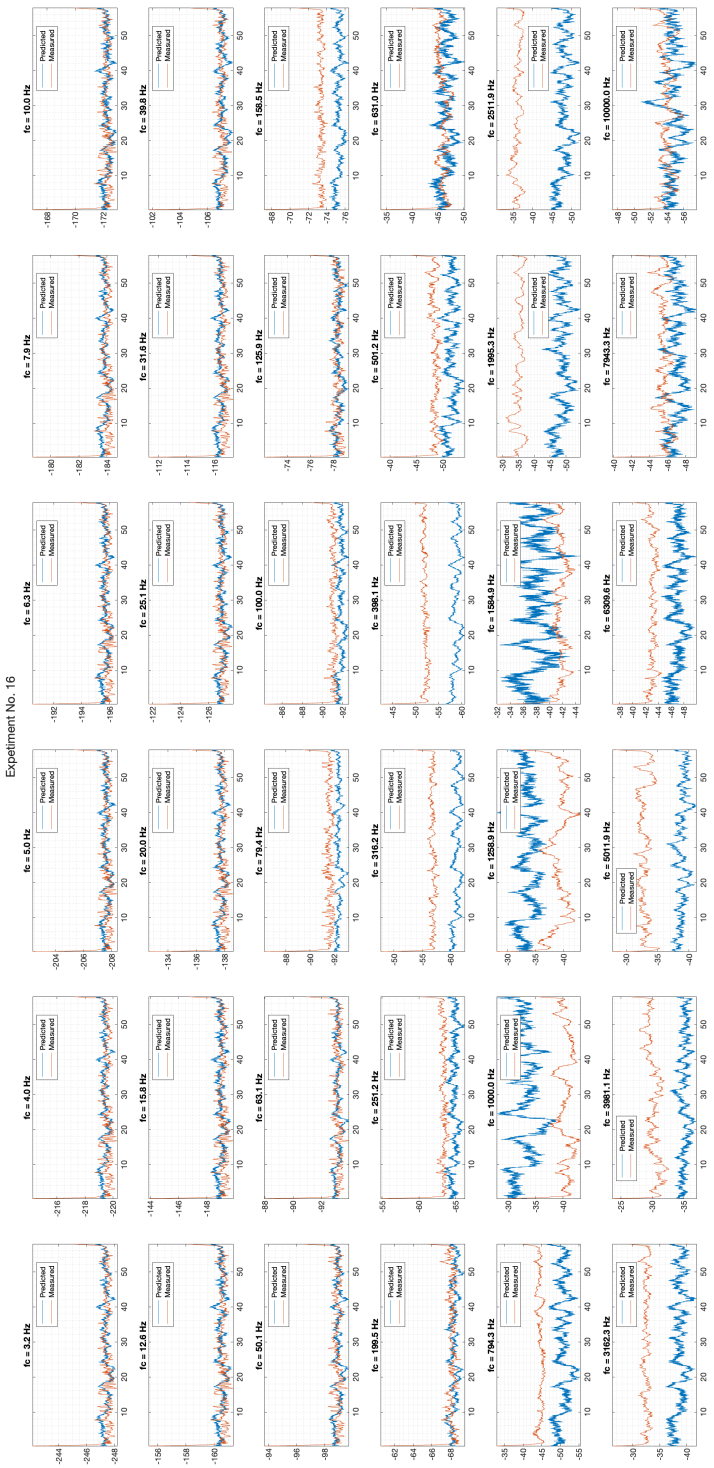

Figure 3-24: Acc.1 Frequency-Band, Time Series Prediction using RNN, Exp.16

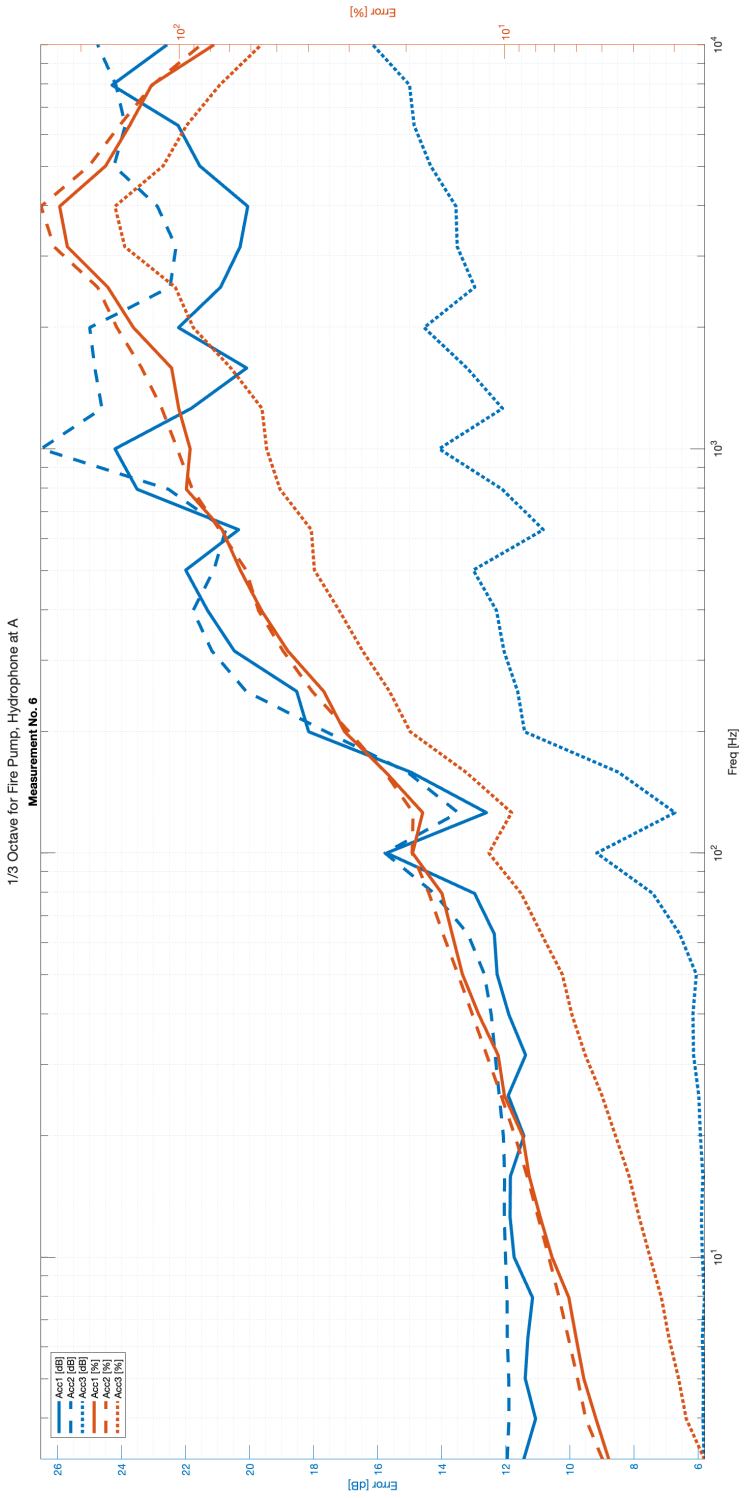

Figure 3-25: RNN Prediction Performance for Fire Pump, Hydrophone at "A"

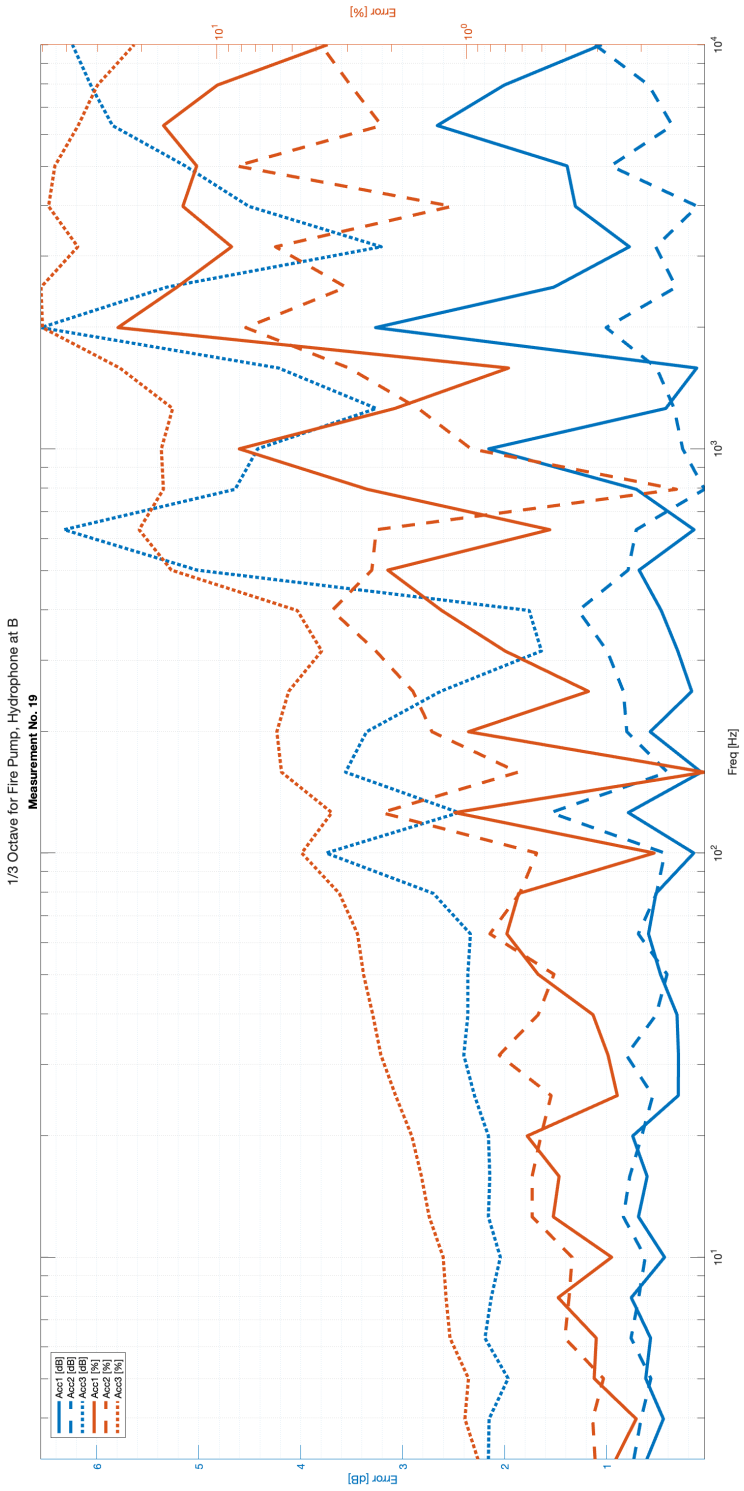

Figure 3-26: RNN Prediction Performance for Fire Pump, Hydrophone at "B"

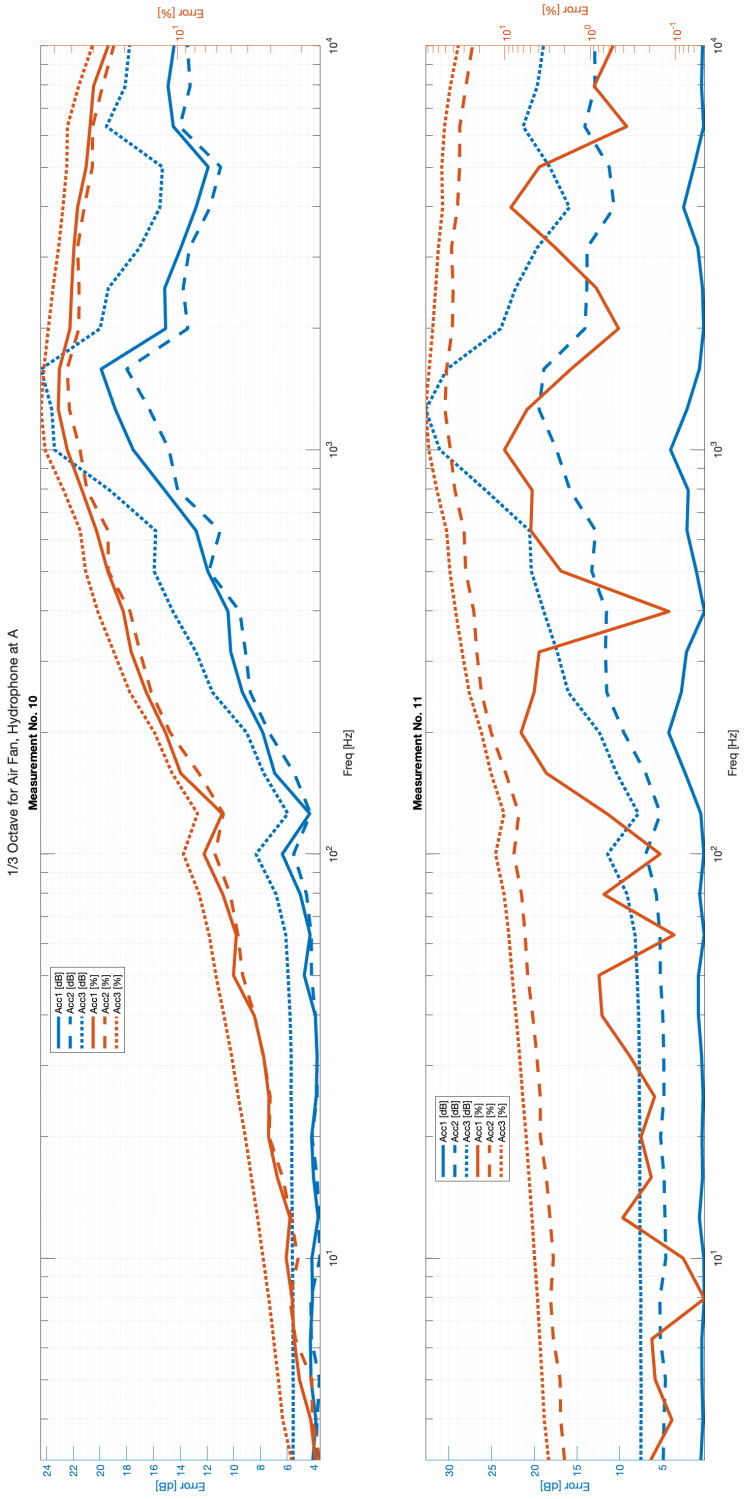

Figure 3-27: RNN Prediction Performance for Air Fan, Hydrophone at "A"

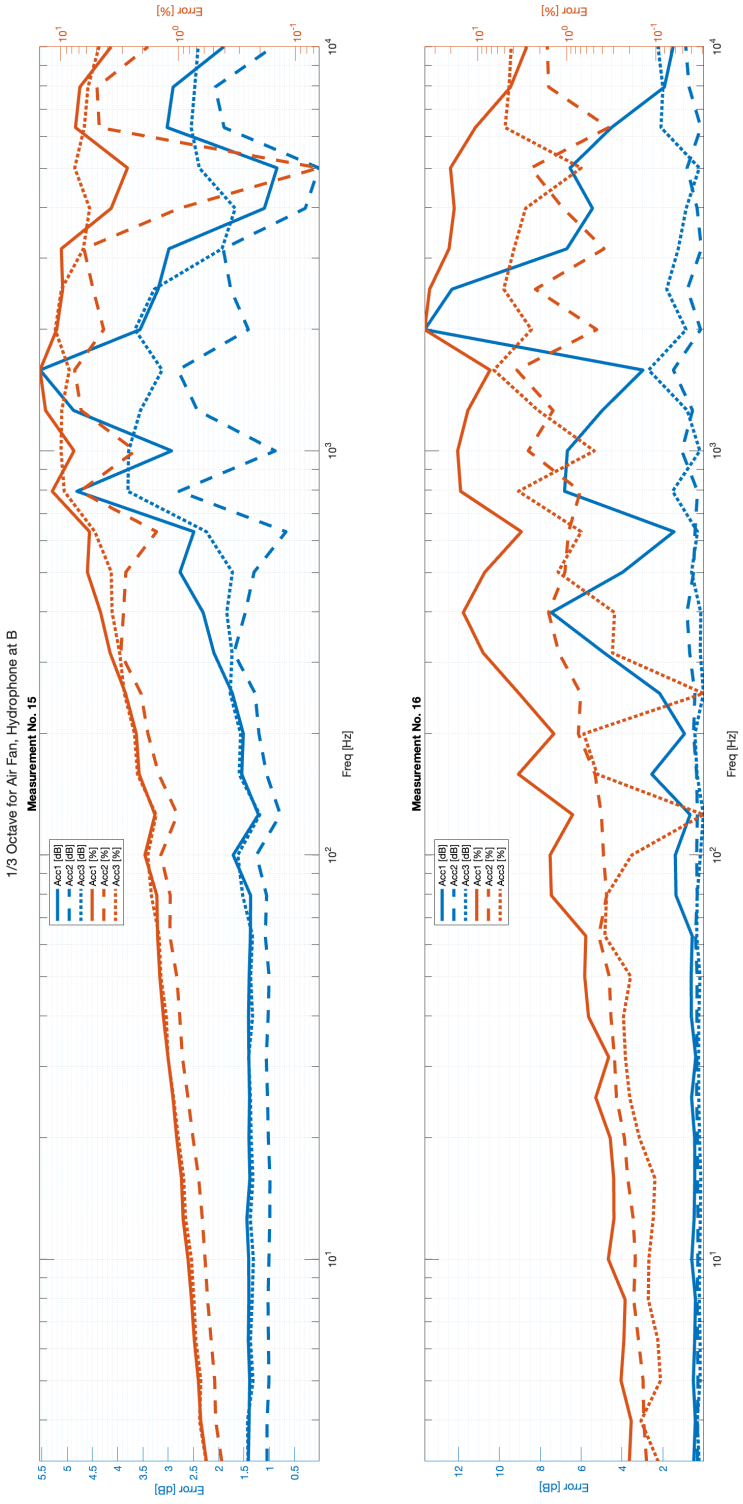

Figure 3-28: RNN Prediction Performance for Air Fan, Hydrophone at "B"

Chapter 4

Conclusion and Future Research

This work aimed to connect acoustic monitoring discipline and the predictive maintenance world by constructing a frequency-gain model between vibrations on shipboard-mounted machinery and the acoustic signature of the ship. The literature survey yielded several methods to construct a frequency-gain model, where some dealt with the estimation empirically, and some dealt with it by direct calculation. Two main methods were chosen - Statistical Energy Analysis (SEA) and Finite Element Analysis (FEA).

Statistical Energy Analysis is a method that bundles vibrations to frequency dependant "bins of energy" that transfers between sub-systems according to their energetic state. Similar to a thermal model, heat (vibrational energy) can transfer only from high-temperature (high-energy) bodies to low-temperature (low-energy) bodies. Therefore, each transfer mechanism depends on the boundary line and interface between the bodies.

On the other hand, Finite Element Analysis directly computes the modes and their related frequency. This way, instead of bundling energetic states, each state is solved particularly, and the results are given with high resolution of detail. Nevertheless, this method requires strong computation power and resources.

In order to validate these theoretical models on a simple system, a simple metal cabinet was modeled and experimented with. At first, both methods yielded different predictions to the cabinet's behavior for excitation and could not agree both

on vibration levels and trends. Comparing both methods to the experiment showed complete disagreement: both with each other and not conforming with the experimental results. Moreover, the frequency-gain model constructed using the experimental method could predict, with very little error, other experimental results that were not involved in the construction of the model.

Although not undoubtedly overruled, both prediction methods (SEA and FEA) demonstrated modeling sensitivity and complexity that could not help the research's cause to build a frequency-gain model for a more convoluted system like a ship. However, as mentioned, the experimental construction approach yielded a good result with the metal cabinet. Thus, this approach was adopted for the experimental process on the test ship.

Despite ambient noise levels that prevented the experiment from being fully controlled, the vibro-acoustic set of experiments on the test ship yielded exciting results. In some cases, the hydrophone could easily detect vibration patterns that appeared on the ship. In some cases, noise that was readily detected in the hydrophone was not seen in the accelerometers. Additionally, analyzing the vibro-acoustic data using the conventional methods resulted in high error levels, reaching up to about 1000% error. However, using a simple Recurrent Neural Network (RNN) had made the error levels manageable.

As far as the scope of this research goes, experimental methods proved better accuracy and efficiency in building a frequency-gain model for a convoluted system. Moreover, some predictive models even showed disagreement with the experimental results, strengthening the claim that one must not rely solely on predictive models. RNNs showed excellent noise filtering performance and could detect changes not seen in the human eye while analyzing spectrograms. Therefore it is recommended to try and deepen the research in the use of RNNs for better frequency-gain model construction.

Appendix A

Cabinet Drawings and Modeling Details

A.1 Cabinet Technical Drawings

This section contains:

1. Bill of Materials - Table A.1
2. Assembly Drawing - Figure A-1
3. Parts Drawings - Figure A-2

Item No.	Description	Qty.
1	Cover Plates - Top & Bottom	2
2	Front U-Beams - Top & Bottom	2
3	Front Vertical Beams - Left & Right	2
4	Side Plates - Left & Right	2
5	Back Supporting Plates - Top & Bottom	2
6	Back Vertical Beams - Left & Right	2
7	Back Center Plate	1
8	Back Side-Plates - Left & Right	2

Table A.1: Bill of Materials for Assembly - Top Level

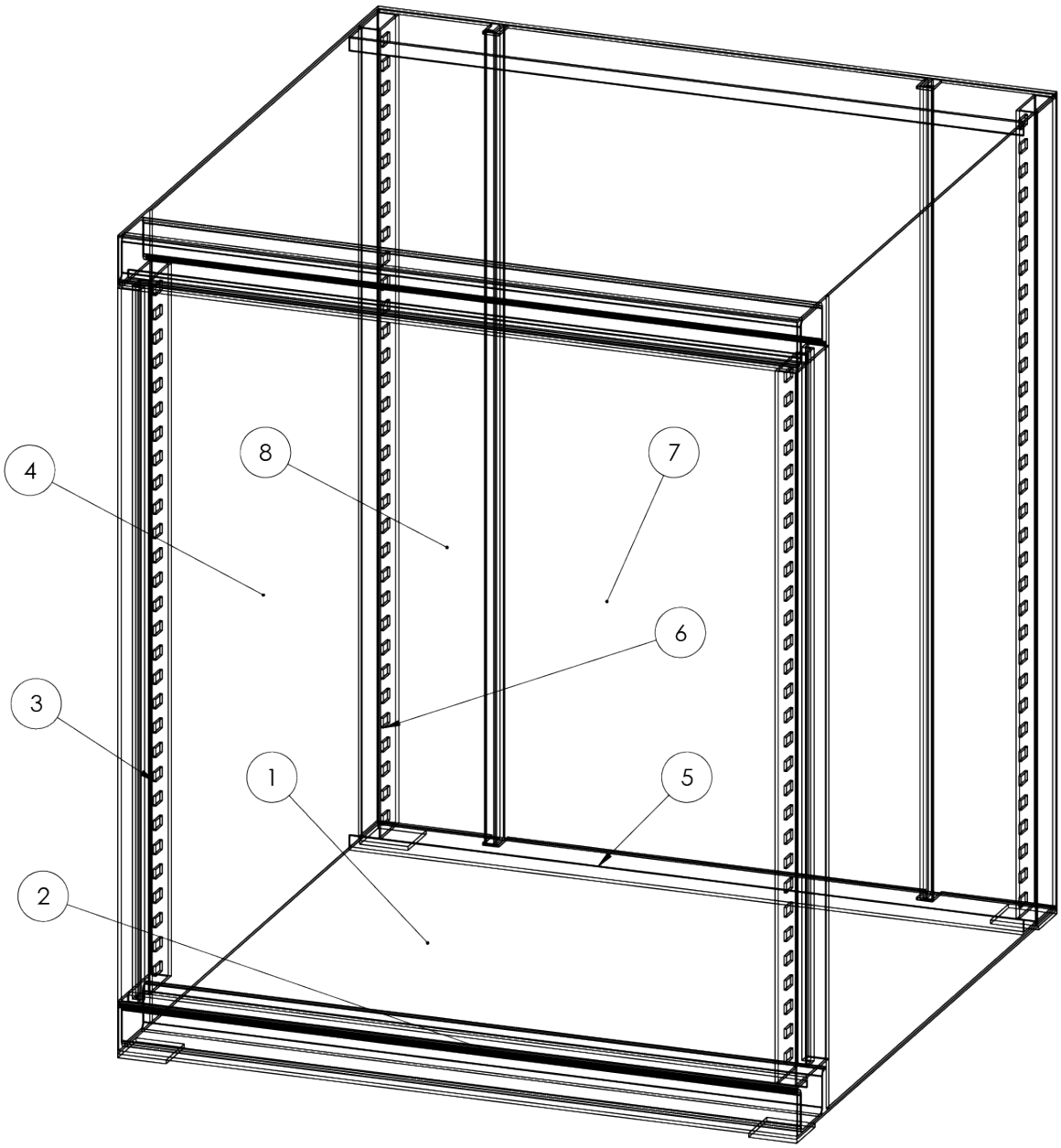

Figure A-1: Assembly Illustration of the Cabinet

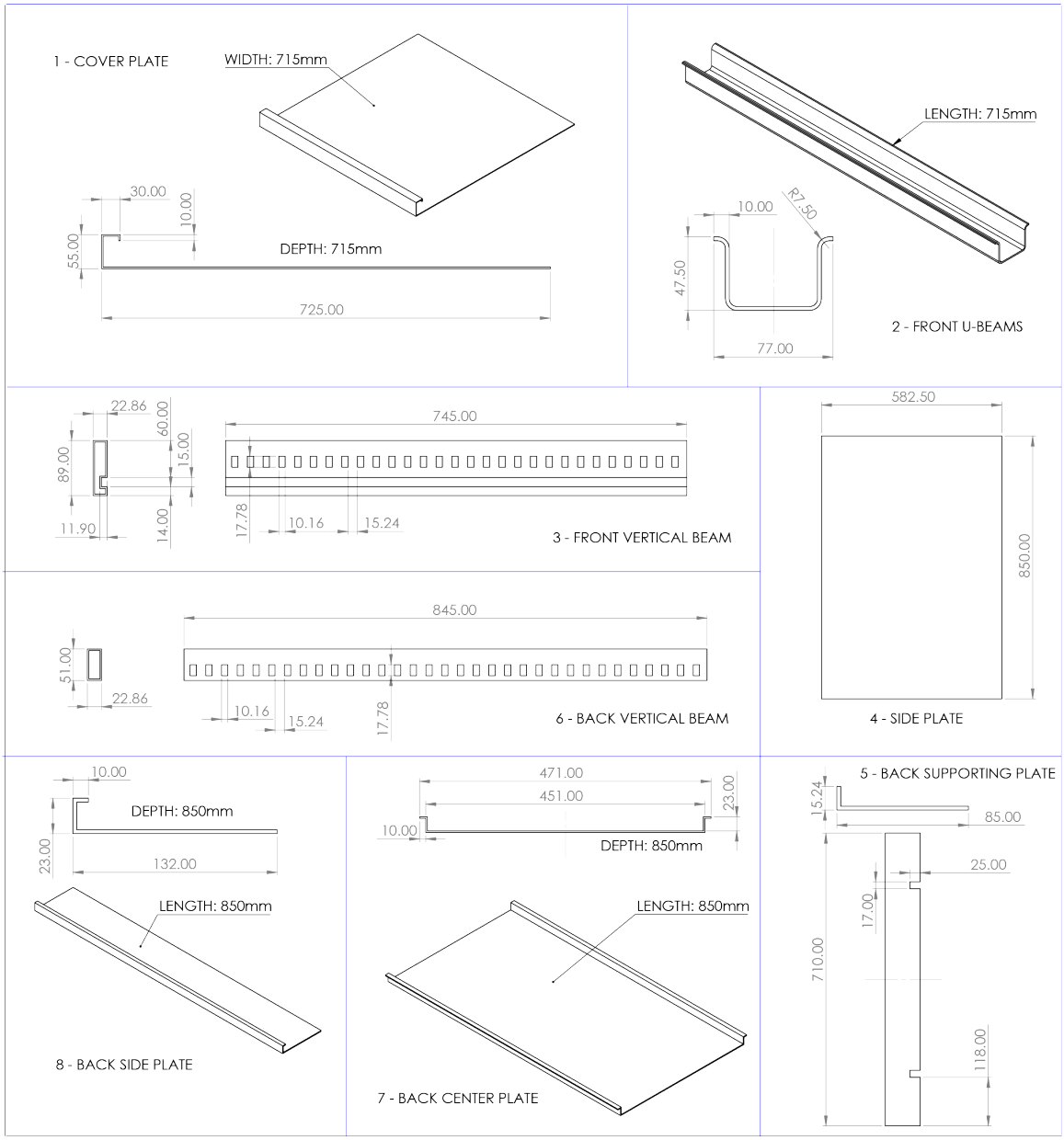

ALL PLATE THICKNESS ARE 2.5MM UNLESS SPECIFIED

Figure A-2: Cabinet Part-Specific Drawings

A.2 Cabinet Sub-Division for SEA

This section contains:

1. SEA Plate Table - Tables A.2 and A.3 with the following fields:
   (a) Plate Number
   (b) Plate Name (Abbreviated)
   (c) Plate Width $[mm]$
   (d) Plate Length $[mm]$
   (e) Plate Area $[mm^2]$
   (f) Plate Thickness $[mm]$
2. SEA Cavity and Connecting Plate Table - Table A.4 with the following fields:
   (a) Air Cavity Number (5 total)
   (b) Air Cavity Name
   (c) Air Cavity Depth $[m]$
   (d) Air Cavity Width $[m]$
   (e) Air Cavity Height $[mm^2]$
   (f) Connecting Plate No.
   (g) Area of Interaction $[m^2]$
3. SEA Plate-Plate Connections - Tables A.5, A.6 and A.7 with the following fields:
   (a) Connection No.
   (b) Connecting Plate "A" No.
   (c) Connecting Plate "B" No.
   (d) Connection Angle $[^\circ]$
   (e) Connection Length $[m]$

No.	Name	Wid. [mm]	Len. [mm]	Area [mm^2]	t [mm]
1	Bottom Plate - B0	715	725	518375	2.5
2	Bottom Plate - B1	715	55	39325	2.5
3	Bottom Plate - B2	715	30	21450	2.5
4	Bottom Plate - B3	715	10	7150	2.5
5	Top Plate - B0	715	725	518375	2.5
6	Top Plate - B1	715	55	39325	2.5
7	Top Plate - B2	715	30	21450	2.5
8	Top Plate - B3	715	10	7150	2.5
9	Bot. Front Beam - B0	715	10	7150	2.5
10	Bot. Front Beam - B1	715	50	35750	2.5
11	Bot. Front Beam - B2	715	62	44330	2.5
12	Bot. Front Beam - B3	715	50	35750	2.5
13	Bot. Front Beam - B4	715	10	7150	2.5
14	Top Front Beam - B0	715	10	7150	2.5
15	Top Front Beam - B1	715	50	35750	2.5
16	Top Front Beam - B2	715	62	44330	2.5
17	Top Front Beam - B3	715	50	35750	2.5
18	Top Front Beam - B4	715	10	7150	2.5
19	Right Hand Plate	850	582	494700	2.5
20	Left Hand Plate	850	582	494700	2.5
21	Back RH Plate - B0	850	132	112200	2.5
22	Back RH Plate - B1	850	23	19550	2.5
23	Back RH Plate - B2	850	10	8500	2.5
24	Back LH Plate - B0	850	132	112200	2.5
25	Back LH Plate - B1	850	23	19550	2.5
26	Back LH Plate - B2	850	10	8500	2.5

Table A.2: Modeled Sub-Plates 1-26

No.	Name	Wid. [mm]	Len. [mm]	Area [mm^2]	t [mm]
27	Back Mid. Plate - B0	850	13	11050	2.5
28	Back Mid. Plate - B1	850	23	19550	2.5
29	Back Mid. Plate - B2	850	450	382500	2.5
30	Back Mid. Plate - B3	850	23	19550	2.5
31	Back Mid. Plate - B4	850	13	11050	2.5
32	Back Bot. Plate - B0	710	85	59500	2.5
33	Back Bot. Plate - B1	710	15	10650	2.5
34	Back Top Plate - B0	710	85	59500	2.5
35	Back Top Plate - B1	710	15	10650	2.5
36	Fr. RH V-Beam - B0	745	23	17135	2.5
37	Fr. RH V-Beam - B1	745	89	66305	2.5
38	Fr. RH V-Beam - B2	745	23	17135	2.5
39	Fr. RH V-Beam - B3	745	109	81205	2.5
40	Fr. LH V-Beam - B0	745	23	17135	2.5
41	Fr. LH V-Beam - B1	745	89	66305	2.5
42	Fr. LH V-Beam - B2	745	23	17135	2.5
43	Fr. LH V-Beam - B3	745	109	81205	2.5
44	Back RH V-Beam - B0	845	23	19435	2.5
45	Back RH V-Beam - B1	845	51	43095	2.5
46	Back RH V-Beam - B2	845	23	19435	2.5
47	Back RH V-Beam - B3	845	51	43095	2.5
48	Back LH V-Beam - B0	845	23	19435	2.5
49	Back LH V-Beam - B1	845	51	43095	2.5
50	Back LH V-Beam - B2	845	23	19435	2.5
51	Back LH V-Beam - B3	845	51	43095	2.5

Table A.3: Modeled Sub-Plates 27-51

Cav. No.	Name	D [m]	W[m]	H [m]	Conn. Plate	Area [m^2]
1	Main Cavity	0.715	0.725	0.850	1	0.518
1	Main Cavity	0.715	0.725	0.850	5	0.518
1	Main Cavity	0.715	0.725	0.850	10	0.036
1	Main Cavity	0.715	0.725	0.850	15	0.036
1	Main Cavity	0.715	0.725	0.850	19	0.495
1	Main Cavity	0.715	0.725	0.850	20	0.495
1	Main Cavity	0.715	0.725	0.850	21	0.112
1	Main Cavity	0.715	0.725	0.850	24	0.112
1	Main Cavity	0.715	0.725	0.850	29	0.383
1	Main Cavity	0.715	0.725	0.850	32	0.06
1	Main Cavity	0.715	0.725	0.850	34	0.06
1	Main Cavity	0.715	0.725	0.850	38	0.017
1	Main Cavity	0.715	0.725	0.850	39	0.081
1	Main Cavity	0.715	0.725	0.850	42	0.017
1	Main Cavity	0.715	0.725	0.850	43	0.081
1	Main Cavity	0.715	0.725	0.850	46	0.019
1	Main Cavity	0.715	0.725	0.850	47	0.043
1	Main Cavity	0.715	0.725	0.850	50	0.019
1	Main Cavity	0.715	0.725	0.850	51	0.043
2	Fr. RH V-Beam	0.090	0.025	0.745	36	0.017
2	Fr. RH V-Beam	0.090	0.025	0.745	37	0.066
2	Fr. RH V-Beam	0.090	0.025	0.745	38	0.017
2	Fr. RH V-Beam	0.090	0.025	0.745	39	0.081
3	Fr. LH V-Beam	0.090	0.025	0.745	40	0.017
3	Fr. LH V-Beam	0.090	0.025	0.745	41	0.066
3	Fr. LH V-Beam	0.090	0.025	0.745	42	0.017
3	Fr. LH V-Beam	0.090	0.025	0.745	43	0.081
4	Back RH V-Beam	0.050	0.023	0.845	44	0.019
4	Back RH V-Beam	0.050	0.023	0.845	45	0.043
4	Back RH V-Beam	0.050	0.023	0.845	46	0.019
4	Back RH V-Beam	0.050	0.023	0.845	47	0.043
5	Back LH V-Beam	0.050	0.023	0.845	48	0.019
5	Back LH V-Beam	0.050	0.023	0.845	49	0.043
5	Back LH V-Beam	0.050	0.023	0.845	50	0.019
5	Back LH V-Beam	0.050	0.023	0.845	51	0.043

Table A.4: Modeled Cavities and their Interaction Areas

No.	Plt. A	Plt. B	∠ [°]	L [m]		No.	Plt. A	Plt. B	∠ [°]	L [m]
1	1	2	90	0.715		31	1	47	90	0.051
2	1	10	90	0.715		32	1	48	90	0.023
3	1	11	180	0.715		33	1	49	90	0.051
4	1	12	90	0.715		34	1	50	90	0.023
5	1	19	90	0.582		35	1	51	90	0.051
6	1	20	90	0.582		36	2	3	90	0.715
7	1	21	90	0.132		37	2	13	90	0.715
8	1	22	90	0.023		38	2	36	180	0.055
9	1	23	90	0.010		39	2	37	90	0.055
10	1	24	90	0.132		40	2	40	180	0.055
11	1	25	90	0.023		41	2	41	90	0.055
12	1	26	90	0.010		42	3	4	90	0.715
13	1	27	90	0.013		43	3	13	180	0.715
14	1	28	90	0.023		44	3	37	90	0.030
15	1	29	90	0.450		45	3	41	90	0.030
16	1	30	90	0.023		46	4	37	90	0.010
17	1	31	90	0.013		47	4	41	90	0.010
18	1	32	90	0.085		48	5	6	90	0.715
19	1	33	90	0.015		49	5	15	90	0.715
20	1	36	90	0.023		50	5	16	180	0.715
21	1	37	90	0.089		51	5	17	90	0.715
22	1	38	90	0.023		52	5	19	90	0.582
23	1	39	90	0.109		53	5	20	90	0.582
24	1	40	90	0.023		54	5	21	90	0.132
25	1	41	90	0.089		55	5	22	90	0.023
26	1	42	90	0.023		56	5	23	90	0.010
27	1	43	90	0.109		57	5	24	90	0.132
28	1	44	90	0.023		58	5	25	90	0.023
29	1	45	90	0.051		59	5	26	90	0.010
30	1	46	90	0.023		60	5	27	90	0.013

Table A.5: Plate Connections 1 - 60

No.	Plt. A	Plt. B	∠ [°]	L [m]		No.	Plt. A	Plt. B	∠ [°]	L [m]
61	5	28	90	0.023		91	7	37	90	0.030
62	5	29	90	0.450		92	7	41	90	0.030
63	5	30	90	0.023		93	8	37	90	0.010
64	5	31	90	0.013		94	8	41	90	0.010
65	5	34	90	0.085		95	9	10	90	0.715
66	5	35	90	0.015		96	9	37	90	0.010
67	5	36	90	0.023		97	9	41	90	0.010
68	5	37	90	0.089		98	10	11	90	0.715
69	5	38	90	0.023		99	10	37	90	0.050
70	5	39	90	0.109		100	10	41	90	0.050
71	5	40	90	0.023		101	11	12	90	0.715
72	5	41	90	0.089		102	11	37	90	0.062
73	5	42	90	0.023		103	11	41	90	0.062
74	5	43	90	0.109		104	12	13	90	0.715
75	5	44	90	0.023		105	12	37	90	0.050
76	5	45	90	0.051		106	12	41	90	0.050
77	5	46	90	0.023		107	13	37	90	0.010
78	5	47	90	0.051		108	13	41	90	0.010
79	5	48	90	0.023		109	14	15	90	0.715
80	5	49	90	0.051		110	14	37	90	0.010
81	5	50	90	0.023		111	14	41	90	0.010
82	5	51	90	0.051		112	15	16	90	0.715
83	6	7	90	0.715		113	15	37	90	0.050
84	6	18	90	0.715		114	15	41	90	0.050
85	6	36	180	0.055		115	16	17	90	0.715
86	6	37	90	0.055		116	16	37	90	0.062
87	6	40	180	0.055		117	16	41	90	0.062
88	6	41	90	0.055		118	17	18	90	0.715
89	7	8	90	0.715		119	17	37	90	0.050
90	7	18	180	0.715		120	17	41	90	0.050

Table A.6: Plate Connections 61-120

No.	Plt. A	Plt. B	∠ [°]	L [m]		No.	Plt. A	Plt. B	∠ [°]	L [m]
121	18	37	90	0.010		151	25	30	180	0.850
122	18	41	90	0.010		152	26	31	180	0.850
123	19	32	90	0.085		153	27	28	90	0.850
124	19	33	90	0.015		154	28	29	90	0.850
125	19	34	90	0.085		155	29	30	90	0.850
126	19	35	90	0.015		156	29	32	90	0.710
127	19	38	90	0.745		157	29	34	90	0.710
128	19	39	180	0.745		158	30	31	90	0.850
129	19	44	90	0.745		159	32	33	90	0.710
130	19	45	180	0.745		160	34	35	90	0.710
131	20	32	90	0.085		161	36	37	90	0.745
132	20	33	90	0.015		162	36	39	90	0.745
133	20	34	90	0.085		163	37	38	90	0.745
134	20	35	90	0.015		164	38	39	90	0.745
135	20	42	90	0.745		165	40	41	90	0.745
136	20	43	180	0.745		166	40	43	90	0.745
137	20	48	90	0.745		167	41	42	90	0.745
138	20	49	180	0.745		168	42	43	90	0.745
139	21	22	90	0.850		169	44	45	90	0.845
140	21	29	180	0.850		170	44	47	90	0.845
141	21	46	180	0.850		171	45	46	90	0.845
142	21	47	90	0.850		172	46	47	90	0.845
143	22	23	90	0.850		173	48	49	90	0.845
144	22	28	180	0.850		174	48	51	90	0.845
145	23	27	180	0.850		175	49	50	90	0.845
146	24	25	90	0.850		176	50	51	90	0.845
147	24	29	180	0.850						
148	24	50	180	0.850						
149	24	51	90	0.850						
150	25	26	90	0.850						

Table A.7: Plate Connections 121-176

Appendix B

Test Ship - Technical Data and Results

Figure B-1: C57 Hydrophone Picture

C57 hydrophone specifications		
	C57 / C57X	**C57RS / C57XRS**
Linear Frequency Range (±3dB) [kHz]	0.015 to 45	0.015 to 50 & 124 to 250+
Usable Frequency Range (+3/-12dB) [kHz]	0.008 to 100	0.008 to 77 & 96 to 250+
Transducer Sensitivity* [dB, re 1V/µPa]	-187	-200
Preamplifier Gain [dB]	20 / 33	20 / 33
Effective Sensitivity* [dB, re 1V/µPa]	-167 / -154	-180 / -167
SPL Equiv. Self Noise at 1kHz [dB, re 1µPa/√Hz]	46 (*Sea State Zero*)	61
Power Requirement [Vdc]	5 to 32	5 to 32
RMS Overload Acoustic Pressure [dB, re 1µPa]	171 to 188 / 158 to 175	184 to 201 / 171 to 188
Maximum Operating Depth [m]	370	920
Operating Temperature Range [°C]	-40 to 60	-40 to 60
Output Impedance [Ω]	10	10
Dimensions [mm]	116**L** x 25**dia.**	116**L** x 25**dia.**
Integral Connector * **	Subconn MCBH3MSS	Subconn MCBH3MSS

Figure B-2: C57 Hydrophone Technical Data

13 – Specifications

Rating

■ **Recording media**

microSD card (64 MB–2 GB)
microSDHC card (4 GB–32 GB)
microSDXC card (48 GB–128 GB)

■ **Recording/playback formats**

BWF: 44.1k/48k/96kHz, 16/24 bit
WAV: 44.1k/48k/96kHz, 16/24 bit
MP3: 44.1k/48 kHz, 32k/64k/96k/128k/192k/256k/320kbps

■ **Number of channels**

2 channels (stereo)

Input/output ratings

Analog audio input and output ratings

■ **MIC/EXT IN jack (can provide plug-in power)**

Connector: 1/8" (3.5 mm) stereo mini jack
Input impedance: 25 kΩ
Reference input level: –20dBV
Maximum input level: –4dBV

■ **Ω/LINE OUT jack**

Connector: 1/8" (3.5 mm) stereo mini jack
Output impedance: 12 Ω
Reference output level: –14dBV (with 10kΩ load)
Maximum output level: +2dBV (with 10kΩ load)
Maximum output: 20mW+20mW (with 32Ω load)

■ **Built-in speaker**

0.3W (mono)

Control input/output ratings

■ **USB port**

Connector: Micro-B type
Format: USB 2.0 HIGH SPEED mass storage class

Audio performance

■ **Frequency response**

20-20 kHz +1/-3 dB (EXT IN to LINE OUT, Fs44.1 kHz, JEITA)
20-22kHz +1/-3 dB (EXT IN to LINE OUT, Fs48kHz, JEITA)
20-40kHz +1/-3 dB (EXT IN to LINE OUT, Fs96kHz, JEITA)

■ **Distortion**

0.05% or less (EXT IN to LINE OUT, Fs44.1k/48k/96kHz, JEITA)

■ **S/N ratio**

92dB or above (EXT IN to LINE OUT, Fs44.1k/48k/96kHz, JEITA)

Note) Based on JEITA: JEITA CP-2150

Requirements for connected computers

Please visit the TEAC Global Site (**http://teac-global.com**) to learn the latest compatible OS.

■ **Windows**

Pentium 300MHz or more
128MB or more memory
USB port (USB2.0 is recommended)

■ **Mac**

Power PC, iMac, G3, or G4 with 266MHz or above
64MB or more memory
USB port (USB2.0 is recommended)

■ **Recommended USB host controller**

Intel chip set

■ **Supported operating systems**

Windows: Windows XP, Windows Vista, Windows 7, Windows 8 (including 8.1)
Macintosh: Mac OS X 10.2 or later

Wi-Fi

■ **Wireless standard**

Based on IEEE 802.11b/g/n (2.4GHz only)

■ **Wireless communication mode**

Simple access point (Limited AP)

■ **Security**

WPA2-PSK (WPS2.0 compatible)

Figure B-3: DR22WL Recorder - Technical Data 1

13 – Specifications

General

■ **Power supply**

2 AA batteries (alkaline or NiMH)
USB bus power from a computer
Dedicated AC adapter (TASCAM PS-P515U; sold separately)

■ **Current consumption**

0.5 A (maximum)

■ **Battery operation time (continuous operation)**

* Alkaline batteries (EVOLTA)

Format	Operation time	Note
Recorded in WAV, 96kHz, 24bit	About 9 hours	Input from the built-in microphone
Recorded in WAV, 44.1kHz, 16bit	About 17.5 hours	Input from the built-in microphone
Recorded in MP3 format, 44.1kHz, 128kbps	About 12 hours	Input from the built-in microphone
Recorded in MP3 format, 48kHz, 320kbps	About 11 hours	Input from the built-in microphone
Playback in WAV, 96kHz, 24bit	About 11 hours	When using a headphone
Playback in WAV, 44.1kHz, 16bit	About 13 hours	When using a headphone
Playback in MP3 format, 44.1kHz, 128kbps	About 11 hours	When using a headphone
Playback in MP3 format, 48kHz, 320kbps	About 11 hours	When using a headphone

Recording: JEITA recording time Playback: JEITA music playback time

* Using NiMH batteries (eneloop)

Format	Operation time	Note
Recorded in WAV, 96kHz, 24bit	About 9 hours	Input from the built-in microphone
Recorded in WAV, 44.1kHz, 16bit	About 13.5 hours	Input from the built-in microphone
Recorded in MP3 format, 44.1kHz, 128kbps	About 12 hours	Input from the built-in microphone
Recorded in MP3 format, 48kHz, 320kbps	About 11 hours	Input from the built-in microphone
Playback in WAV, 96kHz, 24bit	About 12 hours	When using a headphone
Playback in WAV, 44.1kHz, 16bit	About 13.5 hours	When using a headphone
Playback in MP3 format, 44.1kHz, 128kbps	About 10 hours	When using a headphone
Playback in MP3 format, 48kHz, 320kbps	About 10 hours	When using a headphone

Recording: JEITA recording time Playback: JEITA music playback time

■ **Dimensions**

52.2 × 155 × 36.6mm (W x H x D)

■ **Weight**

170 g/123 g (with batteries/without batteries)

■ **Operating temperature**

0°C–40°C

Dimensional drawings

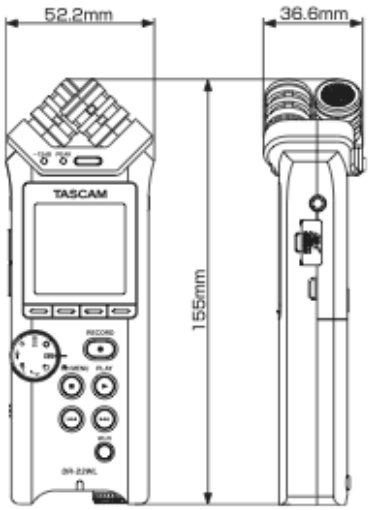

* Illustrations in this manual may be different from the actual product.
* To improve the product, specifications and external appearance may change without prior notice.

Figure B-4: DR22WL Recorder - Technical Data 1

Cetacean Research Technology
7511 Greenwood Ave N #615
Seattle, WA 98103
206-650-8676
www.CetResTec.com

C57 Hydrophone Serial Number 875

C57 Hydrophone Sensitivity = -170.50 dB, re. 1V/µPa

Gain Setting	DR-22WL System Sensitivity [dBFS, re. 1Vpp/µPa]
0	-176.32
1	-175.83
5	-173.84
10	-171.34
20	-166.33
30	-161.26
40	-155.73
50	-150.72
60	-145.66
70	-140.68
80	-135.69
90	-130.67

e.g., when using a gain setting of 20, a peak-peak received level of 166.33 dB, re 1µPa would result in a 100% full scale reading on the file recorded by the DR-22WL.

Figure B-5: C57 Hydrophone Calibration Data with Recorder

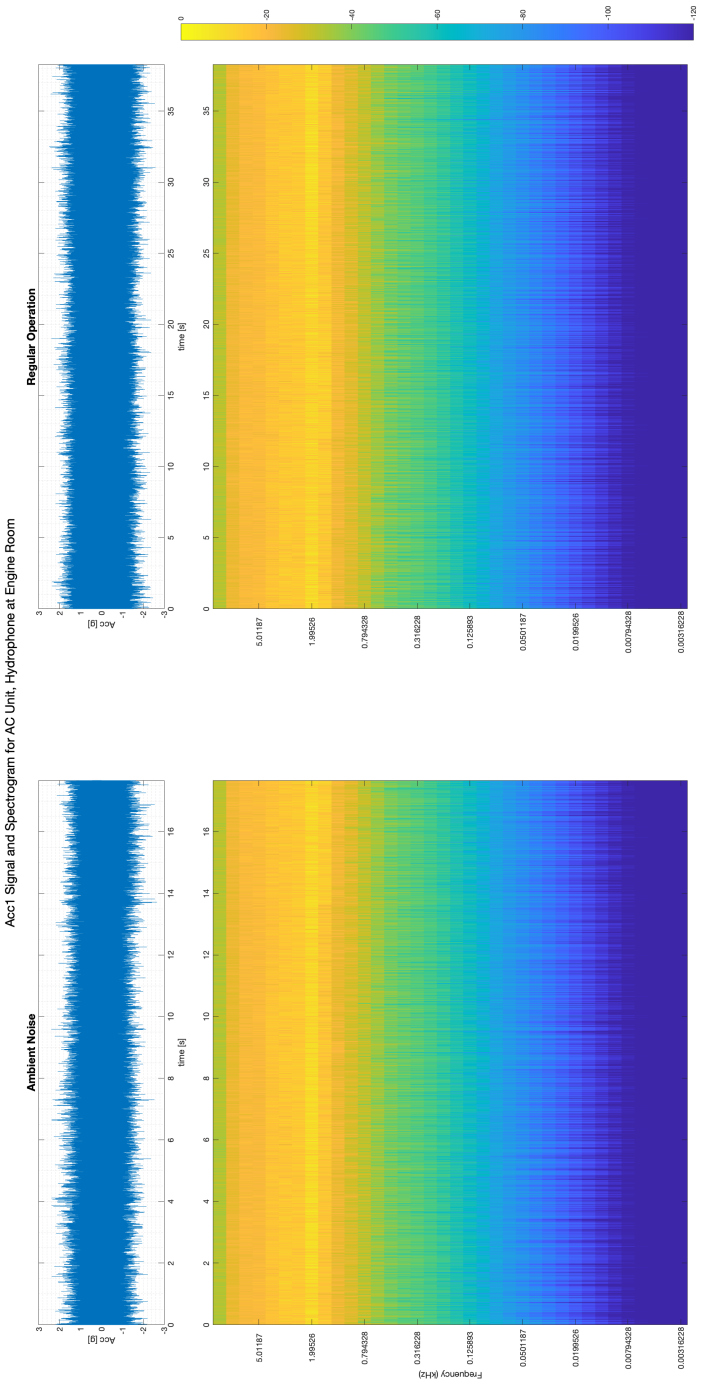

Figure B-6: Accelerometer 1 Data, AC Unit, Hydrophone at "A"

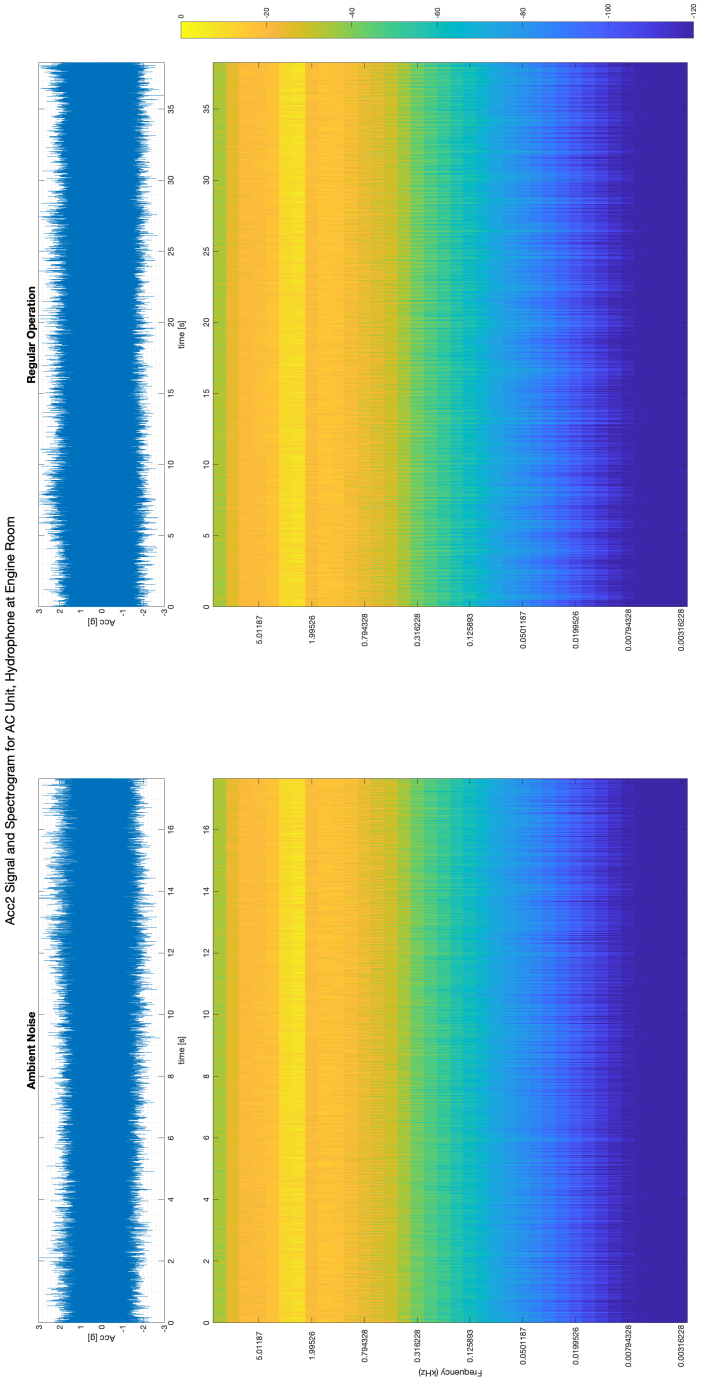

Figure B-7: Accelerometer 2 Data, AC Unit, Hydrophone at "A"

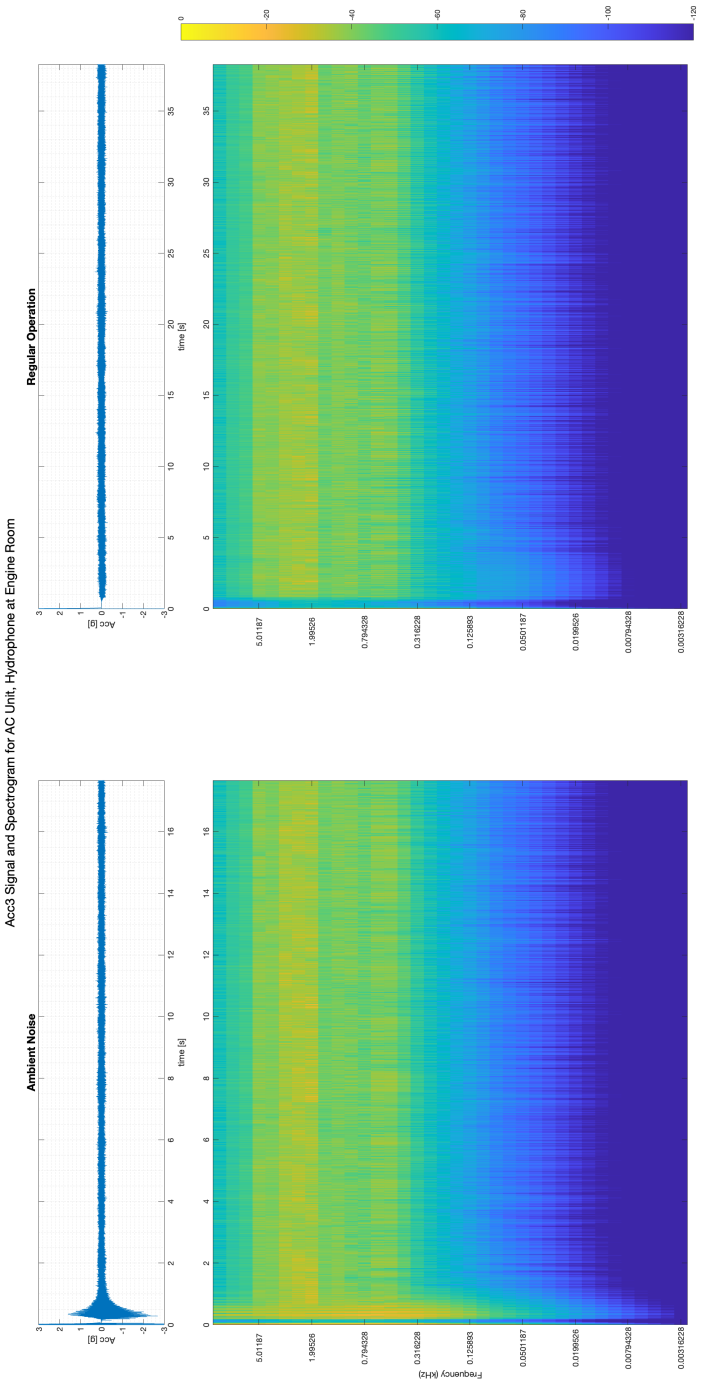

Figure B-8: Accelerometer 3 Data, AC Unit, Hydrophone at "A"

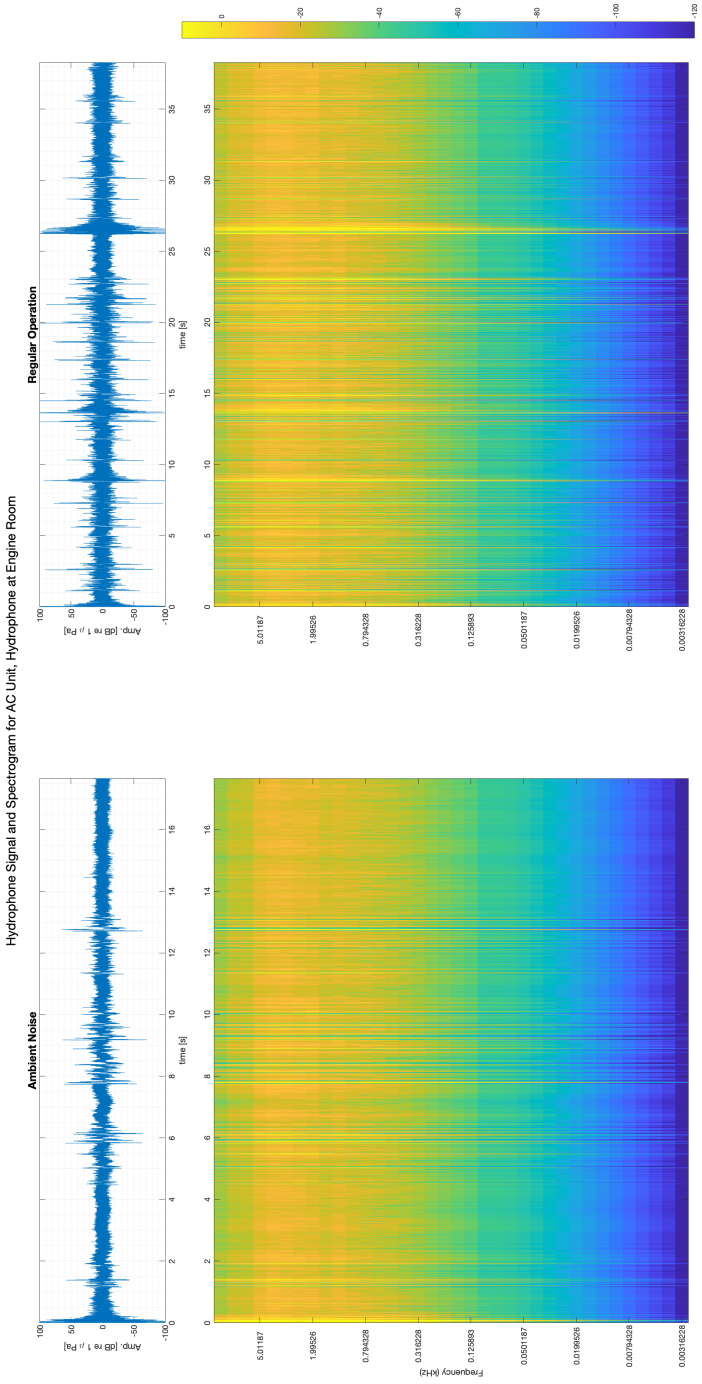

Figure B-9: Hydrophone Data, AC Unit, Hydrophone at "A"

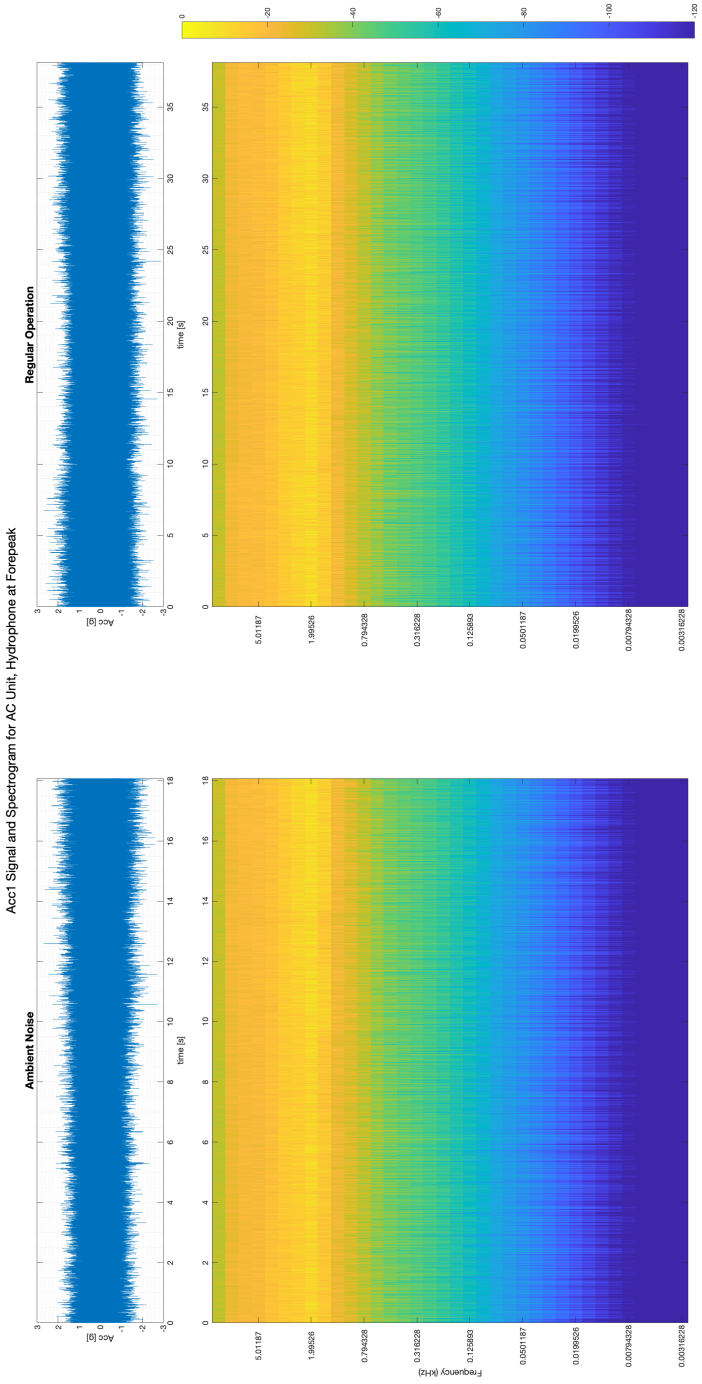

Figure B-10: Accelerometer 1 Data, AC Unit, Hydrophone at "B"

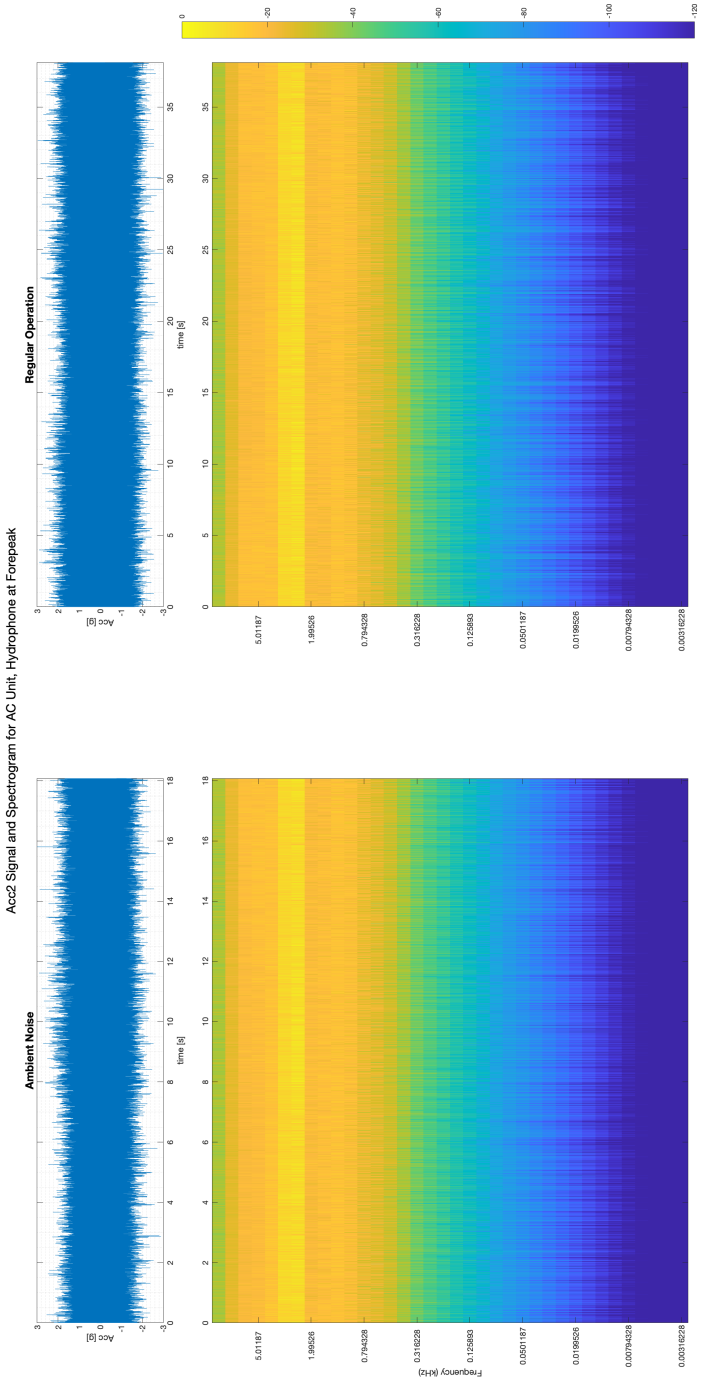

Figure B-11: Accelerometer 2 Data, AC Unit, Hydrophone at "B"

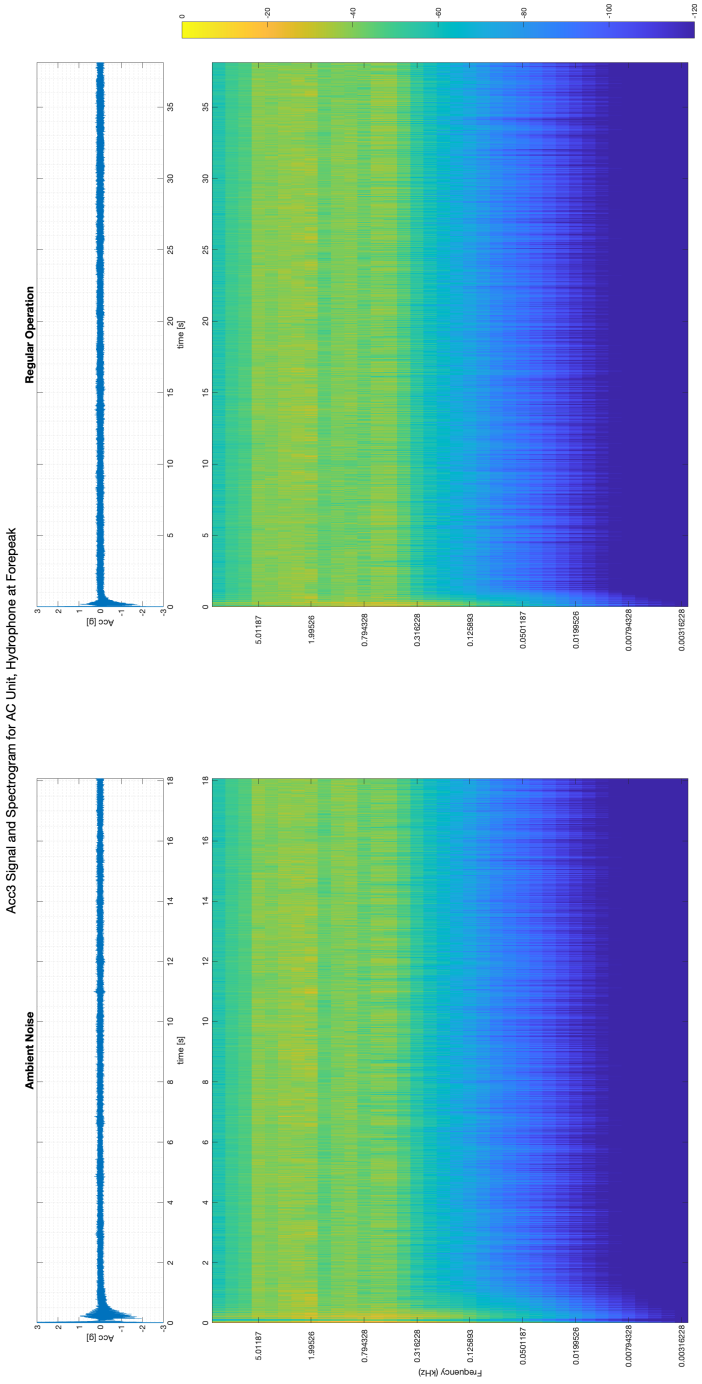

Figure B-12: Accelerometer 3 Data, AC Unit, Hydrophone at "B"

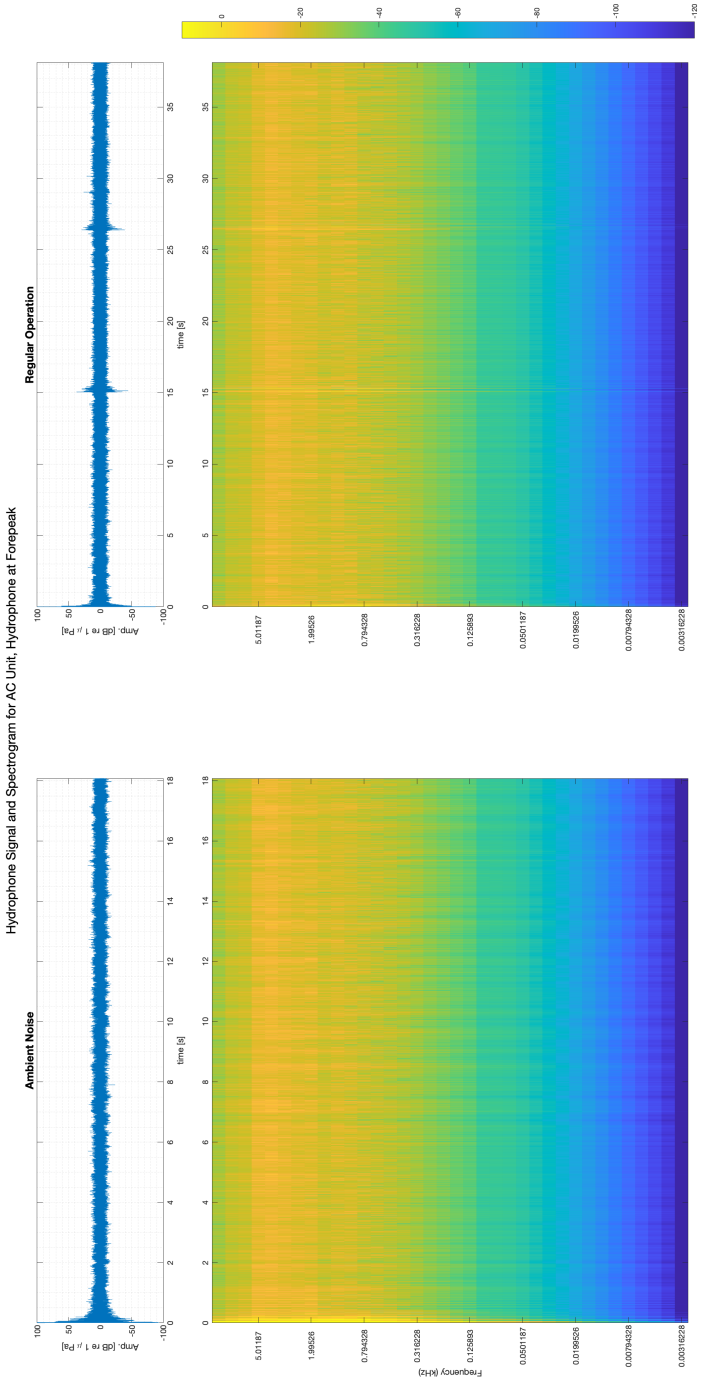

Figure B-13: Hydrophone Data, AC Unit, Hydrophone at "B"

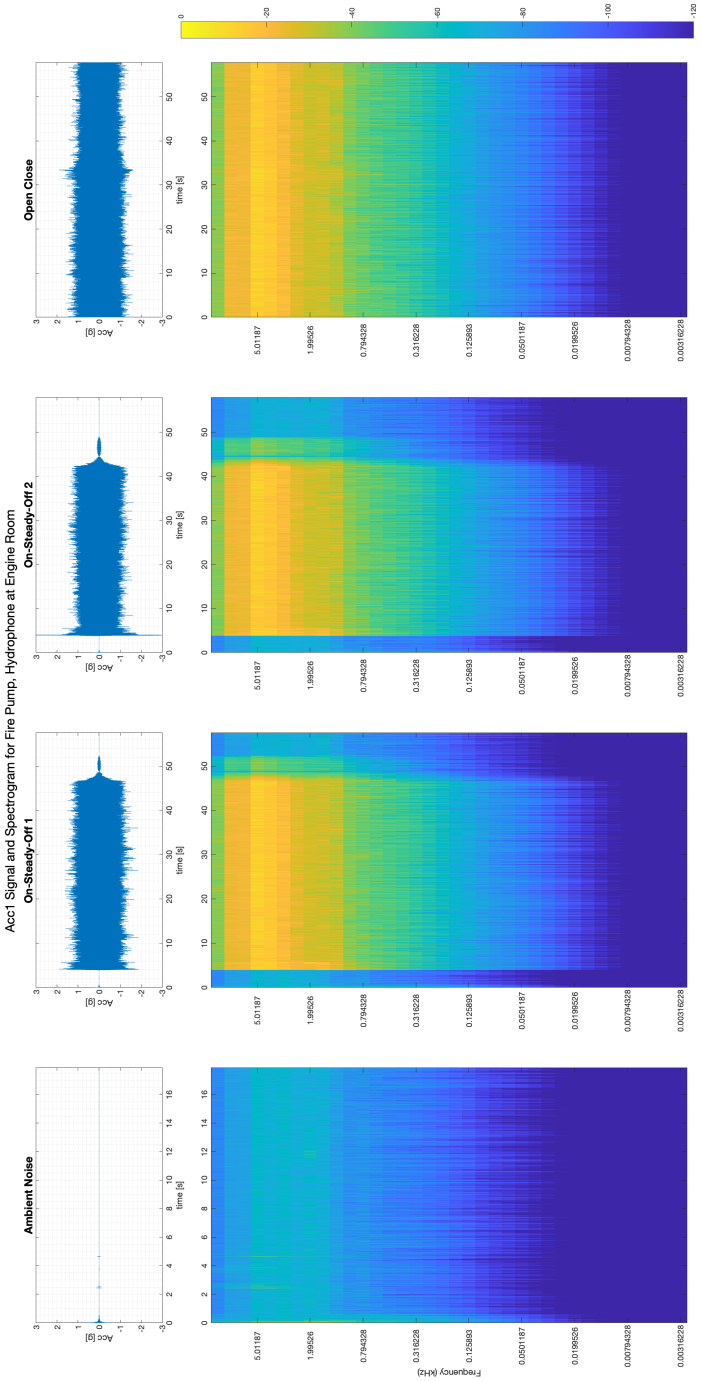

Figure B-14: Accelerometer 1 Data, Fire Pump, Hydrophone at "A"

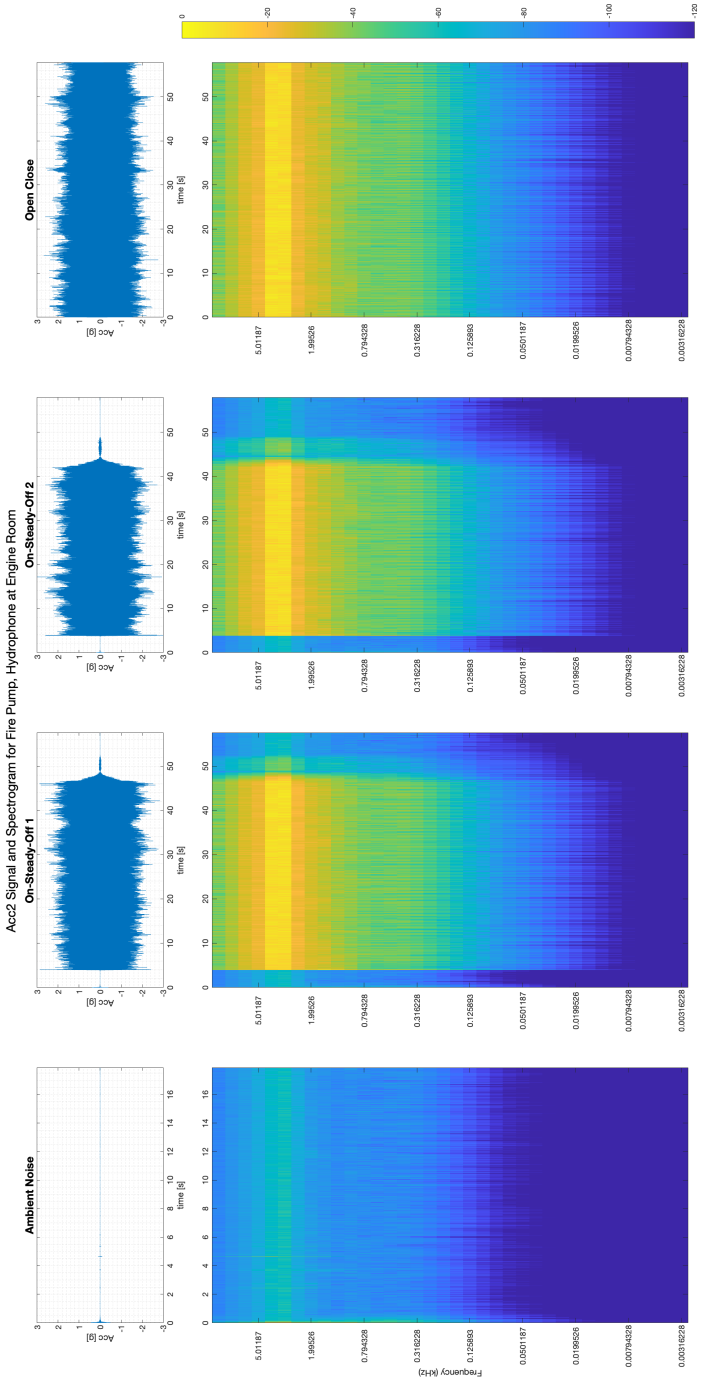

Figure B-15: Accelerometer 2 Data, Fire Pump, Hydrophone at "A"

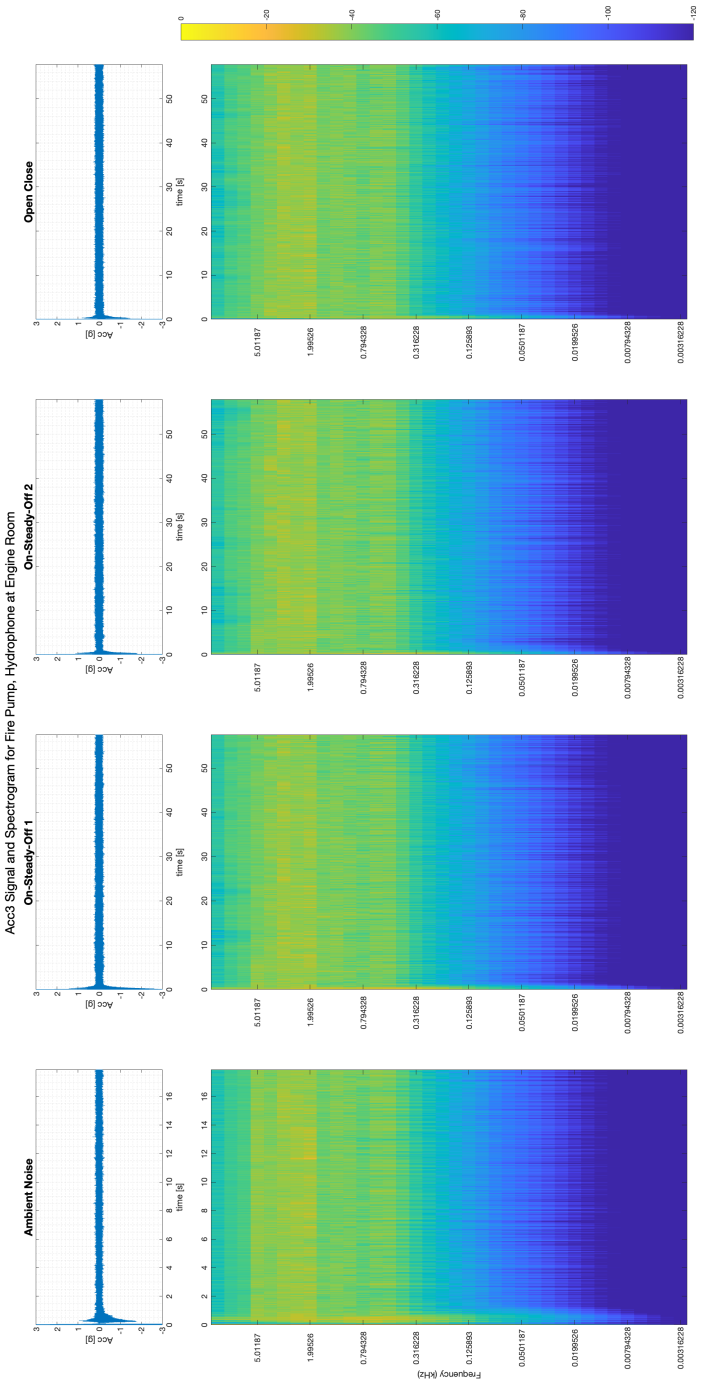

Figure B-16: Accelerometer 3 Data, Fire Pump, Hydrophone at "A"

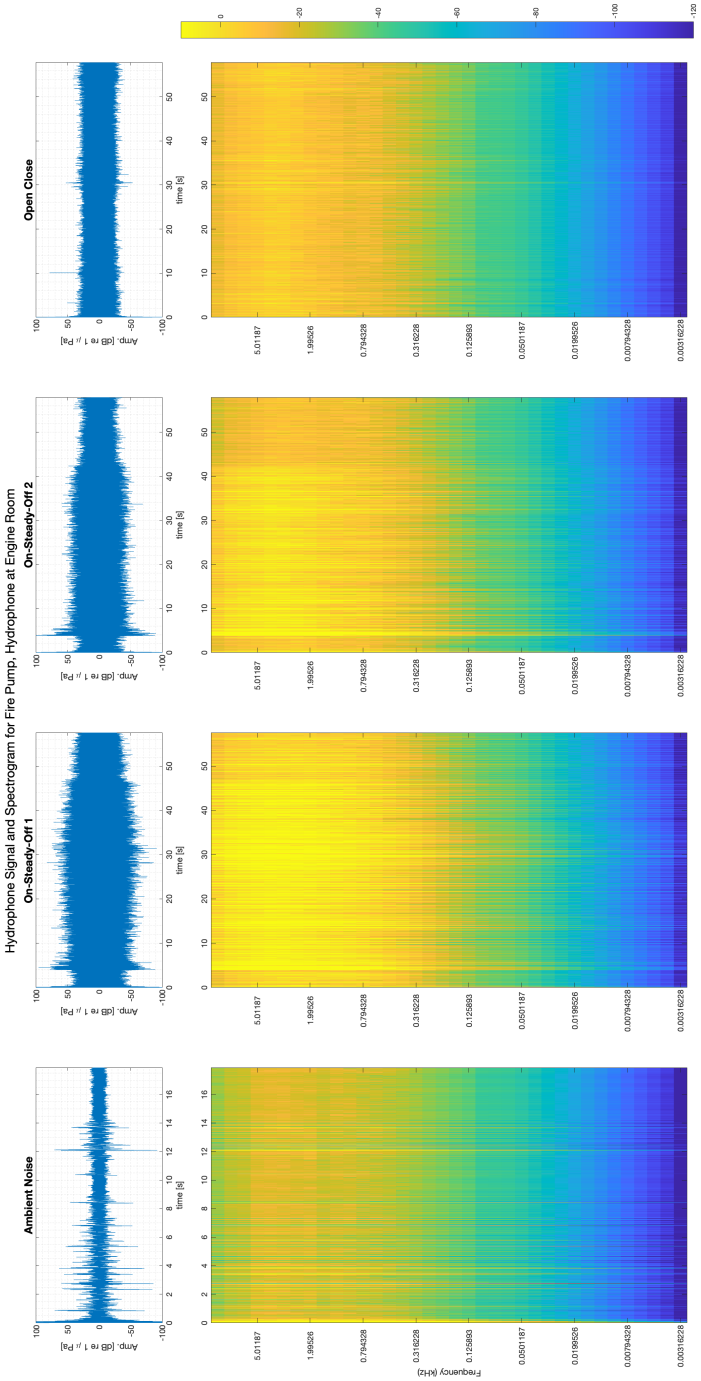

Figure B-17: Hydrophone Data, Fire Pump, Hydrophone at "A"

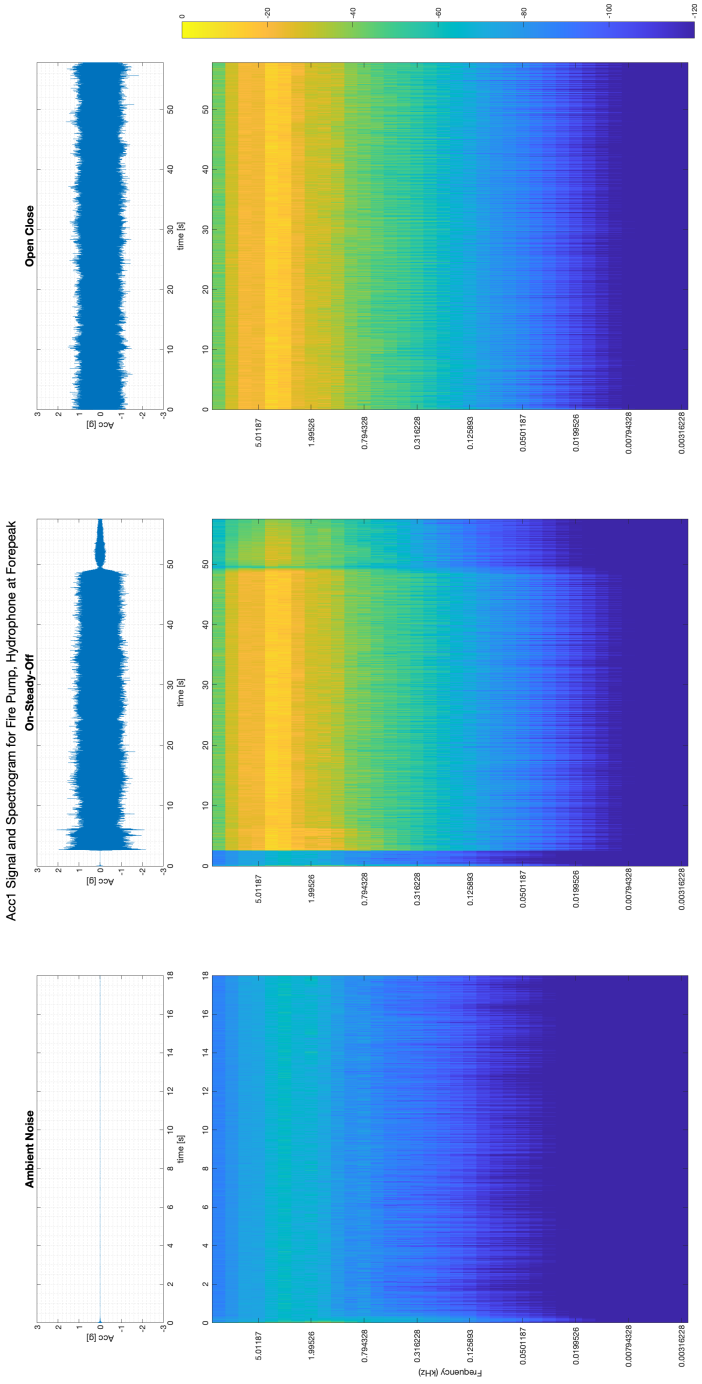

Figure B-18: Accelerometer 1 Data, Fire Pump, Hydrophone at "B"

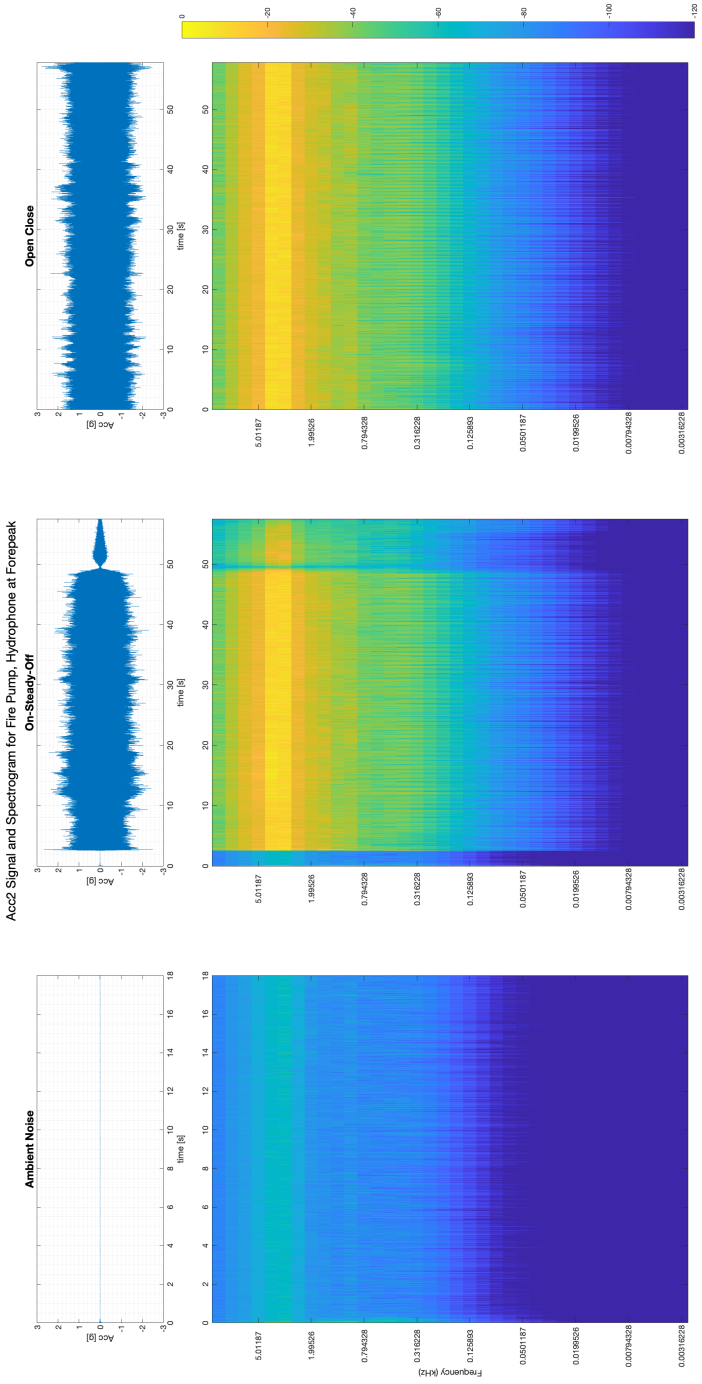

Figure B-19: Accelerometer 2 Data, Fire Pump, Hydrophone at "B"

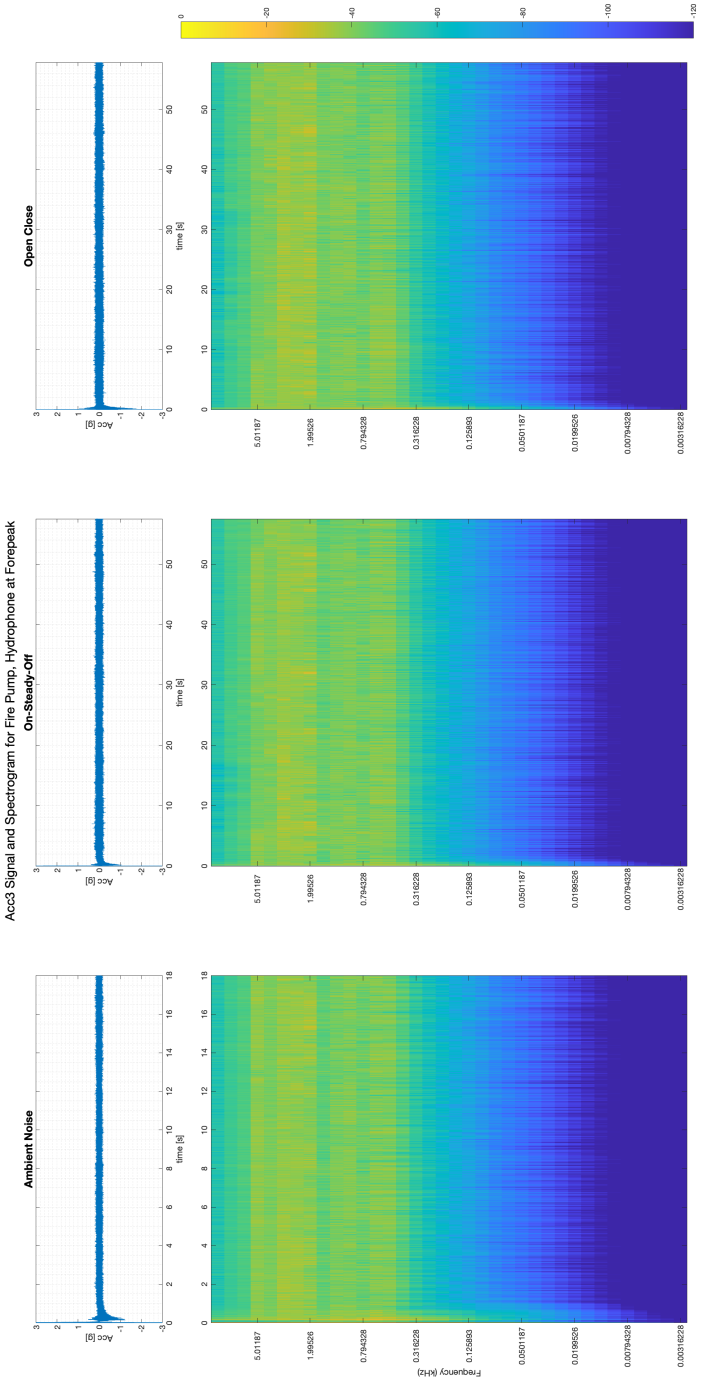

Figure B-20: Accelerometer 3 Data, Fire Pump, Hydrophone at "B"

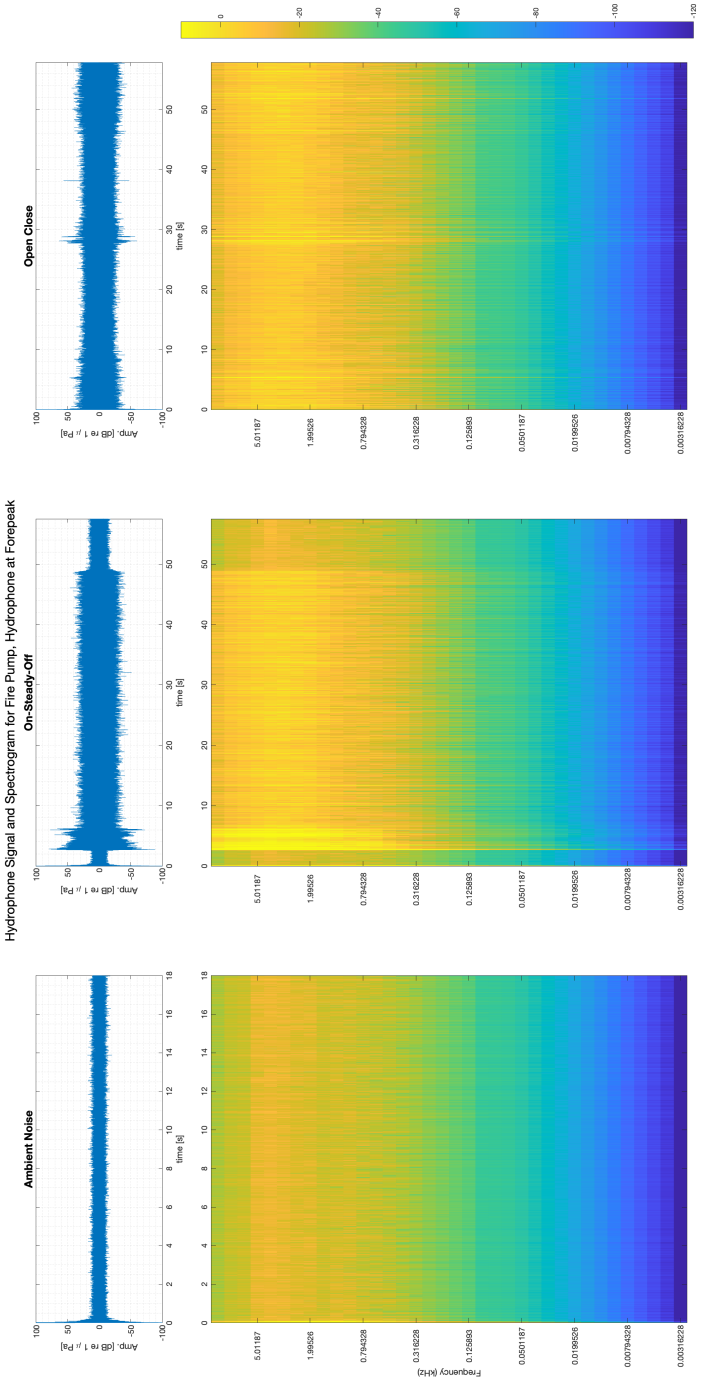

Figure B-21: Hydrophone Data, Fire Pump, Hydrophone at "B"

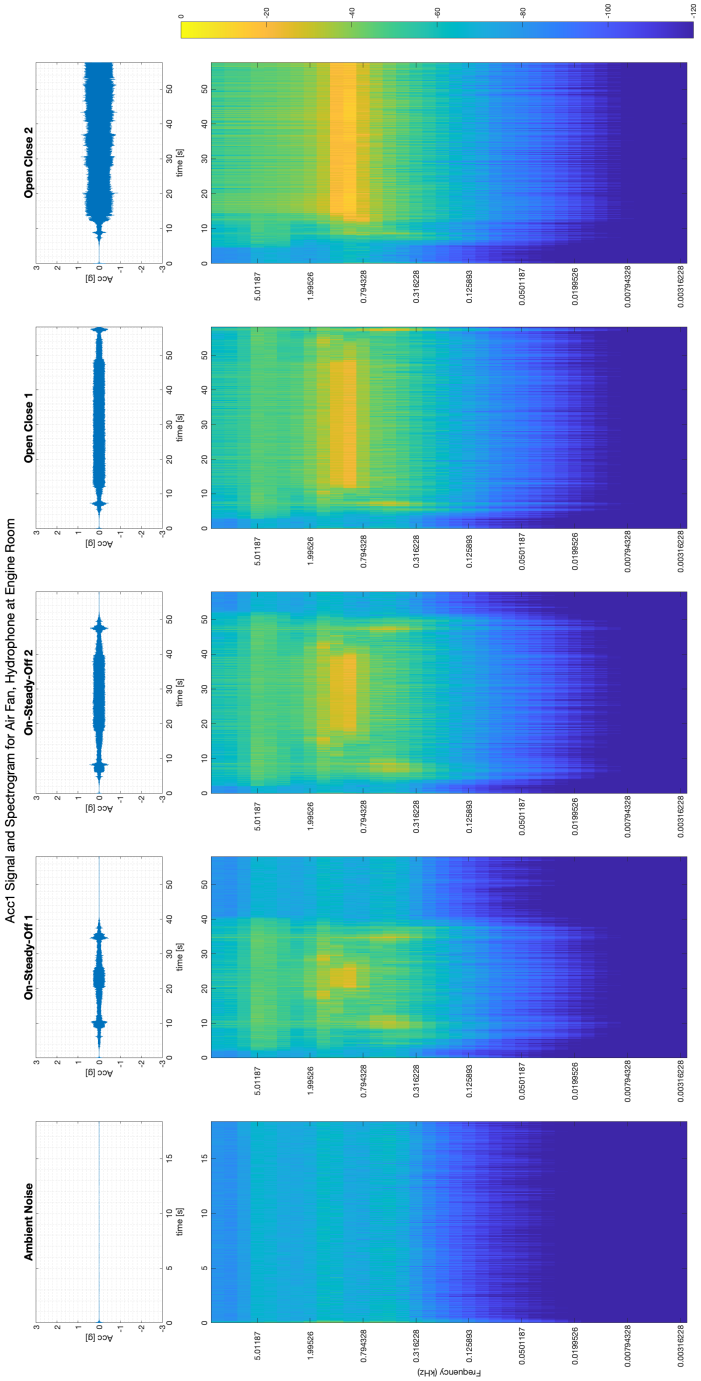

Figure B-22: Accelerometer 1 Data, Air Fan, Hydrophone at "A"

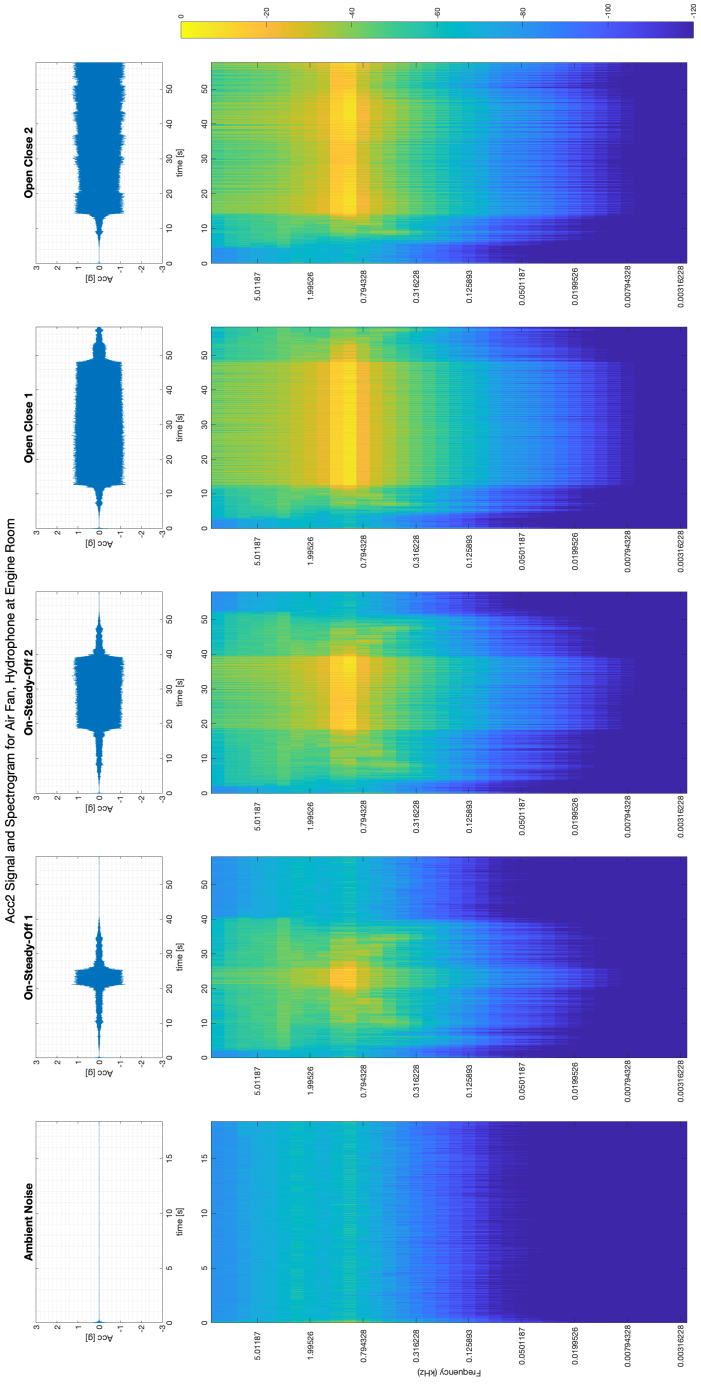

Figure B-23: Accelerometer 2 Data, Air Fan, Hydrophone at "A"

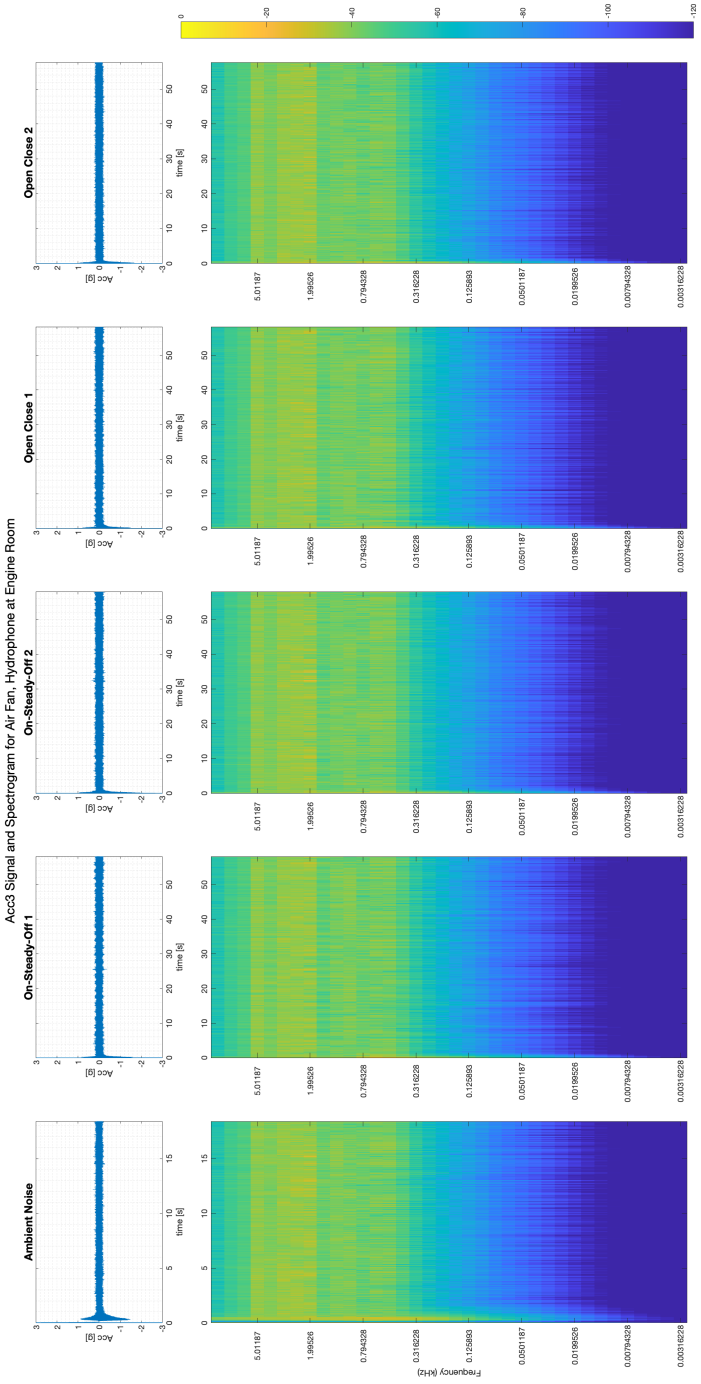

Figure B-24: Accelerometer 3 Data, Air Fan, Hydrophone at "A"

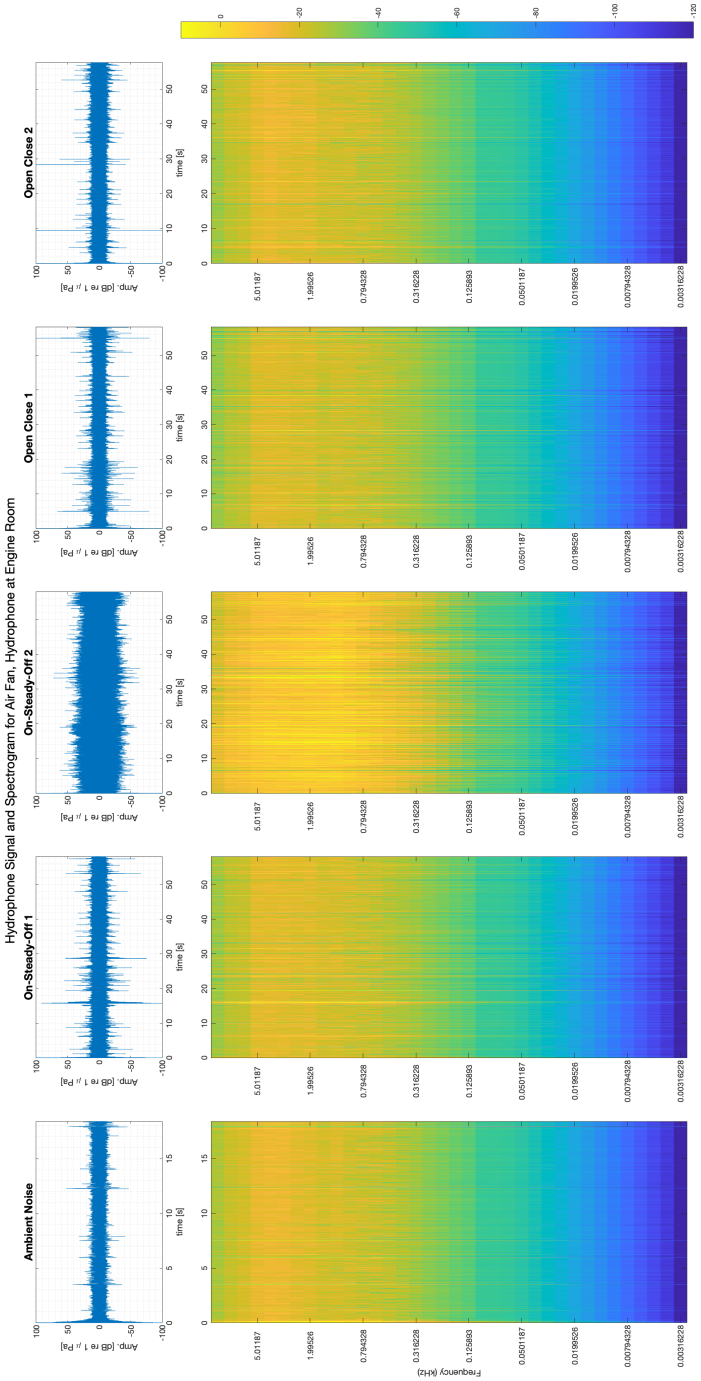

Figure B-25: Hydrophone Data, Air Fan, Hydrophone at "A"

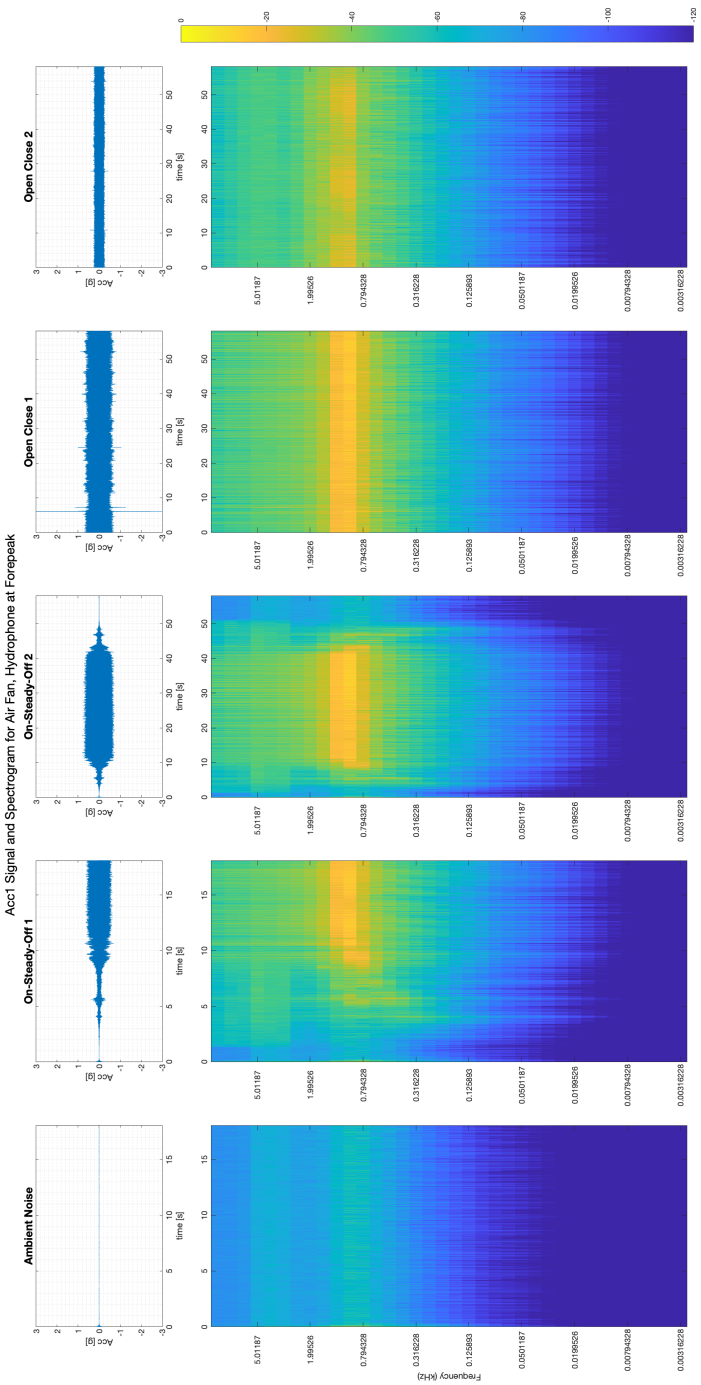

Figure B-26: Accelerometer 1 Data, Air Fan, Hydrophone at "B"

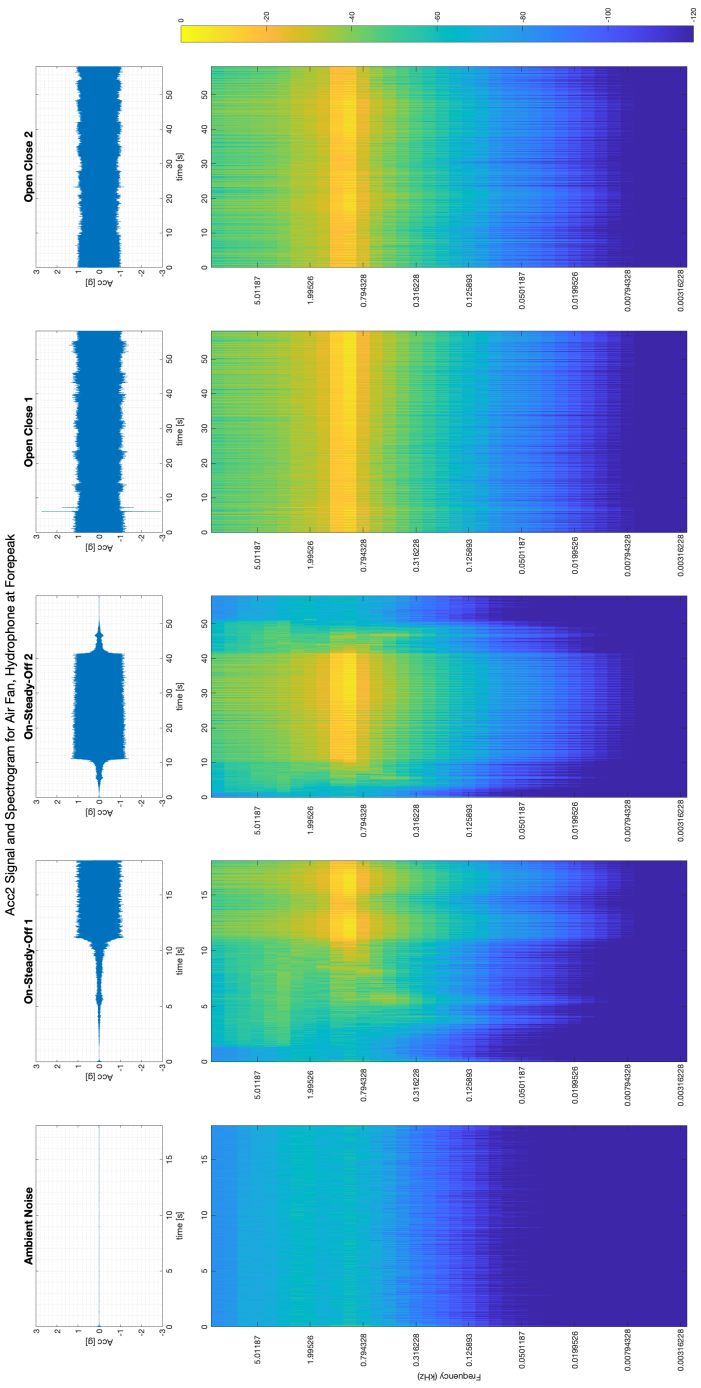

Figure B-27: Accelerometer 2 Data, Air Fan, Hydrophone at "B"

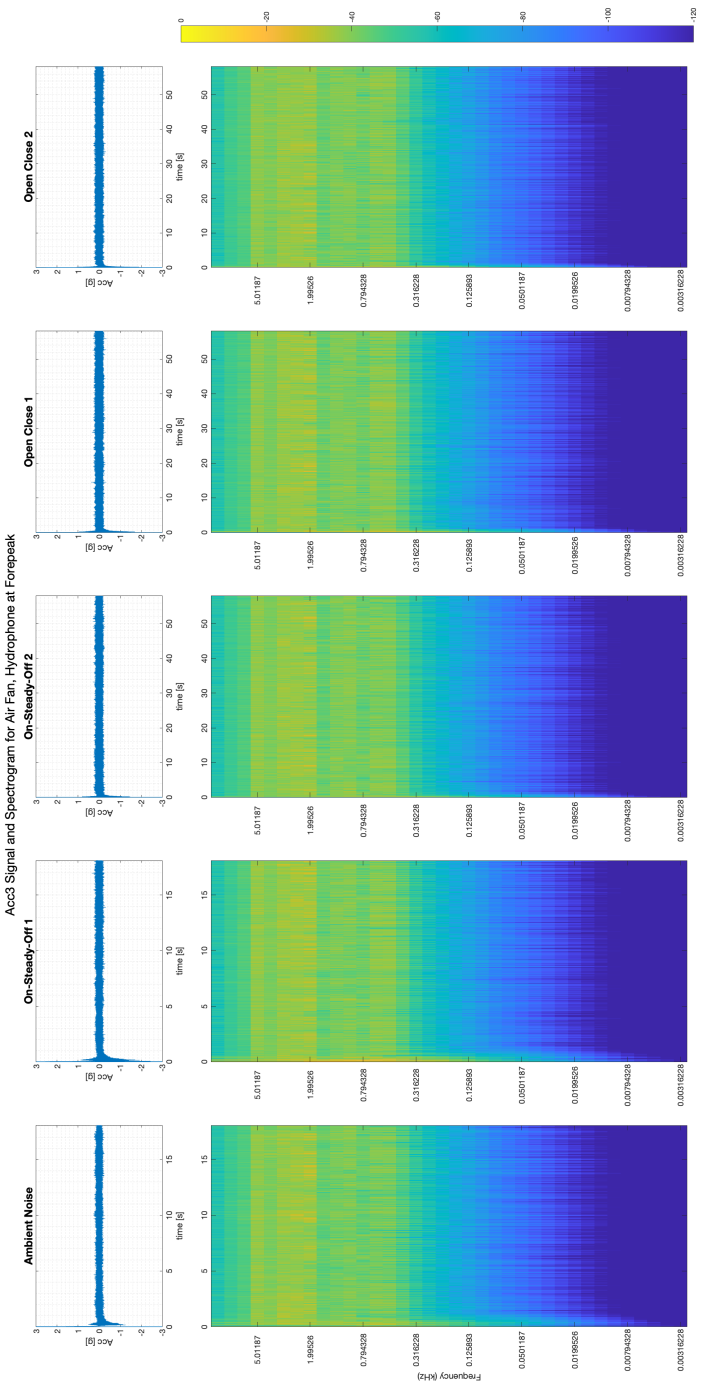

Figure B-28: Accelerometer 3 Data, Air Fan, Hydrophone at "B"

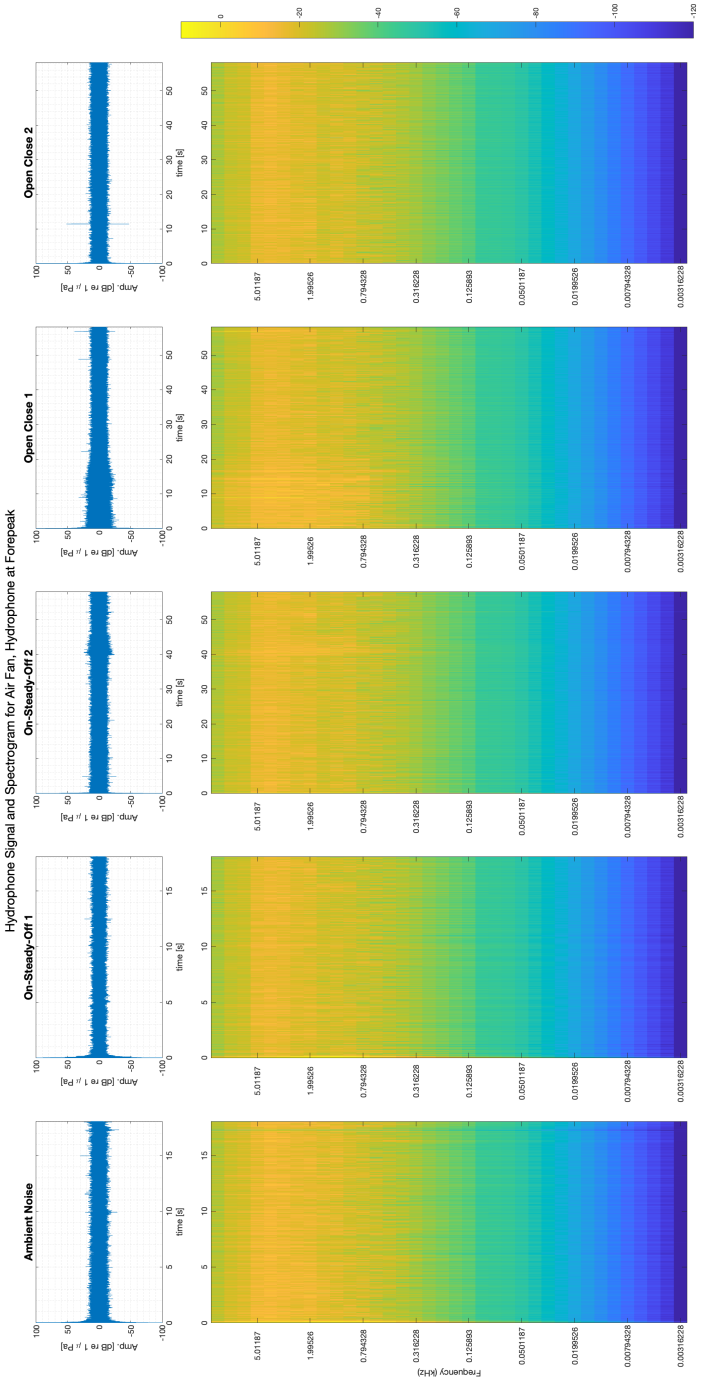

Figure B-29: Hydrophone Data, Air Fan, Hydrophone at "B"

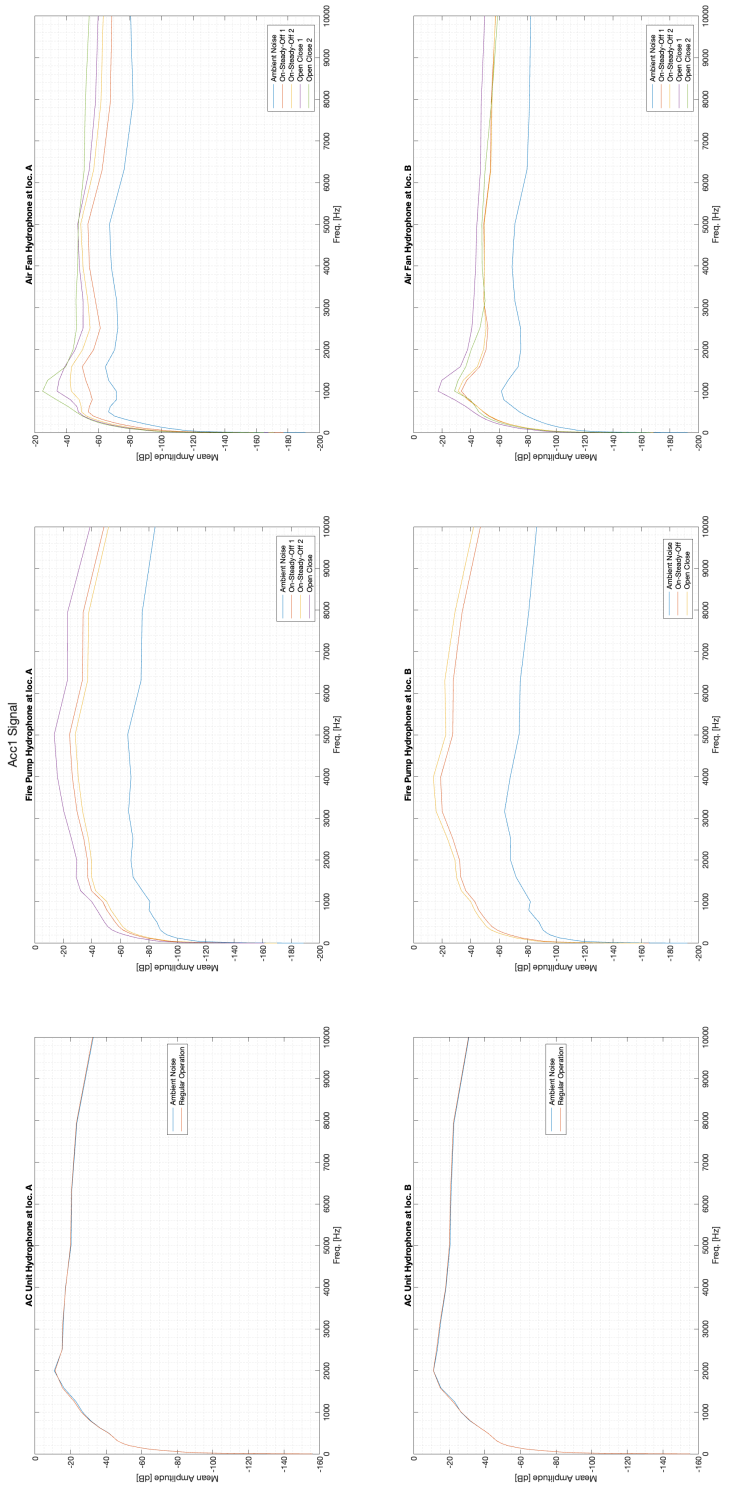

Figure B-30: Time Averaged Magnitude Levels, Accelerometer 1

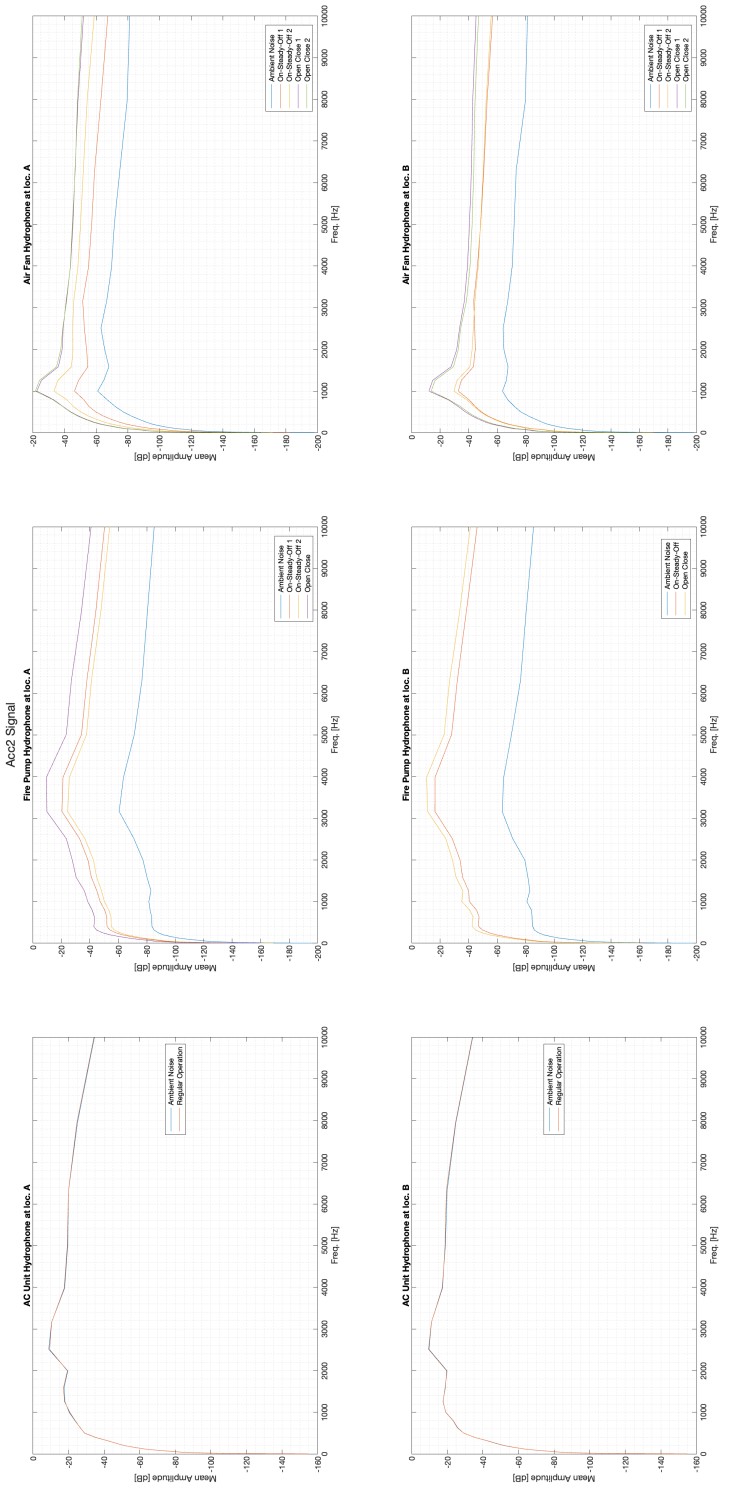

Figure B-31: Time Averaged Magnitude Levels, Accelerometer 2

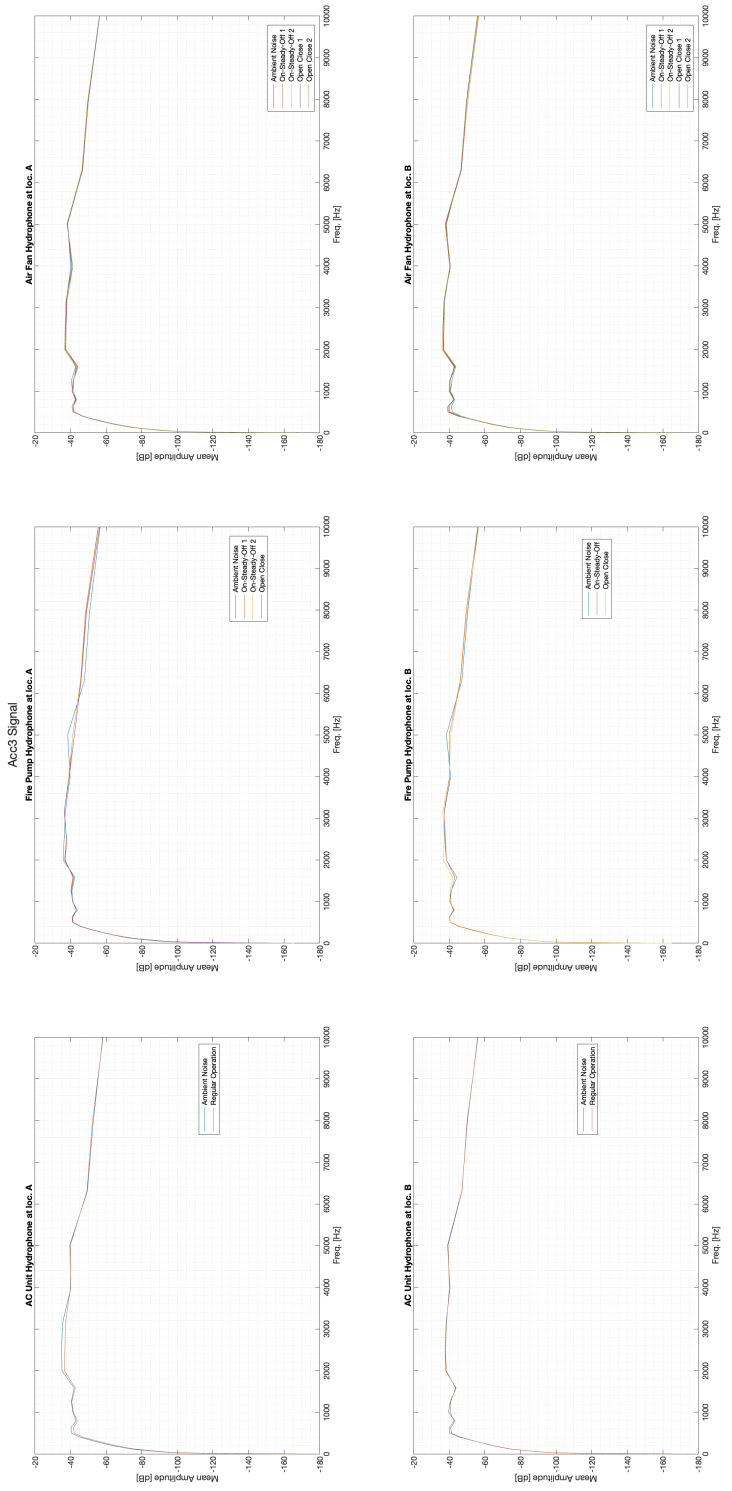

Figure B-32: Time Averaged Magnitude Levels, Accelerometer 3

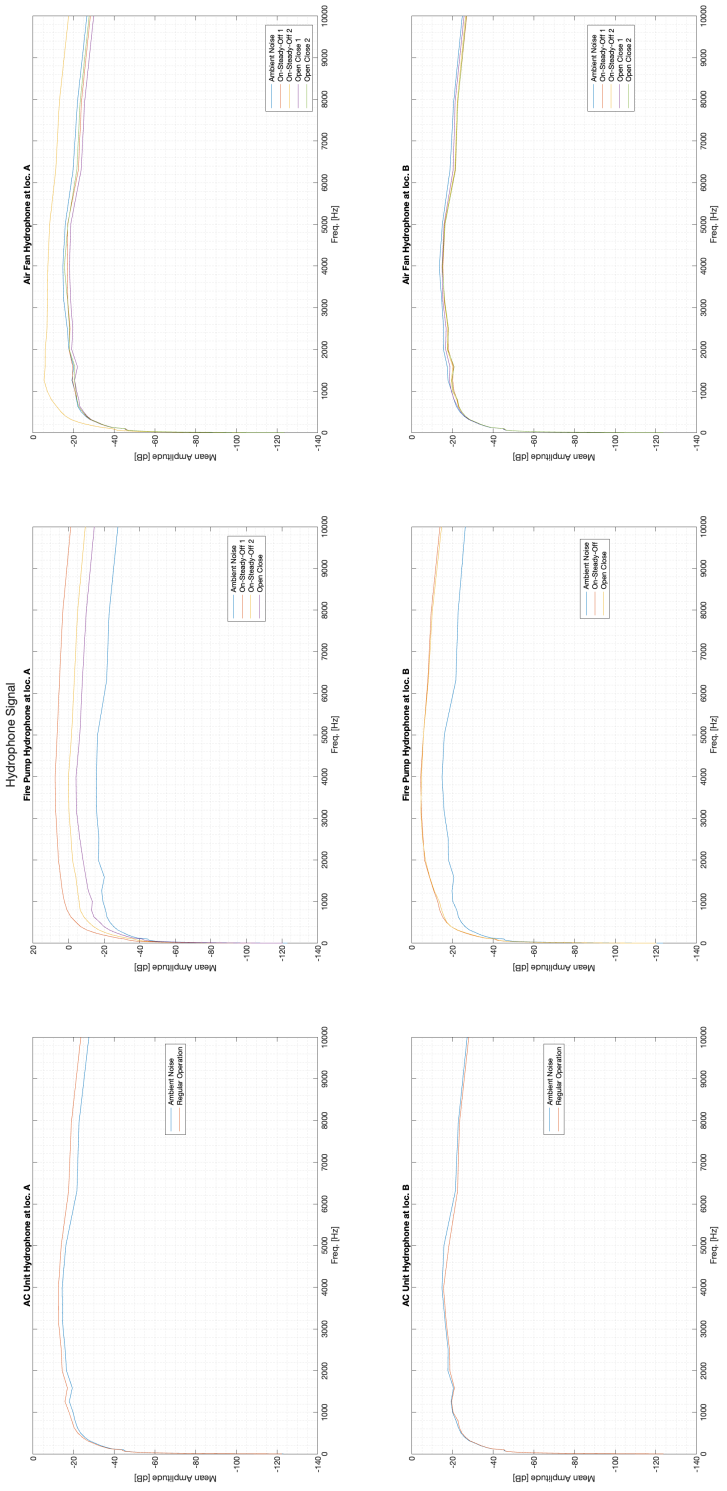

Figure B-33: Time Averaged Magnitude Levels, Hydrophone

Bibliography

[1] Andre Aboulian, Daisy H. Green, Jennifer F. Switzer, Thomas J. Kane, Gregory V. Bredariol, Peter Lindahl, John S. Donnal, and Steven B. Leeb. Nilm dashboard: A power system monitor for electromechanical equipment diagnostics. *IEEE Transactions on Industrial Informatics*, 15(3):1405–1414, 2019.

[2] Léa Bouffaut. *Détection et classification dans un contexte acoustique passive : application à la détection des signaux basse-fréquences des baleines bleues*. PhD thesis, Université de Bretagne occidentale, 10 2019.

[3] Roy Burcher and Louis J. Rydill. *Concepts in Submarine Design*. Cambridge Ocean Technology Series. Cambridge University Press, 1994.

[4] Paul G. Dylejko, Ian R. MacGillivray, Stephen M. Moore, and Alex T. Skvortsov. The influence of internal resonances from machinery mounts on radiated noise from ships. *IEEE Journal of Oceanic Engineering*, 42(2):399–409, 2017.

[5] Alex Graves, Abdel-rahman Mohamed, and Geoffrey Hinton. Speech recognition with deep recurrent neural networks. In *2013 IEEE International Conference on Acoustics, Speech and Signal Processing*, pages 6645–6649, 2013.

[6] Jens Hovem. *Ray Trace Modeling of Underwater Sound Propagation*, page 26. InTech - Open Access Publisher, Rijeka, Croatia, 08 2013.

[7] Lukasz Huchel, Jan Helsen, Peter Lindahl, and Steven Leeb. Diagnostics for periodically excited actuators. *IEEE Transactions on Instrumentation and Measurement*, PP:1–1, 10 2019.

[8] Daniel Johansson and Peter Comnell. Statistial energy analysis software. development and implementation of an open source code in matlab/octave. In *Chalmers UoT*, 2010.

[9] Christian Kanzow, Nobuo Yamashita, and Masao Fukushima. Levenberg–marquardt methods with strong local convergence properties for solving nonlinear equations with convex constraints. *Journal of Computational and Applied Mathematics*, 172(2):375–397, 2004.

[10] R.H. Lyon and R.G. DeJong. *Theory and Application of Statistical Energy Analysis*. Butterworth-Heinemann, 1995.

[11] Gideon Maidanik. Response of ribbed panels to reverberant acoustic fields. *The Journal of the Acoustical Society of America*, 34:809–826, 1962.

[12] Hermann Mayer, Faustino Gomez, Daan Wierstra, Istvan Nagy, Alois Knoll, and Jurgen Schmidhuber. A system for robotic heart surgery that learns to tie knots using recurrent neural networks. In *2006 IEEE/RSJ International Conference on Intelligent Robots and Systems*, pages 543–548, 2006.

[13] V Meyer, L Maxit, J.-L. Guyader, and T Leissing. Prediction of the vibroacoustic behavior of a submerged shell with non-axisymmetric internal substructures by a condensed transfer function method. *Journal of Sound and Vibration*, 360:260–276, 2016.

[14] Gábor Petneházi. Recurrent neural networks for time series forecasting. *CoRR*, abs/1901.00069, 2019.

[15] C. Schantz, K. Gerhard, J. Donnal, J. Moon, B. Sievenpiper, S. Leeb, and K. Thomas. Retrofittable machine condition and structural excitation monitoring from the terminal box. *IEEE Sensors Journal*, 16(5):1224–1232, March 2016.

[16] M Schroeder, Thomas D Rossing, F Dunn, W M Hartmann, D M Campbell, and N H Fletcher. *Springer Handbook of Acoustics*. Springer Publishing Company, Incorporated, 1st edition, 2007.

[17] Tomoki Takami, Sadaoki Matsui, Masayoshi Oka, and Kazuhiro Iijima. A numerical simulation method for predicting global and local hydroelastic response of a ship based on cfd and fea coupling. *Marine Structures*, 59:368–386, 2018.

[18] Jan Verheij. *Multi-path sound transfer from resiliently mounted shipboard machinery - Experimental methods for analyzing and improving noise control*. PhD thesis, Institute of Applied Physics TNO-TH, 05 1982.

[19] Haesang Yang and Woojae Seong. Acoustic radiation efficiency of a submerged periodic ring-stiffened cylindrical shell with finite vibration loading. *Applied Acoustics*, 171:107664, 2021.